Journal of Biomedical Science and Engineering

Editor-in-Chief
Kuo-Chen Chou

Journal Editorial Board

TABLE OF CONTENTS

Volume 2, Number 3, June 2009

The figure on the front cover shows the binding interaction of the human TXA2 receptor with G alpha 13. (Courtesy of Kuo-Chen Chou.)

Journal of Biomedical Science and Engineering (JBiSE)

News and Announcement

We are pleased to announce that two of the Editorial Board Members of **JBiSE**, Kuo-Chen Chou and Hong-Bin Shen, have been identified by Science Watch (http://sciencewatch.com/ana/fea/09maraprFea/) as the authors with the highest numbers of Hot Papers published over the preceding two years (2007 and 2008). Among the 13 authors listed in the table of **"**Scientists with Multiple Hot Papers" by Science Watch, Professor Dr. Kuo-Chen Chou of Gordon Life Science institute and Shanghai Jiaotong University ranks No.1 with 17 hot papers, and Associated Professor Hong-Bin Shen of Shanghai Jiaotong University ranks No.4 with 13 hot papers.

Meanwhile, the review article by Kuo-Chen Chou and Hong-Bin Shen, entitled "Recent Progresses in Protein Sub-cellular Location Prediction" published in Analytical Biochemistry, has been identified by Science Watch as the New Hot Paper in the field of Biology & Biochemistry (http://sciencewatch.com/dr/nhp/2009/09marnhp/09marnhpChou/).

For more information about the hot research and hot papers, go to visit the web-sites at http://www.sciencenet.cn/htmlnews/2009/3/216833.html; http://sciencewatch.com/ana/fea/pdf/09maraprFea.pdf; and http://sciencewatch.com/dr/nhp/2009/pdf/09marnhpChou.pdf.

Please join us to send our sincere and warm congratulations to our fellow board members, Kuo-Chen Chou and Hong-Bin Shen, for their prominent contributions in science. Meanwhile, we hope this announcement can attract more researchers to submit their best papers to **JBiSE**, the journal that publishes the highest quality of research and review articles in all important aspects of biology, medicine, engineering, and their intersection.

We would also like to take this opportunity to announce that, owing to the large number of manuscripts that we are receiving, **JBiSE** will increase publication frequency from quarterly to bi-monthly in 2009.

<div align="right">**JBiSE** Editorial Office</div>

Prediction of protein folding rates from primary sequence by fusing multiple sequential features

Hong-Bin Shen[1,3,*], Jiang-Ning Song[2], Kuo-Chen Chou[1,3]

[1]Institute of Image Processing & Pattern Recognition, Shanghai Jiaotong University, 800 Dongchuan Road, Shanghai, 200240, China; [2]Bioinformatics Center, Institute for Chemical Research, Kyoto University, Gokasho, Uji, Kyoto 611-0011, Japan; [3]Gordon Life Science Institute, 13784 Torrey Del Mar Drive, San Diego, California 92130, USA.
*Corresponding author: hbshen@sjtu.edu.cn

ABSTRACT

We have developed a web-server for predicting the folding rate of a protein based on its amino acid sequence information alone. The web-server is called Pred-PFR (Predicting Protein Folding Rate). Pred-PFR is featured by fusing multiple individual predictors, each of which is established based on one special feature derived from the protein sequence. The ensemble predictor thus formed is superior to the individual ones, as demonstrated by achieving higher correlation coefficient and lower root mean square deviation between the predicted and observed results when examined by the jackknife cross-validation on a benchmark dataset constructed recently. As a user-friendly web-server, Pred-PFR is freely accessible to the public at www.csbio.sjtu.edu.cn/bioinf/Folding Rate/.

Keywords: Protein Folding Rate; Ensemble Predictor; Fusion Approach; Web-Server; Pred-PFR

1. INTRODUCTION

Knowledge of protein three-dimensional (3D) structures plays an indispensable role in molecular biology, cell biology, biomedicine, and drug design [1]. However, each protein begins as a polypeptide, translated from a sequence of mRNA as a linear chain of amino acids. A protein can function properly only if it is folded into a correct shape or conformation [2]. Failure to fold into the intended 3D structure usually produces inactive proteins with different properties. Although many efforts have been made trying to understand the mechanism of protein folding (see, e.g., [3,4,5,6]), it still remains one of the most challenging problems in molecular biology. In addition to understanding how a protein chain is folded, it is also important to find the folding rates of

proteins from their primary sequences. Protein chains can fold into the functional 3D structures with quite different rates, varying from several microseconds to even an hour [7,8].

Experimentally determining the three dimensional structure of a protein is often very difficult and expensive. However the sequence of that protein is easily known. Therefore, for quite a long time, scientists have tried to use the "least free energy principle" [2,9] to predict the 3D structures of proteins. Unfortunately, owing to the notorious local energy minimum problem, so far it can only be successfully used to address very limited structural characters, such as the handedness tendency and packing arrangement in proteins (see, e.g., [10,11,12]). In the past two decades, various statistical methods have been developed for predicting the structural classes of proteins and their folding patterns according to the sequence information alone (see, e.g., [13,14,15,16,17,18,19,20,21,22,23,24,25,26,27,28] and a review [29]). Encouraged by the results obtained via these statistical approaches, various methods were developed for predicting the folding rates of proteins because the information thus acquired would be very useful for understanding the protein folding mechanism and the sequence-structure-function relationship [8,30]. In this regard, the approaches can be generally categorized into two groups: (1) the prediction of protein folding rates is based on the protein structure information; and (2) the prediction is based on the primary sequence information.

For the first group, the features of proteins are extracted from their 3D structural information and hence the predictions are feasible only after the structures have been determined. Most of the methods in this group tried to derive the statistical significance of the correlation between the protein folding rate and the corresponding structural topological parameters, such as contact order (CO) [31], absolute contact order (Abs_CO) [32], total contact distance (TCD) [33], long-range order (LRO) [34], the fraction of local contact (FLC) [34], the chain

topology parameter (CTP) [35] and the most recent geometric contact number (N_α) [30].

For the second group, the features of proteins are mainly extracted from their primary amino acid sequences, such as the amino acid biochemical properties [36] and the effective folding length (L_{eff}) [8] derived from the sequence-predicted secondary structure. The approaches in the second group are particularly useful when the 3D structural information of the protein concerned is not available.

Although the aforementioned methods in predicting folding rates of proteins each have their own merits, they were all established by focusing on one (or a few) specific feature(s). As is well known, a protein folding system is very complicated that involves many physical and chemical factors. For this kind of complicated biological system, it would be particularly effective to treat it by assembling many individual predictors with each operated based on its own special feature [37,38]. In view of this, the present study was devoted to develop a novel ensemble predictor for predicting the folding rate of a protein chain by incorporating its many different features through an optimal fusion process.

2. MATERIALS AND METHODS

To develop a powerful statistical predictor, the first important thing is to obtain an effective benchmark dataset [39]. To realize this and also for facilitating comparison with the existing prediction methods, we use the benchmark dataset as described below.

2.1. Benchmark Dataset

The large dataset recently constructed by Ouyang and Liang [30] was used in the current study. It contains 80 proteins whose folding rates have been experimentally determined. Of the 80 proteins, 45 belong to the two-state folding behaviors without the visible intermediates while the other 35 belong to the three-state or multi-state folding kinetics that exhibit the obvious intermediate state during the folding process under the experimental conditions. If classified according to their structural classes, 18 are all-α proteins, 32 all-β, and the remaining 30 are $\alpha\beta$ proteins (where $\alpha\beta$ means the mix of α/β and $\alpha+\beta$ [40]). The folding rates of the 80 proteins range from $\ln K_f = -6.9$ to $\ln K_f = 12.9$, spanning more than eight orders of magnitude of K_f. For users' convenience, the benchmark dataset, denoted as $\mathbb{S}_{bench}$, is given in the Online Supporting Information A, which can also be downloaded from the web-site at www.csbio.sjtu.edu.cn/bioinf/FoldingRate/. It is instructive to point out that K_f in $\mathbb{S}_{bench}$ is actually an apparent folding rate constant (see Appendix A). Therefore, to develop a statistical method for predicting K_f of a protein according to its sequence information alone, there is no need to discriminate whether the protein is two-state or multi-state folding.

2.2. Sequence Feature Extraction

As mentioned above, although the features extracted from the 3D structures of proteins are very useful for predicting their folding rates, they can be used only when the corresponding PDB codes are available. Owing to such a limit, in this study we will focus on those features that can be derived from the amino acid sequential information alone, either directly or indirectly.

(a) Amino acid properties. Protein is composed of different amino acids, which show different physical, chemical, and conformational properties and hence may have correlations with the folding rates. In this study, the following four amino acid properties were used: α_c, the propensity to be at the C-terminal of α-helix [41]; β_S, the propensity to form β-strand [41]; τ, the compressibility [42]; and $SASA$, the solvent accessible surface area in an unfolding protein chain [43]. Suppose a protein **P** is expressed by

$$\mathbf{P} = R_1 R_2 R_3 R_4 R_5 R_6 R_7 \cdots R_L \tag{1}$$

where R_1 represents the 1st residue of the protein **P**, R_2 the 2nd residue, and so forth. Thus, the protein's scores in the aforementioned four amino acid properties can be formulated as

$$\Phi_i = \frac{\sum_{j=1}^{L} \Phi_{i,j}}{L} \qquad (i = 1, 2, 3, 4) \tag{2}$$

where L represents the protein length, and

$$\Phi_{i,j} = \frac{\Phi_{i,j}^0}{\mathbf{Max}_j\{\Phi_{i,j}^0\} - \mathbf{Min}_j\{\Phi_{i,j}^0\}} \tag{3}$$
$$(i = 1, 2, 3, 4; \quad j = 1, 2, \cdots, 20)$$

where $\Phi_{i,j}^0$ ($i = 1, 2, 3, 4$) respectively represent the original α_c, β_S, τ, and $SASA$ for the j-th ($j = 1, 2, \cdots, 20$) native amino acid, and their values can be obtained from [41,42,43]; $\mathbf{Max}_j\{\Phi_{i,j}^0\}$ means taking the maximum one among $\Phi_{i,1}^0$, $\Phi_{i,2}^0$, $\cdots$, $\Phi_{i,20}^0$, and $\mathbf{Min}_j\{\Phi_{i,j}^0\}$ the corresponding minimum one. For reader's convenience, the values thus obtained for $\Phi_{i,j}$ ($i = 1, 2, 3, 4; j = 1, 2, \cdots, 20$) (cf. **Eq.3**) are given in **Table 1**.

(b) Protein size effect. Many studies have indicated that the protein chain length L and its fractional powers ($L^{1/2}$, $L^{2/3}$, or $L^{3/5}$) or logarithm $\ln(L)$ have a good correlation with the folding rates, suggesting that

L and its various expressions forms could be useful features for predicting protein folding rates [8,30]. In the present study, $\ln(L)$ was adopted.

(c) Information derived from secondary structure prediction. Given a protein sequence, its secondary structure can be predicted by means of various secondary structure prediction tools. In the present study, based on the information thus obtained by using PSIPRED [44], we have the secondary structure content ratios for the protein **P**, as formulated by

$$\Gamma_\alpha + \Gamma_\beta + \Gamma_C = 1 \tag{4}$$

where Γ_α, Γ_β and Γ_C are the ratios of the α-helix, β-sheet, and coiled-coil residues for the protein **P**. Note that although the secondary structure content contains three components ($\Gamma_\alpha, \Gamma_\beta, \Gamma_C$), they were treated as one feature because of the normalized condition imposed by **Eq.4**. Moreover, based on the secondary structure prediction results, the effective protein folding chain length can be derived, as given by [8]:

$$L_{\text{eff}} = L - L_{\text{H}} + L_{\text{h}} \cdot N_{\text{H}} \tag{5}$$

where L is the total number of amino acids for the entire protein chain; L_H the number of predicted helical conformation residues; N_H the number of predicted helices; and L_{h} the number of an α-helix turn (L_{h} is generally ≤ 4; for a standard α-helix, $L_{\text{h}} = 3.6$). In the current study, L_{h} was set at 3, and $\ln(L_{\text{eff}})$ used as the feature input.

2.3. Prediction Algorithm

According to the above section, we have a set of seven different kinds of specific features, as can be summarized by the following equation:

$$\mathbb{S}_{\text{feature}} = \begin{cases} \Phi_1 = \alpha_c \\ \Phi_2 = \beta_S \\ \Phi_3 = \tau \\ \Phi_4 = \text{SASA} \\ \Phi_5 = \ln(L) \\ \Phi_6 = (\Gamma_\alpha, \Gamma_\beta, \Gamma_C) \\ \Phi_7 = \ln(L_{\text{eff}}) \end{cases} \tag{6}$$

To study the folding rate of a protein chain, the key is to determine K_{f}, the so-called folding rate constant. For reader's convenience, a brief discussion about the role of K_{f} (or its logarithm $\ln K_{\text{f}}$) on the protein folding rate is provided in **Appendix A**. According to **Eq.6**, we can construct the following seven linear regression models for predicting the protein folding rate constants:

$$\ln K_{\text{f}}^{(1)} = a_1 + b_1 \cdot \alpha_c \tag{7.1}$$

$$\ln K_{\text{f}}^{(2)} = a_2 + b_2 \cdot \beta_S \tag{7.2}$$

$$\ln K_{\text{f}}^{(3)} = a_3 + b_3 \cdot \tau \tag{7.3}$$

$$\ln K_{\text{f}}^{(4)} = a_4 + b_4 \cdot \text{SASA} \tag{7.4}$$

$$\ln K_{\text{f}}^{(5)} = a_5 + b_5 \ln(L) \tag{7.5}$$

$$\ln K_{\text{f}}^{(6)} = a_6 + b_{6,1} \cdot \Gamma_\alpha + b_{6,2} \cdot \Gamma_\beta + b_{6,3} \cdot \Gamma_C \tag{7.6}$$

$$\ln K_{\text{f}}^{(7)} = a_7 + b_7 \ln(L_{\text{eff}}) \tag{7.7}$$

where $K_{\text{f}}^{(i)}$ ($i = 1, 2, \cdots, 7$) is the protein folding rate constant predicted based on the i-th specific feature Φ_i (cf. **Eq.6**), while a_i and b_i are the corresponding parameters determined by using the regression analysis on a training dataset such as $\mathbb{S}_{\text{bench}}$. For the details of how to use the regression procedures to determine a_i and b_i, refer to [45]. Note that $K_{\text{f}}^{(6)}$ of **Eq.7.6** is involved with more parameters because the 6-th feature Φ_6 contains three sub-features (cf. **Eq.6**).

All the above seven formulae (**Eqs. 7.1–7.7**) can be used to predict the protein folding rates but they each reflect the effect (s) of only one (or one kind) of specific feature (s). To incorporate the effects from all the seven kinds of features, let us consider the following formulation:

$$\ln K_{\text{f}} = \sum_{i=1}^{7} w_i \ln K_{\text{f}}^{(i)} \tag{8}$$

where w_i is the weight that reflects the impact of the i-th specific feature Φ_i on the protein folding rate. If the impacts of the seven features were the same, we should have $w_i = 1/7$ ($i = 1, 2, \cdots, 7$). Since they are actually not the same, it would be rational to introduce some statistical criterion to reflect their different impacts, as formulated below.

Given a statistical system consisting of N samples, the Pearson Correlation Coefficient (ACC) is defined by

$$\text{PCC} = \frac{\sum_{i=1}^{N} (x_i - \bar{x})(y_i - \bar{y})}{\sqrt{\left[\sum_{i=1}^{N} (x_i - \bar{x})^2\right]\left[\sum_{i=1}^{N} (y_i - \bar{y})^2\right]}} \tag{9}$$

where x_i and y_i are, respectively, the observed and predicted results for the i-th sample, while $\bar{x}$ and $\bar{y}$ the corresponding mean values for the N samples. Since PCC reflects the correlation of the predicted results with the actual ones, its value can be used to

measure the quality of a prediction method. If all the predicted results are exactly the same as the observed ones, we have the perfect correlation of $PCC=1$. For different prediction algorithms, **Eq.9** will yield different values of PCC. Therefore, the weight w_i in **Eq.8** can be formulated as

$$w_i = \frac{PCC(K_f^{(i)})}{\sum_{j=1}^{7} PCC(K_f^{(j)})} \qquad (i = 1, 2, \cdots, 7) \qquad (10)$$

where $PCC(K_f^{(i)})$ is the Pearson Correlation Coefficient (**Eq.9**) obtained with the i-th folding rate predicting formula in **Eq.7** on the benchmark dataset $\mathbb{S}_{bench}$ by the jackknife cross-validation.

The prediction method by fusing the seven individual methods as formulated by **Eq.7** is called the **Pred-PFR** (<u>Pred</u>ictor of <u>P</u>rotein <u>F</u>olding <u>R</u>ate).

3. RESULTS AND DICSUSSIONS

In statistical prediction, the following three cross-validation methods are often used to examine a predictor for its effectiveness in practical application: independent dataset test, subsampling test, and jackknife test [40]. However, as elucidated in [38] and demonstrated by **Eq.5** of [39], among the three cross-validation methods, the jackknife test is deemed the most objective that can always yield a unique result for a given benchmark dataset, and hence has been increasingly and widely used by investigators to examine the accuracy of various predictors (see, e.g., [46,47,48,49,50,51,52,53, 54]). To demonstrate the quality of **Pred-PFR**, here let us also use the jackknife cross-validation on the benchmark dataset $\mathbb{S}_{bench}$ (see the Online Supporting Information A).

Now, let us use $PCC(K_f)$ to represent the Pearson Correlation Coefficient (**Eq.9**) obtained with **Pred-PFR** (**Eq.8**) on the benchmark dataset $\mathbb{S}_{bench}$ by the jackknife cross-validation. For facilitate comparison of the ensemble predictor with the individual predictors, the values of $PCC(K_f)$ and those of $PCC(K_f^{(i)})$ $(i = 1, 2, \cdots, 7)$ are given in **Table 2.**

Furthermore, to show the accuracy about the prediction in a more intuitive manner, let us introduce the RMSD (<u>R</u>oot <u>M</u>ean <u>S</u>quare <u>D</u>eviation) as defined by

$$RMSD = \sqrt{\frac{\sum_{i=1}^{N}(x_i - y_i)^2}{N}} \qquad (11)$$

where x_i, y_i and N have the same meanings as **Eq.9**. Obviously, the smaller the value of $RMSD$, the

more accurate the prediction. If all the predicted results are identical to the corresponding observed ones, we have $RMSD = 0$.

Similar to the case of PCC, let us use $RMSD(K_f)$ to represent the value of $RMSD$ obtained with the ensemble predictor **Pred-PFR** (**Eq.8**) on the benchmark dataset $\mathbb{S}_{bench}$ by the jackknife cross-validation, and $RMSD(K_f^{(i)})$ that by the i-th $(i = 1, 2, \cdots, 7)$ formula of **Eq.7**. All these $RMSD$ values are also given in **Table 2**.

As we can see from the table, the overall PCC value yielded by the ensemble prediction formula (**Eq.8**) is 0.88, which is the closest to 1 in comparison with those by the individual prediction formulae (**Eqs 7.1−7.7**). Such an overall PCC value is even higher than that by the prediction method using the 3D structural information [30] on the same benchmark dataset. Moreover, it can be seen from **Table 2** that the overall RMSD value generated by the ensemble prediction formula is the lowest one in comparison with those by the seven individual prediction formulae. The highest correlation and lowest deviation results indicate that the **Pred-PFR** ensemble predictor formed by the fusing approach is indeed more powerful than the individual predictors.

4. CONCLUSIONS

Pred-PFR is developed for predicting the folding rate of a protein based on its sequence information alone. It is an ensemble predictor formed by fusing multiple individual predictors with each based on one special feature. As expected, the ensemble predictor is superior to the individual predictors. The web-server for **Pred-PFR** is freely accessible to the public at <u>www.csbio.sjtu.edu.cn/bioinf/FoldingRate/</u>.

5. ACKNOWLEDGEMENTS

APPENDIX A. THE PROTEIN FOLDING RATE CONSTANT K_f

For a given protein, its folding rate is generally reflected by the apparent rate constant K_f as defined by the following differential equation

$$\begin{cases} \dfrac{dP_{unfold}(t)}{dt} = -K_f P_{unfold}(t) \\ \dfrac{dP_{folded}(t)}{dt} = K_f P_{unfold}(t) \end{cases} \qquad (A1)$$

Table 1. The values of the four amino acid properties that have been normalized according to the Max-Min normalization procedure of Eq.3. For more explanation about the four amino acid properties, see the relevant text.

Amino acid code		α_c	β_s	τ	SASA
Single letter	Numerical index j	$\Phi_{1,j}$	$\Phi_{2,j}$	$\Phi_{3,j}$	$\Phi_{4,j}$
A	1	0.58	0.82	0.34	0.21
C	2	0.20	0.25	0.61	0.56
D	3	0.96	0.23	0.12	0.20
E	4	0.90	0.00	0.00	0.29
F	5	0.34	0.12	0.75	0.84
G	6	0.12	0.70	0.28	0.00
H	7	0.09	0.33	0.37	0.51
I	8	0.16	0.33	0.92	0.79
K	9	0.11	0.29	0.27	0.35
L	10	0.10	0.33	0.69	0.69
M	11	0.18	0.38	0.51	0.83
N	12	0.30	0.40	0.39	0.24
P	13	1.00	1.00	0.13	0.23
Q	14	0.45	0.27	0.54	0.39
R	15	0.00	0.73	0.42	0.58
S	16	0.23	0.48	0.28	0.15
T	17	0.47	0.38	0.61	0.27
V	18	0.13	0.42	1.00	0.57
W	19	0.56	0.45	0.75	1.00
Y	20	0.18	0.08	0.82	0.82

Table 2. The jackknife test results by using different formulae on the benchmark dataset S_{bench} (see the Online Supporting Information A). [a]Note that PCC may also have negative value (see Eq.9). However, the correlation strength of the predicted results with the observed ones is generally measured by its absolute value.

Prediction formula	PCC [a] (cf. Eq.9)	RMSD (cf. Eq.12)
$\ln K_f^{(1)}$ (see Eq.7.1)	-0.68	3.16
$\ln K_f^{(2)}$ (see Eq.7.2)	0.27	4.17
$\ln K_f^{(3)}$ (see Eq.7.3)	-0.52	3.71
$\ln K_f^{(4)}$ (see Eq.7.4)	-0.39	3.99
$\ln K_f^{(5)}$ (see Eq.7.5)	0.79	2.67
$\ln K_f^{(6)}$ (see Eq.7.6)	0.29	4.14
$\ln K_f^{(7)}$ (see Eq.7.7)	0.85	2.23
$\ln K_f$ (see Eq.8)	**0.88**	**2.03**

where $P_{unfold}(t)$ and $P_{folded}(t)$ represent the concentrations of its unfolded state and folded state, respectively. Suppose the total protein concentration is C_0, and initially only the unfolded protein is present; i.e., $P_{unfold}(t) = C_0$ and $P_{folded}(t) = 0$ when $t = 0$. Subse-quently, the protein system is subjected to a sudden change in temperature, solvent, or any other factor that causes the protein to fold. Obviously, the solution for **Eq.A1** is

$$\begin{cases} P_{unfold}(t) = C_0 \exp(-K_f t) \\ P_{folded}(t) = C_0 \left[1 - \exp(-K_f t)\right] \end{cases} \quad (A2)$$

It can be seen from the above equation that the larger the K_f, the faster the folding rate will be. However, the

actual process is much more complicated than the one as described by **Eq.A1** even if the system concerned consists of only two states. The reason is the folded state may reverse back to the unfolded state, as described by the following equation

$$P_{unfold} \underset{k_{21}}{\overset{k_{12}}{\rightleftharpoons}} P_{folded} \quad (A3)$$
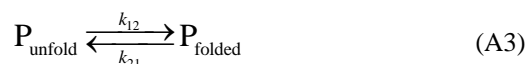
where k_{12} is the forward rate constant for P_{unfold} converting to P_{folded}, and k_{21} is the corresponding reverse rate constant. Thus we have the following kinetic equation

$$\begin{cases} \dfrac{dP_{unfold}(t)}{dt} = -k_{12}P_{unfold}(t) + k_{21}P_{folded}(t) \\ \dfrac{dP_{folded}(t)}{dt} = -k_{21}P_{folded}(t) + k_{12}P_{unfold}(t) \end{cases} \quad (A4)$$

Eqs. A3 and **A4** can be expressed by an intuitive graph called directed graph or digraph $\mathbb{G}$ [55,56] as shown in **Fig.1a**. To reflect the variation of the concentrations of unfolded and folded proteins with time, the digraph $\mathbb{G}$ is further transformed to the phase digraph $\tilde{\mathbb{G}}$ as shown in **Fig.1b**, where s is an interim parameter associated with the following Laplace transform

$$\begin{cases} \tilde{P}_{unfold}(s) = \int_0^\infty P_{unfold}(t)\exp(-ts)\,dt \\ \tilde{P}_{folded}(s) = \int_0^\infty P_{folded}(t)\exp(-ts)\,dt \end{cases} \quad (A5)$$

$$\begin{aligned} \frac{dP_{folded}(t)}{dt} &= k_{12}C_0\exp\left[-(k_{12}+k_{21})t\right] \\ &= (k_{12}+k_{21})P_{unfold}(t) - k_{21}C_0 \\ &= \left\{\frac{k_{12}(k_{12}+k_{21})}{k_{21}+k_{12}\exp\left[-(k_{12}+k_{21})t\right]}\exp\left[-(k_{12}+k_{21})t\right]\right\}P_{unfold}(t) \end{aligned} \quad (A7)$$

Comparing **Eq.A7** with **Eq.A1**, we obtain the following equivalent relation

$$K_f \Leftrightarrow \left\{\frac{k_{12}(k_{12}+k_{21})}{k_{21}+k_{12}\exp\left[-(k_{12}+k_{21})t\right]}\exp\left[-(k_{12}+k_{21})t\right]\right\} \quad (A8)$$

meaning: the apparent folding rate constant K_f is a function of not only the detailed rate constants, but also t. Accordingly, K_f is actually not a constant but will change with time. Only when $k_{12} \gg k_{21}$ and $k_{12} \gg 1$,

Figure 1. (a) The directed graph or digraph $\mathbb{G}$ [55,56] for the two-state protein folding mechanism as schematically expressed in Eq.A3 and formulated in Eq.A4. **(b)** The phase digraph $\tilde{\mathbb{G}}$ obtained from $\mathbb{G}$ of panel **(a)** according to the graphic rule 4 [55,56], which is also called "Chou's graphic rule for non- steady-state enzyme kinetics" in the literature (see, e.g., [57]). The symbol s in panel **(b)** is an interim parameter (see Eq.A5) and the related text for further explanation).

where $\tilde{P}_{unfold}$ and $\tilde{P}_{folded}$ are the phase concentrations of P_{unfold} and P_{folded}, respectively [55,56]. Thus, using the graphic rule 4 [55,56], also called "Chou's graphic rule for non-steady-state enzyme kinetics" [57], we can immediately obtain the solutions of **Eq.A4**, as given by

$$\begin{cases} P_{unfold}(t) = \dfrac{k_{21}C_0}{k_{12}+k_{21}} + \dfrac{k_{12}C_0}{k_{12}+k_{21}}\exp\left[-(k_{12}+k_{21})t\right] \\ P_{folded}(t) = \dfrac{k_{12}C_0}{k_{12}+k_{21}} - \dfrac{k_{12}C_0}{k_{12}+k_{21}}\exp\left[-(k_{12}+k_{21})t\right] \end{cases} \quad (A6)$$

Accordingly, it follows

can **Eq.A8** be reduced to $K_f \simeq k_{12}$ and **Eq.A6** to

$$\frac{dP_{folded}(t)}{dt} \simeq k_{12}P_{unfold}(t) = K_f P_{unfold}(t) \quad (A9)$$

and K_f be treated as a constant.

It can be imagined that for a three-state or multi-state folding system, K_f will be much more complicated. We can also see from the above derivation that using graphic analysis to deal with kinetic systems is quite efficient and intuitive, particularly in dealing complicated kinetic systems. For more discussions about graphic analysis and its applications to kinetic systems, see [55,58,59,60,61,62].

REFERENCES

[1] Chou, K. C. (2004) Review: Structural bioinformatics and its impact to biomedical science. Current Medicinal Chemistry, **11,** 2105–2134.

[2] Anfinsen, C. B. and Scheraga, H. A. (1975) Experimental and theoretical aspects of protein folding. Adv Protein Chem, **29,** 205–300.

[3] Chou, K. C., Nemethy, G., Pottle, M. S. and Scheraga, H. A. (1985) The folding of the twisted beta-sheet in bovine pancreatic trypsin inhibitor. Biochemistry, **24,** 7948–7953.

[4] Creighton, T. E. (1990) Protein folding. Biochem J, **270,** 1–16.

[5] Creighton, T. E. (1995) Protein folding. An unfolding story. Curr Biol, **5,** 353–356.

[6] Scheraga, H. A. (2008) From helix-coil transitions to protein folding. Biopolymers, **89,** 479–485.

[7] Goldberg, M. E., Semisotnov, G. V., Friguet, B., Kuwajima, K., Ptitsyn, O. B. and Sugai, S. (1990) An early immunoreactive folding intermediate of the tryptophan synthease beta 2 subunit is a 'molten globule'. FEBS Lett,

263, 51–56.

[8]   Ivankov, D. N. and Finkelstein, A. V. (2004) Prediction of protein folding rates from the amino acid sequence-predicted secondary structure. Proc Natl Acad Sci USA, **101,** 8942–8944.

[9]   Anfinsen, C. B. (1973) Principles that govern the folding of protein chains. Science, **181,** 223–230.

[10] Chou, K. C. and Scheraga, H. A. (1982) Origin of the right- handed twist of beta-sheets of poly-L-valine chains. Proceedings of National Academy of Sciences, USA, **79,** 7047–7051.

[11] Chou, K. C., Nemethy, G. and Scheraga, H. A. (1984) Energetic approach to packing of a-helices: 2. General treatment of nonequivalent and nonregular helices. Journal of American Chemical Society, **106,** 3161–3170.

[12] Chou, K. C., Maggiora, G. M., Nemethy, G. and Scheraga, H. A. (1988) Energetics of the structure of the four-alpha-helix bundle in proteins. Proceedings of National Academy of Sciences, USA, **85,** 4295–4299.

[13] Klein, P. and Delisi, C. (1986) Prediction of protein structural class from amino acid sequence. Biopolymers, **25,** 1659–1672.

[14] Chou, K. C. and Zhang, C. T. (1992) A correlation coefficient method to predicting protein structural classes from amino acid compositions. European Journal of Biochemistry, **207,** 429–433.

[15] Zhang, C. T. and Chou, K. C. (1992) An optimization approach to predicting protein structural class from amino acid composition. Protein Science, **1,** 401–408.

[16] Chou, J. J. and Zhang, C. T. (1993) A joint prediction of the folding types of 1490 human proteins from their genetic codons. Journal of Theoretical Biology, **161,** 251–262.

[17] Chou, K. C. and Zhang, C. T. (1994) Predicting protein folding types by distance functions that make allowances for amino acid interactions. J Biol Chem, **269,** 22014–22020.

[18] Dubchak, I., Muchnik, I., Holbrook, S. R. and Kim, S. H. (1995) Prediction of protein folding class using global description of amino acid sequence. Proc Natl Acad Sci U S A, **92,** 8700–8704.

[19] Chou, K. C. (1995) Does the folding type of a protein depend on its amino acid composition? FEBS Letters, **363,** 127–131.

[20] Chou, K. C. (1995) A novel approach to predicting protein structural classes in a (20-1)-D amino acid composition space. Proteins: Structure, Function & Genetics, **21,** 319–344.

[21] Bahar, I., Atilgan, A. R., Jernigan, R. L. and Erman, B. (1997) Understanding the recognition of protein structural classes by amino acid composition. PROTEINS: Structure, Function, and Genetics, **29,** 172–185.

[22] Zhou, G. P. (1998) An intriguing controversy over protein structural class prediction. Journal of Protein Chemistry, **17,** 729– 738.

[23] Ding, C. H. and Dubchak, I. (2001) Multi-class protein fold recognition using support vector machines and neural networks. Bioinformatics, **17,** 349–358.

[24] Zhou, G. P. and Assa-Munt, N. (2001) Some insights into protein structural class prediction. PROTEINS: Structure, Function, and Genetics, **44,** 57–59.

[25] Ding, Y. S., Zhang, T. L. and Chou, K. C. (2007) Prediction of protein structure classes with pseudo amino acid

composition and fuzzy support vector machine network. Protein & Peptide Letters, **14,** 811–815.

[26] Shen, H. B. and Chou, K. C. (2006) Ensemble classifier for protein fold pattern recognition. Bioinformatics, **22,** 1717–1722.

[27] Chen, K. and Kurgan, L. (2007) PFRES: protein fold classification by using evolutionary information and predicted secondary structure. Bioinformatics, **23,** 2843–2850.

[28] Shen, H. B. and Chou, K. C. (2009) Predicting protein fold pattern with functional domain and sequential evolution information. Journal of Theoretical Biology, **256,** 441–446.

[29] Chou, K. C. (2005) Review: Progress in protein structural class prediction and its impact to bioinformatics and proteomics. Current Protein and Peptide Science, **6,** 423–436.

[30] Ouyang, Z. and Liang, J. (2008) Predicting protein folding rates from geometric contact and amino acid sequence. Protein Science, **17,** 1256–1263.

[31] Plaxco, K. W., Simons, K. T. and Baker, D. (1998) Contact order, transition state placement and the refolding rates of single domain proteins. J Mol Biol, **277,** 985–994.

[32] Ivankov, D. N., Garbuzynskiy, S. O., Alm, E., Plaxco, K. W., Baker, D. and Finkelstein, A. V. (2003) Contact order revisited: influence of protein size on the folding rate. Protein Science, **12,** 2057–2062.

[33] Zhou, H. and Zhou, Y. (2002) Folding rate prediction using total contact distance. Biophys Journal, **82,** 458–463.

[34] Gromiha, M. M. and Selvaraj, S. (2001) Comparison between long-range interactions and contact order in determining the folding rate of two-state proteins: application of long-range order to folding rate prediction. J Mol Biol, **310,** 27–32.

[35] Nolting, B., Schalike, W., Hampel, P., Grundig, F., Gantert, S., Sips, N., Bandlow, W. and Qi, P. X. (2003) Structural determinants of the rate of protein folding. J Theor Biol, **223,** 299–307.

[36] Gromiha, M. M., Thangakani, A. M. and Selvaraj, S. (2006) FOLD-RATE: prediction of protein folding rates from amino acid sequence. Nucleic Acids Res, **34,** W70–74.

[37] Wang, D., Keller, J. M., Carson, C. A., McAdo-Edwards, K. K. and Bailey, C. W. (1998) Use of fuzzy-logic-inspired features to improve bacterial recognition through classifier fusion. IEEE Trans Syst Man Cybern B Cybern, **28,** 583–591.

[38] Chou, K. C. and Shen, H. B. (2008) Cell-PLoc: A package of web-servers for predicting subcellular localization of proteins in various organisms. Nature Protocols, **3,** 153–162.

[39] Chou, K. C. and Shen, H. B. (2007) Review: Recent progresses in protein subcellular location prediction. Analytical Biochemistry, **370,** 1–16.

[40] Chou, K. C. and Zhang, C. T. (1995) Review: Prediction of protein structural classes. Critical Reviews in Biochemistry and Molecular Biology, **30,** 275–349.

[41] Chou, P. Y. and Fasman, G. D. (1978) Prediction of secondary structure of proteins from amino acid sequences.

Advances in Enzymology and Related Subjects in Biochemistry, **47,** 45–148.

[42] Iqbal, M. and Verrall, R. E. (1988) Implications of protein folding. Additivity schemes for volumes and compressibilities. J Biol Chem, **263,** 4159–4165.

[43] Oobatake, M. and Ooi, T. (1993) Hydration and heat stability effects on protein unfolding. Prog Biophys Mol Biol, **59,** 237–284.

[44] Jones, D. T. (1999) Protein secondary structure prediction based on position-specific scoring matrices. J Mol Biol, **292,** 195–202.

[45] Chou, K. C. (1999) Using pair-coupled amino acid composition to predict protein secondary structure content. Journal of Protein Chemistry, **18,** 473–480.

[46] Zhou, X. B., Chen, C., Li, Z. C. and Zou, X. Y. (2007) Using Chou's amphiphilic pseudo-amino acid composition and support vector machine for prediction of enzyme subfamily classes. Journal of Theoretical Biology, **248,** 546–551.

[47] Ding, Y. S. and Zhang, T. L. (2008) Using Chou's pseudo amino acid composition to predict subcellular localization of apoptosis proteins: an approach with immune genetic algorithm-based ensemble classifier. Pattern Recognition Letters, **29,** 1887–1892.

[48] Zhang, G. Y., Li, H. C. and Fang, B. S. (2008) Predicting lipase types by improved Chou's pseudo-amino acid composition. Protein & Peptide Letters, **15,** 1132–1137.

[49] Lin, H. (2008) The modified Mahalanobis discriminant for predicting outer membrane proteins by using Chou's pseudo amino acid composition. Journal of Theoretical Biology, **252,** 350–356.

[50] Li, F. M. and Li, Q. Z. (2008) Predicting protein subcellular location using Chou's pseudo amino acid composition and improved hybrid approach. Protein & Peptide Letters, **15,** 612– 616.

[51] Zhang, G. Y. and Fang, B. S. (2008) Predicting the cofactors of oxidoreductases based on amino acid composition distribution and Chou's amphiphilic pseudo amino acid composition. Journal of Theoretical Biology, **253,** 310–315.

[52] Lin, H., Ding, H., Feng-Biao Guo, F. B., Zhang, A. Y. and Huang, J. (2008) Predicting subcellular localization of mycobacterial proteins by using Chou's pseudo amino acid composition. Protein & Peptide Letters, **15,** 739–744.

[53] Munteanu, C. R., Gonzalez-Diaz, H., Borges, F. and de Magalhaes, A. L. (2008) Natural/random protein classification models based on star network topological indices. Journal of Theoretical Biology, **254,** 775–783.

[54] Rezaei, M. A., Abdolmaleki, P., Karami, Z., Asadabadi, E. B., Sherafat, M. A., Abrishami-Moghaddam, H., Fadaie, M. and Forouzanfar, M. (2008) Prediction of membrane protein types by means of wavelet analysis and cascaded neural networks. Journal of Theoretical Biology, **254,** 817–820.

[55] Chou, K. C. (1989) Graphical rules in steady and non-steady enzyme kinetics. J Biol Chem, **264,** 12074–12079.

[56] Chou, K. C. (1990) Review: Applications of graph theory to enzyme kinetics and protein folding kinetics. Steady and non- steady state systems. Biophysical Chemistry, **35,** 1–24.

[57] Lin, S. X. and Neet, K. E. (1990) Demonstration of a slow conformational change in liver glucokinase by fluorescence spectroscopy. J Biol Chem, **265,** 9670–9675.

[58] Chou, K. C. and Liu, W. M. (1981) Graphical rules for non-steady state enzyme kinetics. Journal of Theoretical Biology, **91,** 637–654.

[59] Zhou, G. P. and Deng, M. H. (1984) An extension of Chou's graphical rules for deriving enzyme kinetic equations to system involving parallel reaction pathways. Biochemical Journal, **222,** 169–176.

[60] Myers, D. and Palmer, G. (1985) Microcomputer tools for steady-state enzyme kinetics. Bioinformatics (original: Computer Applied Bioscience), **1,** 105–110.

[61] Kuzmic, P., Ng, K. Y. and Heath, T. D. (1992) Mixtures of tight- binding enzyme inhibitors. Kinetic analysis by a recursive rate equation. Anal Biochem, **200,** 68–73.

[62] Andraos, J. (2008) Kinetic plasticity and the determination of product ratios for kinetic schemes leading to multiple products without rate laws: new methods based on directed graphs. Canadian Journal of Chemistry, **86,** 342–357.

Assessment of bone condition by acoustic emission technique: A review

Sharad Shrivastava[1], Ravi Prakash[1]

[1]Birla Institute of Technology and Science, Pilani, India.
Email: sharadiitkgp@gmail.com, raviprakash.ravi@gmail.com

ABSTRACT

The paper deals with the review of acoustic emission technique in biomedical field. The review is done with the aim to provide an overview of the use of AE technique in biomedical field, mainly concentrated on the AE behavior of bone under different loading conditions, its dependence on strain rate, in osteoporosis, monitoring the fracture healing process of bone. The overall conclusion from the review was that almost all the studies in bone indicated that the initial AE occurs only in the plastic region and just prior to yield. That means the use of AE technique for clinical application cannot be considered as a safe technique, but the early occurrence of AE events from callus promises the application of AE technique for monitoring the fracture healing process. The negligible effect of soft tissues on AE response of bone promises AE to become a non-invasive method for assessment of bone condition.

Keywords: Acoustic Emission; Assessment; Strain Rate; Callus; Fracture Healing; Osteoporosis

1. INTRODUCTION

Bone is primary structural element of human body. The anatomy of human beings is quite well known but the strength and mechanical properties of bones have not been investigated thoroughly. The 206 named bones of skeleton constitutes 18% of the adult human body weight, only skin and fat (25%) and muscles (43%) being greater [1]. In biological terms bone is described as a connective tissue and in mechanical terms bone is a composite material with several distinct solid and fluid phases. The mechanical properties of bone have been more extensively investigated than those of any other biological tissue materials. Although our understanding of the mechanical properties and fracture behavior of bone is continuously improving, as yet it is far from complete. As pointed by Hayes, W. C. [2] while fundamental research is needed on many aspects of the mechanical response of the bone, applications of the techniques of analytical and experimental mechanics in this area are made complicated by the fact that bone is highly complex living material.

The initial work in the field of bone biomechanics can be traced back to the 17th century when "attempts to express biological findings in physical terms" [3] were made by the scholars at that time. This philosophical background of the aspect was intensified in the age of determinism which lasted until the middle of the 19th century. One of the main aspects of the research work in that time was to relate the architecture of bone and its mechanical functions. In the year 1832, Bourgery, J. M. [4] in his work on anatomy raised the question of relation between architecture and mechanical functions of bone. In his book on osteology, Ward, F. O. [5] compared the proximal end of the human femur with a crane and he mentioned the compressive and tensile stresses evoked in the bone by loading. In the year 1867, a more detailed analysis of the structure of cancellous bone and its mathematical significance was given by Meyer, G. H. [6] in association with the famous mathematician Culmann.

The industrial revolution took place in the second half of the 19th century. It had an impact on the research works in the bone also. New developments were made in the field of material testing and the new methods were developed for mechanical measurements. For a while, these methods were used to determine the in vitro mechanical properties of bone. The bones were tested under various loading conditions and the ultimate strength of bone was determined by many investigators [7,8,9,10,11, 12,13,14,15,16,17,18]. Mc Elhaney, J. H. [19] from his study on the strain rate dependence of the mechanical properties of bone showed that both the compressive strength and modulus of longitudinally oriented compact bone specimens were significantly increased by increasing the strain rate. A critical strain rate for bone has been

claimed in compression [19], torsion [20] and tension [21]. However Wright, T. M. and Hayes, W. C. [22] found no critical strain rate in tensile tests of bovine bone over a wide strain-rate range.

In the last few decades attempts were made to use the newly developed/improved non-destructive testing techniques to find the mechanical properties of in vivo and in vitro bones. Those include finding the elastic constants using ultrasonic techniques [23,24,25,26], finding the mechanical strength of bone specimens by X-ray computed tomography, etc.

Assessment of in vivo bone condition is one of the research areas, which have attracted many biomedical engineers and clinical orthopaedicians in recent times. Presently the radiological examination is widely used for the assessment of in vivo bone condition [27,28]. In some clinical problems such as diagnosis of the point of clinical union of fracture, the manual assessment of stability is also used along with the radiological examination. However for many applications the radiographic technique was found to be suffered from low sensitivity. For instance, for the evaluation of osteoporosis it requires a minimum loss of 30% or more of bone mineral content before an unequivocal roentgen logical diagnosis can be made [29].

Monitoring the fracture healing process is another area where the currently used techniques failed to give satisfactory results. Uncertainty regarding the significance of the radiographic and clinical findings may result in unnecessarily long immobilization periods which can produce discomfort and inconvenience for the patients, as well as possible joint stiffness and even permanent loss of motion especially in the elderly.

In certain long bone shaft fractures the healing process is modified by the method of treatment so that the clinical assessment of mechanical integrity is impossible and the interpretation of radiographs may be difficult.

Diaphyseal fractures treated by "rigid" internal fixation always demonstrated this problem, since the fracture cannot be tested mechanically and external callus formation is not seen on radiographs, methods are needed to assess the mechanical integrity of fracture healing in such circumstances, or an unreliable and unsafe rehabilitation programme may be prescribed.

Mechanical impedance, natural frequency, vibration analysis, stress wave propagation, ultrasonic- measurements, impact response technique, electrical potential measurements and mechanical tissue response analysis are some of the techniques, which have been attempted by different investigators for the assessment of in vivo bone condition in the past [30,31,32,33,34,35,36,37,38, 39,40]. However, in all these studies, the intervening soft tissues, whose quantity and quality changes with individual to individual, affected the results. Furthermore some methods were not really non-invasive in nature and some were not practicable for widespread clinical use because of low reliability and complicated instrumentation.

The structure of bone is very much similar to engineering composite materials and is therefore advantageous to use a non-destructive testing technique, which has already proved it usefulness in the field of composite materials testing. Acoustic emission (AE) technique has been used very successfully for the non-destructive evaluation of composites. The relationship between AE response and mechanical behavior in composite materials has been extensively studied in the past [41]. This paper deals with the review of AE technique which is to be used for bone assessment. The review has been broadly classified as follows (**Figure 1**).

2. ACOUSTIC EMISSION TECHNIQUE

The AE technique is the sound produced by materials as they fail. A familiar example is the audible cracking
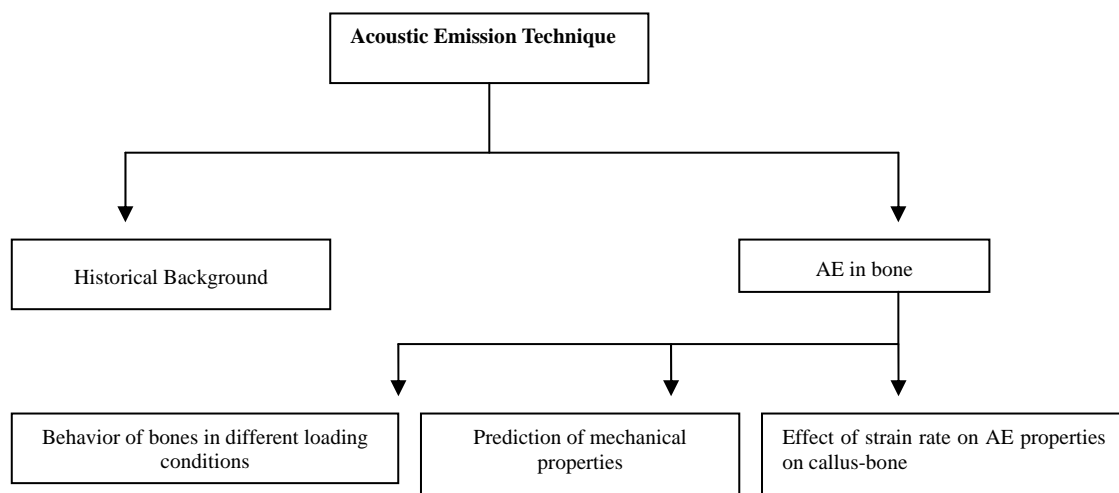
Figure 1. Broad classification of the review study.

noise from wood. Almost all engineering materials generate acoustic emissions but unlike wood, the sound is too faint to be heard without sensitive electronic monitors. Acoustic emission waves can be detected by means of remote piezoelectric sensors and their source can be located by timing the wave arrival at several sensors. Thus AE provides a unique method of recognizing when and where deformation is taking place as a structure is stressed.

The first systematic investigations of AE phenomenon was made in 1950 by Kaiser, J. [42] at the technical university of Munich. In his investigations, the noise emitted by the deformation of materials was examined by means of electronic equipment capable of detecting inaudible ultrasonic signals. Kaiser, while working with polycrystalline specimens concluded that acoustic vibrations originate in grain boundary interfaces and was believed to be associated with the interaction induced between interfaces by applied stresses. He noted that, for a given materials, characteristics spectra of frequency and amplitude existed. One of the important observations made in his study was that irreversible processes were involved with AE phenomenon; an effect later came to be known as Kaiser Effect. The universality of the AE phenomenon, as recognized by Kaiser, leads to a very wide range of applicability. AE has been recorded from hundreds of materials-metals, composites, ceramics, plastics, glasses, building materials, biological materials in vitro and in vivo as well as from multi material structures and joints between different materials [43]. Compared to other NDT techniques which rely on extraneous energy for the illumination of defect; AE enjoys the unique feature that the defect makes its own signal. This leads to a natural complementary between AE and other methods.

3. ACOUSTIC EMISSION DETECTION AND SIGNAL PROCESSING

Figure 2 [44] shows the method of detection of acoustic emission events by remote piezoelectric transducers. Here, an AE source generates an expanding spherical
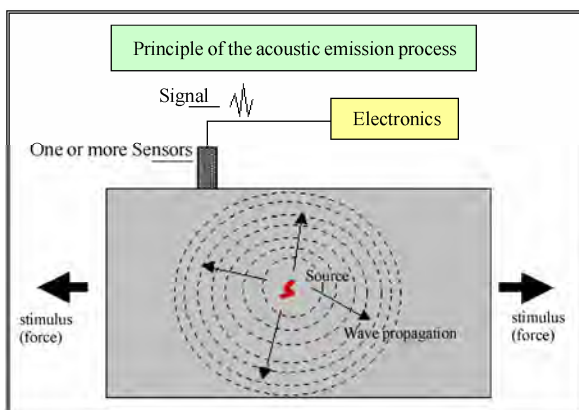
Figure 2. Detection of acoustic emission event by remote piezoelectric transducers (source: 44).

wave packet losing intensity at a rate of r^{-2}. When this wave reaches the body boundary, a surface wave packet is created, either Rayleigh or Lamb wave type depending on the thickness. This method is mainly used for flaw monitoring in inaccessible areas. The individual signal has a short duration at the source and a corresponding broad spectrum which typically extends from zero frequency to many megahertz. The form of the signal at the point of detection is a damped oscillation, developed in the structure according to known principles of acoustic wave propagation. **Figure 3** [44] shows the signal waveform of one acoustic emission event and different parameters normally measured to characterize the acoustic emission source.

4. ACOUSTIC EMISSION IN BONE

Hanagud, S., *et al.* [45] using bovine femora first demonstrated detectable acoustic emissions from bone. His work made the way for other investigators to use the AE technique for characterization of bone and also to explore the possibilities of using it as a tool for clinical orthopaedicians to detect bone abnornamilities [46,47,48, 49,50]. Knet-s, I. V., *et al.* [46] has shown that the character of the fracture surface depends on the orientation of the load relative to the direction of the osteons, the rate of loading, and the geometrical shape of the actual sample. They concluded that the most promising approach in testing the internal state of a bone is acoustic emission, sometimes also known as the method of stress-wave emission. This approach involves recording of deformation noise in the material due to the development and further propagation of structural defects. These defects may include dislocations or cracks appearing in the course of loading. This study was the first work to visualize the degree of micro cracks development in bone tissue subjected to longitudinal extension. This experimental work was only visualized for longitudinal loading and the deformation rate considered was also very low (1 mm/min). The study was not conducted for higher strain rates. In another investigation Hanagud, S., *et al.* [50] conducted AE tests on carefully prepared bone specimens subjected to bending loads. Their specimen included femur from cattle and cadavers. They compared the AE patterns from 60 perfect and defective specimens. The result clearly indicated that the development of an effective early diagnostic tool for osteoporosis was possible by using AE technique.

Thomas, R. A., *et al.* [51] studied the acoustic emissions from fresh bovine femora and its clinical applications. They employed a more sophisticated set up of AE technique by including both amplitude and pulse width distribution to investigate whole fresh bovine femora which were loaded by compression and bending. They found that both the amplitude distribution and pulse width distribution results of fresh bone had clearly shown characteristic spectra which could be used for the early detection of bone abnormalities such as fracture and osteoporosis.
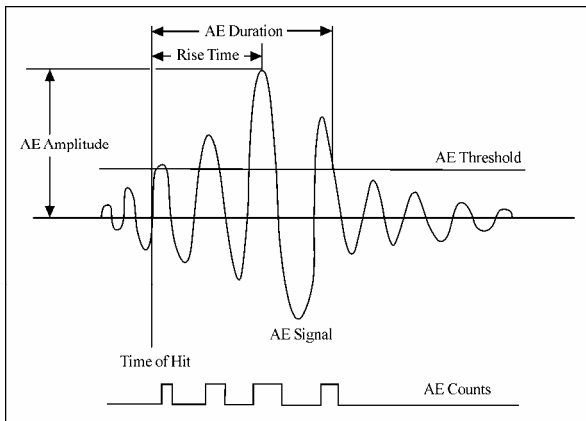
Figure 3. Signal waveform for one acoustic emission event (source: 44).

Yoon, H. S., *et al.* [52] developed a new AE technique for applications to human and animals both non-invasively and non-traumatically. Bones from several different species of animals and different kinds in the same species were tested to obtain AE parameters. Their results indicated that the AE amplitude distributions of all the bones are similar, somewhat independent of the species of animals and kind in the same species and however different from those of those materials such as metals, ceramics and plastics. The technique was found useful for the diagnosis of micro fractures, such as stress fractures in the tibia of runners, which were not detectable by conventional X-ray technique until they begun to heal. Moreover conventional techniques would require introducing some additional stresses in to the part of the body under examination, which also introduces additional trauma to the patient. In their technique the low intensity ultrasonic pulses were injected through an AE transducer, instead of applying loads to the bone under tests. The loading as pulses reduced the introduction of trauma to the live subject. Another receiving AE transducer was used to collect five types of useful AE data: per-event- distribution of counts, peak amplitude, energy and pulse duration, and cumulative counts vs time.

Netz, P. [53] monitored the AE response of canine femora in torsion at 6 degrees per second. His work demonstrated that the AE events occur in the non-linear plastic portion of the load deflection curve. Wright, T. M., *et al.* [54] monitored the permanent deformation of compact bone using AE technique. Uniaxial tension tests were performed on standardized specimens of bovine harvesian bone to examine the contributions of mineral and collagen to permanent deformation in bone and to monitor the damage mechanisms occurring in permanent deformation using AE technique. Their results were consistent with a two-phase model for bone in which the mineral behaves as an elastic-perfectly plastic material when bound to the collagen fiber matrix. The AE events occurred just prior to the yield point and continued during yielding. Significant AE counts occurred again just

prior to fracture. No emissions occurred in the elastic region and few occurred in the major portion of plastic region between yield and fracture. To monitor micro cracks in the specimen they used AE and plotted graphs. **Figures 4,5** [54] show stress vs. strain and cumulative acoustic emission counts vs. strain curves for one of the control specimens and decalcified specimens. These graphs indicate the similarity between the acoustic emission data of the bones prior to fracture. **Figure 6** [54] shows stress strain plots based on the mean values from **Table 1** [54]. The limitation of their work lies in the hy pothesis that the mineral only exhibit elastic-perfectly plastic behavior in conjunction with collagen. They conducted experiments on control, decalcified and deprotenised groups of specimens with the same hypothesis. The fact is that the deprotenised groups of specimens behave in brittle manner. Hence they suggested further studies to be undertaken to examine the contributions of mineral and collagen for permanent deformation in the bone. The two phase model used could be used to study the quasistatic tensile behavior of compact bone but more work could have been carried out for higher strain rates responses before coming to any conclusion.
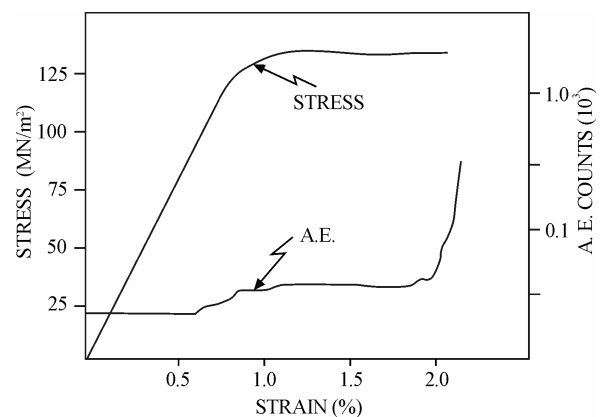
**Figure 4.** Stress vs strain and acoustic emission counts vs strain curves for one of the control specimens (source: 54).
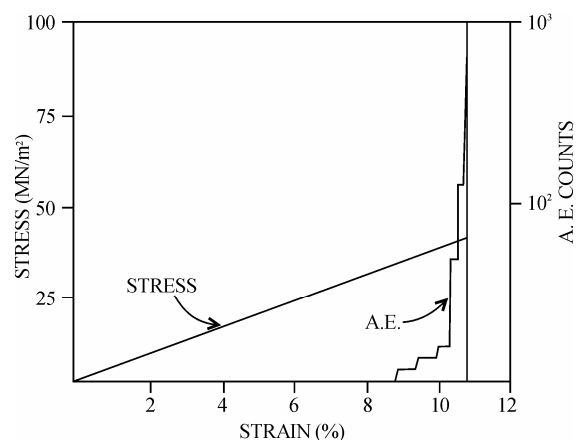

Figure 5. Stress vs strain and acoustic emission counts vs strain curves for one of the decalcified specimens (source: 54).
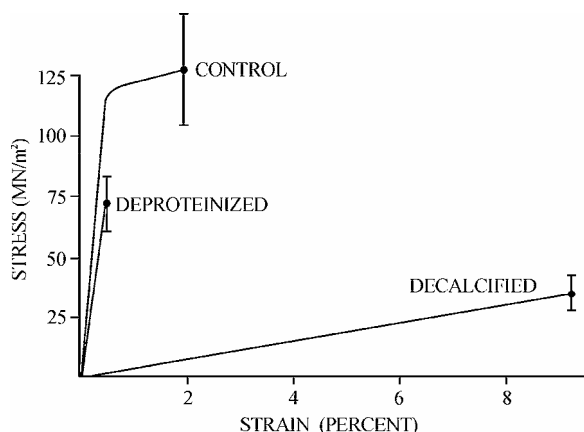
Figure 6. Stress-strain curves for the three test groups constructed from the mean values in Table 1. Error bars are shown for ultimate stress values (source: 54).

Table 1. Mechanical properties of decalcified and partially deproteinized bovine bones (source: 54).

	control	decalcified	Deproteinized
No of specimens	7	11	10
Yield stress	118(9.8)	-	-
Yield strain	0.544(0.150)	-	-
Ultimate stress	128(15.6)	34(7.5)	71(11.5)
Ultimate strain	2.02(0.924)	9.247(1.524)	0.956(0.342)
Elastic modulus	20.6(2.76)	0.37(0.05)	11.3(3.15)
Plastic modulus	0.66(0.357)	-	-

It is an established fact that the ultimate tensile strength of bone is dependent on the applied strain rate. Based on these Fisher, R. A., *et al.* [55] studied the effect of using two different strain rates on the AE in bones. In their work bovine cortical bone was milled in to standard tensile specimens which were tested at two different strain rates while being monitored with AE equipment. They found that the amplitude distribution of the AE events in bone is dependent on strain rate. Greater number of events occurred with the slower strain rate but the events were of lower amplitude than those emitted during the more rapid strain rate. Here also the initial AE occurred well in to the plastic region of the stress-strain curve near the point of fracture of the tensile specimens. It was evident from the study that if acoustic emission technology is to be utilized clinically for the assessment of fracture healing; careful selection of rate of loading would be necessary. Furthermore the study indicated that acoustic emission response was different at different strain rates. As the emissions did not occur until failure was imminent, it indicates that Acoustic emission technology is not suitable for evaluating the integrity of bone. The limitation included that the specimens taken were of very large sizes to minimize the stress concentrations effects of normal bone architecture. They did their work at only two different strain rates (0.0001/s and 0.01/s);

therefore no conclusion could be made for broad range of strain rates.

Later on Nicholls, P. J., *et al.* [56] studied the AE properties of callus. In their work, rabbits with 45 degree midshaft oblique osteotomies were strained in shear while monitoring for AE events. Each fracture remained essentially quiet until over 50% of load to failure had been applied. They suggested that since callus formation during fracture healing takes important role in the healing process, the AE from callus may have clinical applications. The limitation of the study lies in the test method used for evaluating bone. As bone is a non-homogeneous substance, it is very difficult to evaluate with instruments which have been designed for homogeneous substances. A test method should be so designed that eliminates background noise, such as slippage of specimen in the grips and motion of the transducers on the bone surface. This hampers reproducibility of acoustic emission patterns. In most of the AE studies of bone the bone has been tested without the surrounding soft tissues. But in the case of clinical applications of AE, one cannot separate the bone from soft tissues and hence the tests should be performed with soft tissues. Hanagud, S., *et al.* [57] studied these phenomena. They used freshly dissected rabbit tibia and femur with soft tissues. Tests were conducted through bending load. They found that the soft tissues of 2 to 9mm thickness did not affect the bone's AE response.

A study of bone-tissue samples by Martens, M. [58] used acoustic emission for to study the mechanical behavior of femoral bones in bending loading. Ono, K. [59], provided an insight about the fundamental theories and equations related to acoustic emission. Stromsoe, K., *et al.* [60], worked on bending strength of femur using non invasive bone mineral assessment.

The work done till this time demonstrated that the safe use of AE technique for the non-destructive testing of bone is impossible because the AE events occurred only after plastic deformation occurred.

Lentle, B. C. [61], University of British Columbia used acoustic emission to monitor osteoporosis. He devised a method for in vivo diagnosis of patients using AE technique, which could also predict the severity of osteoporosis.

Table 2. The predictive capability of acoustic emissions expressed in terms of the specimen's fatigue life (source: 71).

	Maximum stress(MPa)	N_F Fatigue life [cycles]	NP Fracture onset via AE [cycles]	Predictive Capability [% of fatigue life]
Specimen 1	55	26363	22580	85 %
Specimen 2	61	35020	33382	95 %
Specimen 3	66	4737	2989	63 %
Specimen 4	71	600	402	67 %

Table 3. A statistically significant effect of time on these mechanical properties was detected. Within a row, values with differing letters are significantly different from each other (P<0:05) (Source: 65).

Mechanical properties	weeks after surgery			
	4(n=8)	4(n=8)	4(n=9)	4(n=9)
Tensile Strength (N/mm^2)	36±21a	130±60b	220±32c	510±95d
Tensile Stiffness(N/mm)	0.47±0.18a	1.3±6b	1.8±6b	3.0±2c
Maximum Strain (%)	10±3a	3.7±3b	1.6±0.4b	1.8±0.3b
AE Initiation Load (N)	21±15a	71±3b	150±62c	330±31d
Std. TensileSstrength (N/mm^2)	0.12±0.6a	0.33±0.2b	0.55±0.1c	0.82±0.03d
Std. Tensile Stiffness (N/mm)	0.028±0.02a	0.57±0.3b	0.82±0.3b,c	1.0±0.06c
Std. Maximum Strain	5.6±1.4a	2.2±1b	0.90±0.2b	0.86±0.1b

Table 4. Ash content was calculated by (ash density/apparent density Â 100). A statistically significant effect of time on these mechanical properties was detected. Within a row, values with differing are significantly different from each other letters (P< 0:05) (Source: 65).

Mechanical properties	weeks after surgery			
	4(n=9)	6(n=9)	8(n=10)	12(n=10)
Apparent density (g/cm^3)	0.42±0.07a	0.67±0.07b	1.2±0.1c	1.2±0.08c
Ash density (g/cm^3)	0.14±0.04a	0.40±0.06b	0.82±0.08c	0.88±0.06c
Ash content (%)	33±4a	59±5b	71±1b,c	73±1c

Acoustic emission was being used to predict changes in mechanical properties due to fatigue [62,63,64]. Watanabe, Y., *et al.* [65] used AE technique to predict mechanical properties of fractures. Experimentally produced fractures of femur in rats were tested in tension and in torsion at 4, 6, 8 and 12 weeks after fracture. AE signals were monitored during these mechanical tests. The values for load and torque at the initiation of the AE signal were defined as new mechanical parameters. Tensile strength, tensile stiffness, and torsional stiffness were found to increase with time. They focused on how AE signals can help a surgeon to remove the external fixators in the sense that AE signals can be used to monitor healing of bones. **Table 3** [65] indicates a statistically significant effect of time on these mechanical properties. **Table 4** [65] indicates the calculated ash content and the statistically significant effect of time on the mechanical properties of bone. The data obtained by them were compared to the original values and were found out to be almost the same. The study was a first step towards the establishment of AE testing as a means of predicting the callus strength. The two parameters exhibited strong and positive linear correlation with tensile strength and torque. The linear correlations suggested that it may be possible to use AE technology to evaluate fracture healing process, following osteotomy surgery. There were still many issues which needed to be resolved to make it clinically viable.

Kevin S. C. K., *et al.* [66] developed an acoustical technique for the measurement of structural symmetry of hip joints. Since, these techniques depend very much on the intensity and quality of sounds emitted from the joints under investigation. They developed an acoustical technique for the measurement of relative acoustic transmission across both hips of the test subjects while they were subjected to an external vibratory force applied at the sacrum. The merit of this approach was that it allows direct comparison of the sound signals transmitted across both hips regardless of the measure of the input vibratory force. Simultaneously, other acoustic techniques like scanning acoustic microscopy [67,68] acoustic mapping [69,70] was being used to predict and study mechanical properties of tissues and bone.

Ozan A. [71] worked on a hypothesis that an increase in micro damage activity during repeated loading of bone will signal the approaching stress fracture. Interception with the training regime prior to the incidence of the fracture as signaled by acoustic emissions would reduce the time necessary for recuperation. Acoustic emission was used for real time monitoring of micro cracks. They used acoustic emission technique to predict the failure of cortical bone. **Table 2** [71] indicates the predictive capability of acoustic emissions expressed in terms of the specimen's fatigue life.

Information was collected on all acoustic events, regardless of whether they originated from micro damage or somewhere else and then signals originating from the micro damage were isolated. The rest of the irrelevant signals were filtered out based on their average frequency, duration, amplitude, and intensity. With the non-micro damage signals removed from the data, we were able to determine the number acoustic events related to bone damage as well as the time at which they occurred. Specially designed software is yet to be developed which will segregate the zones of micro damage. Fracture healing and prediction of healing time of fractures were increasingly being studied. A review by Browne, M., *et al.* [72] on acoustic emission's capability to monitor bone degradation and bone fatigue provided us information with latest developments in this field.

In 2004, Franke, R. P., *et al.* [73] used acoustic emission for in vivo diagnosis of the knee joint. For the as-

sessment of the tribological knee function and by the probability of fracture of the femur an adapted Acoustic Emission Measurement System named Bone Diagnostic System (BONDIAS) was developed. This system makes the in vivo analysis of the medical status possible. Different mechanisms of cracking were accompanied by different acoustic emission from human femora as shown in literature. An acoustic emission signal typical of crack initiation is shown in **Figure 7** [73]. This Figure is indicative of the acoustic emission from healthy knee joint cartilage after a sudden change from a two leg stand to a one leg stand. It is characterized by a very short rise time and an exponential decrease of the amplitudes. From the medical point of view such mechanical loads are regarded as non destructive although there is already crack initiation in the interface of the compact and the trabecular system of the bone. These micro cracks seem to be essential for the physiological bone remodeling. For the description of the development of bone strength over time it is necessary to assess both the threshold of crack initiation and the conditions for crack propagation. The sudden change in amplitude indicates high thickness of the cartilage layer. There are several advantages of the diagnostic procedure by AE when compared with established conventional methods:

1) No pain is caused by this procedure.

2) This procedure is non-destructive. Mechanical load even beyond the crack initiation threshold are typical of day to day life and necessary for the physiological bone remodeling to avoid the degeneration of the bone and joint system.

3) There is no health burden through ionizing radiation as is unavoidable with X-ray examination and CT.

4) There is no danger of infection since this is a non-invasive examination.

5) The time required for the assessment of the acoustic emission behavior and analyses of data are of the order of seconds to minutes.
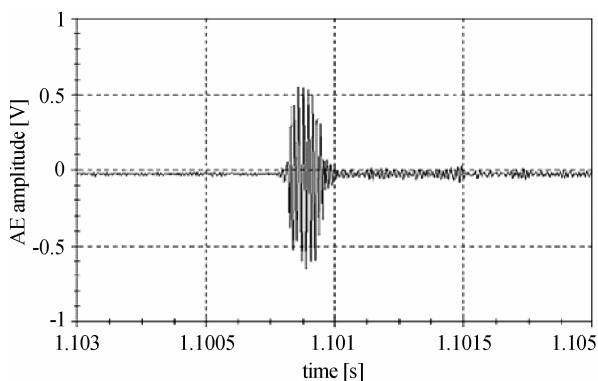
6) The expenses for the AE measurement system are small compared to X-ray systems.

7) The costs per examination including a detailed diagnosis are well below costs of other diagnostic procedures and there is no danger of infection leading to further costs, as happens with invasive methods, e.g. endoscopic examinations.

8) Diagnostic (Real time) monitoring of bone and joint training of sports professionals becomes possible.

The disadvantage of the measurement system suggested was that the physician will be left with the bundle of data and the task to evaluate the AE.

Tatarinov, A., *et al.* [74] proposed multiple acoustic wave method for assessing long bones. The method was based on measurement of ultrasound velocity at different ratio of wavelength to the bone thickness and taking into account both bulk and guided waves. They assessed the changes in both the material properties related to porosity and mineralization as well as the cortical thickness influenced by resorption from inner layers, which are equally important in diagnosis of osteoporosis and osteopenia. More *in vivo* studies on animals and human volunteers has to be carried out before the proposed method could be made clinically usable. The advantage of the method proposed was that it allowed assessment of changes in both the material properties related to porosity and mineralization as well as cortical thickness influenced by resorption from inner layers, which are equally important in diagnosis of osteoporosis and other bone osteopenia. The method could also be used for diagnosis of bone condition if the contribution of soft tissues and topographical heterogeneity in real bones are considered. The method had a potential for better detection of early stage of osteoporosis in long bones. Singh, V. R. [75] reviewed an acoustic imaging technique known as acoustic stress wave propagation technique which was used for bone examination. The technique was developed with the view to solve the problems encountered with the conventional technique like X-rays. As bone is a heterogeneous, complex and fibrous tissue, determination of very small abnormalities viz. shape and size of bone defects, is not usually possible by means of conventional X-ray technique.

In 2006, Azra Alizad, *et al.* [76] studied the change in resonant frequencies of a bone due to change in its physical properties caused due to a fracture. Experiments were conducted on excised rat femurs and resonance frequencies of intact, fractured, and bonded (simulating healed) bones were measured. These experiments demonstrated that changes in the resonance frequency indicated bone fracture and healing. The fractured bone exhibits a lower resonance frequency than the intact bone, and the resonance frequency of the bonded bone approaches that of the intact bone. The graphs are indicative of the result **(Figures 8,9)** [76], that the frequency re-

Figure 7. Acoustic emission from healthy knee joint cartilage deformation after the sudden change from a two leg stand to a one leg stand (source: 73).

sponse of a cut femur is less than the intact femur. The proposed method may be used as a remote and non invasive tool for monitoring bone fracture and healing process, and the use of focused ultrasound enables one to selectively evaluate individual bones. The proposed method offers several advantages over vibrational methods using external mechanical excitation. The ultrasound can be applied remotely and directly to the bone under test, thus avoiding interference of overlaying muscle or other tissues on force distribution. Furthermore, in contrast to traditional methods in which it is difficult to target small bones and to access them, the proposed method allows application of excitation force directly and selectively to the intended bone. The acoustic method for measuring
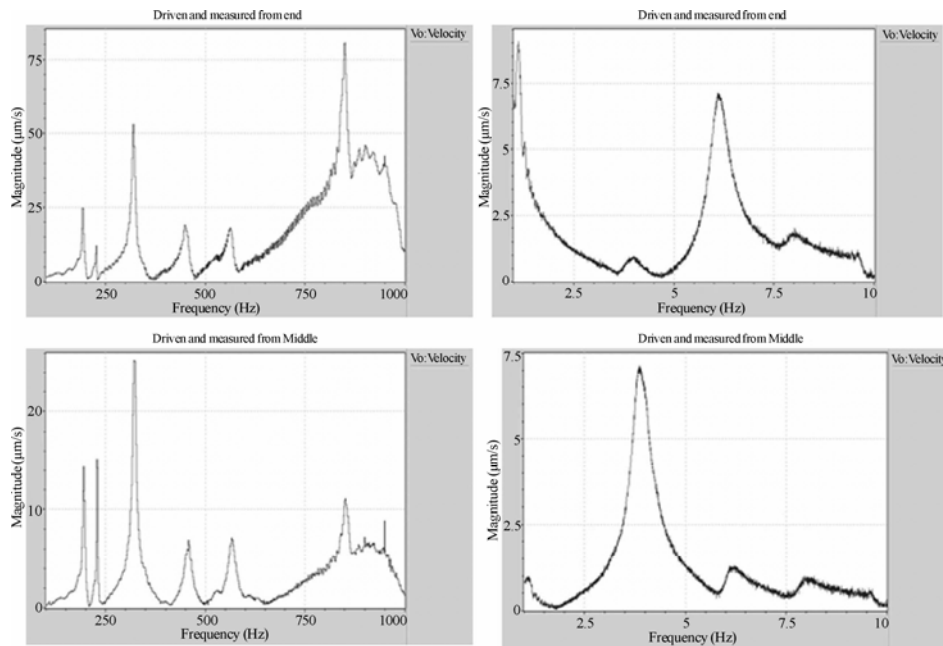
Figure 8. Frequency response of the intact femur A. The plots show the motion of the intact femur vs frequency. These Fig plots indicate peaks at 925 Hz, 4.2 kHz, and 8.1 kHz. Peaks of motion below 700 Hz were explored and found not to be related to the femur. Top left: Driven and measured at the end of the femur at frequency range of 100 Hz to 1000 Hz. Top right: Driven and measured at the end of the bone at 1 kHz–10 kHz. Bottom left: Driven and measured at bone midpoint at 100 Hz–1000 Hz. Bottom right: Driven and measured at bone midpoint at 1 kHz–10 kHz (source: 76).
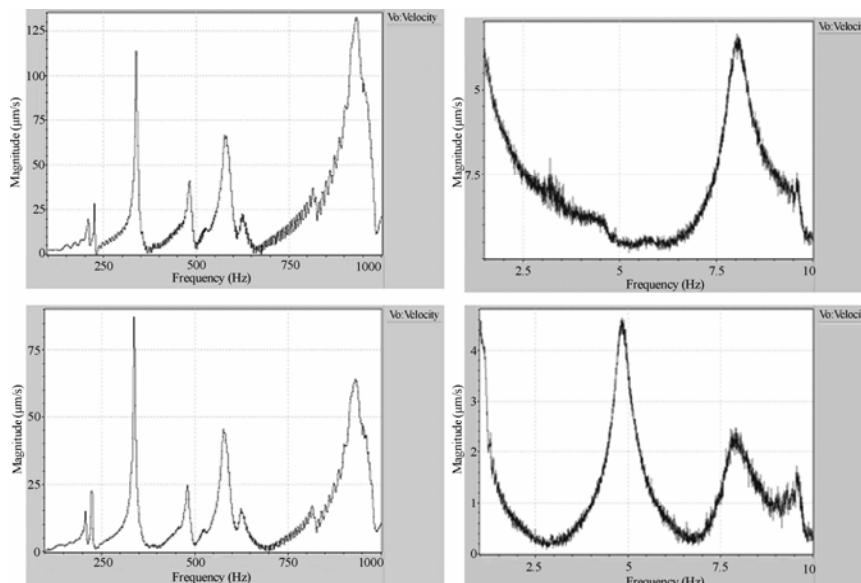

Figure 9. Frequency response of the cut femur (source: 76).

bone response is suitable for *in vivo* applications as long as one take the frequency response of the surrounding structures in to account. An advantage of acoustic motion detection method is that it does not require a direct path to the bone because the acoustic emission produced by the bone travels easily in every direction, thus the location of hydrophone is not critical. Further investigations are needed to demonstrate the applicability of the proposed method for evaluation of bone quality in human body. The boundary conditions of bone to body must also be considered before applying the proposed method.

In 2008, Dipan Bose, *et al.* [77] studied the effect of valgus bending and shear loading on knee joint. They used acoustic sensors to determine the failure timing of soft tissues attached to femur and tibia. The failure timing was determined based on the knee injury mechanism due to valgus loading. At the estimated time injury, the corresponding values of α_{valgus_fail}, d_{shear_fail}, M_{valgus_fail}, and V_{shear_fail} were designated as the failure parameters of the knee. Numerical methods with accurate geometric and material properties could be implemented to simulate and further extend the injury threshold to alternate loading detection. Elmar K. Tschegg, *et al.* [78] did stiffness analysis of tibia implant system under cyclic loading. He used a bio- mechanical system integrated with acoustic emission sensors at the screw head. 3 sequences of loading were used to determine when the locking screws break. Data was obtained from the acoustic sensors onto a data acquisition board and were processed using a acoustic emission software. This acquired data was used to determine as to which screw is bearing the load and as to when does the screw break.

5. CONCLUSIONS

- Many investigations carried out in the field "Assessment of bone condition" are mainly in vitro studies. For any method which is going to be used in clinical practice, a thorough experimental study with animals and/or a clinical study with human volunteers are very much essential.
- The AE is very much dependent on the strain rate.
- AE technique is highly sensitive to specimen damage and cracks and detects them even before visual detection.
- Diagonostic (Real time) monitoring of Bone is possible.
- It is non-destructive and helps us to predict the time length of the healing process.
- It has no harmful effects unlike X-rays, which have radiation effects on patients.
- The emissions from the callus during fracture healing, gives its possibility to be clinically used.

6. FUTURE RESEARCH DIRECTIONS

- Many researchers have used this technique for in vitro as well as in vivo characterization of bone. However, the clinical application of the technique was not fully investigated. The time of occurrence of initial AE and the AE response of bone under different loading conditions at different strain rates are not well established. So focus can be on finding the exact time of occurrence of initial AE with respect to the stress/strain curve and the AE behavior under a suitable loading condition at different strain rates.
- In the case of in vivo studies, the AE response of callus is not thoroughly investigated. Also it is necessary to conduct an experimental study with laboratory animals/volunteers or patients to prove the clinical usage of AE.

7. ACKNOWLEDGEMENT

REFERENCES

[1] F. G. Evans, (1982) Bones and bones, Trans. of ASME, J. Biomechanical Engg., **104/1**, 1−5.

[2] W. C. Hayes, (1978) Biomechanical measurements of bone, in CRC Handbook on Engg., in Medicine and Biology, Section B. Instruments and Measurements, B. N. Feinberg and D. G. Fleming (eds.) CRC Press, Florida, **1**, 333−372.

[3] C. J. Singer, (1959) A short history of scientific ideas to 1900, Oxford University Press, New York.

[4] J. M. Bourgery, (1832) Traite Complet de l' Anatomie de l' Homme. I. Osteologie, Paris.

[5] F. O. Ward, (1838) Outlines of human osteology, London, 370.

[6] G. H. Meyer, (1867.) Die Architektur der spongiosa, Arch. Anat. Physiol. Wiss. Med., **34**, 615−628.

[7] K. K. Hulsen, (1896) Specific gravity, resilience and strength of bone, bull, Biol. Lab. St. Petersburg, **1**, 7−35.

[8] F. G. Evans, (1973) Mechanical properties of bone, Springfield, I. L.

[9] C. O. Carothers, F. C. Smith, and P. Calabrisi, (1949) The elasticity and strength of some long bones of the human body, Nav. Med. Res. Inst. Rept. NM 001056.02.13.

[10] F. G. Evans and M. Lebow, (1951) Regional differences in some of the physical properties of the human femur, J. Appl. Physiol., **3**, 563−572.

[11] F. G. Evans and M. Lebow, (1952) The strength of human bone as revealed by engineering techniques, Am. J. Surg., **83**, 326.

[12] F. G. Evans, (1964) Significant differences in the tensile strength of adult human compact bone, in Proceedings of the First European Bone and Tooth Symposium, H. J. J. Blackwood (ed.), Pergamon, Oxford, 319−381.

[13] E. D. Sedlin and C. Hirsch, (1966) Factors affecting the determination of the physical properties of femoral cortical bone, Acta. Othop. Scand., **37**, 29−48.

[14] E. D. Sedlin, (1965) A rheological model for cortical bone, Acta. Othop. Scand., **33**, 5−77.

[15] A. H. Burstein, J. D. Currey, V. H. Frankel, and D. T. Reilly, (1972) The ultimate properties of bone tissue: The effects of yielding, J. Biomechanics, **5**, 35–44.

[16] A. H. Burstein and V. H. Frankel, (1968) The viscoelastic properties of some biological materials, Ann. N. Y. Acad. Sci., **46**, 158–165.

[17] A. H. Burstein, V. H. Frankel, and D. T. Reilly, (1973) Failure characteristics of bone tissue, in Perspectives in Biomedical Engg, R. M. Kenedi, (ed.), University Park Press, London, 131–134.

[18] A. H. Burstein, D. T. Reilly, and M. Marten, (1975) Aging of bone tissue: Mechanical properties, J. Bone J. Surg, **58**, 82–86.

[19] J. H. Mc Elhaney, (1966) Dynamic response of bone and muscle tissue, J. Appl. Physiol., **21**, pp. 1231–1236.

[20] M. M. Panjabi, A. A. White, and W. O. Southwick, (1973) Mechanical properties of bone as a function of rate of deformation, J. Bone. J. Surg, **55(A)**, 322–330.

[21] R. D. Crowinshield and M. H. Pope, (1974) The response of compact bone in tension at various strain rates, Ann. Biomed.Engg., **2**, 217–225.

[22] T. M. Wright and W. C. Hayes, (1976) Tensile testing of bone over a wide range of strain rates: effects of strain rate, Microstructure and Density, Med. Biol. Engg., **14**, 671–680.

[23] S. B. Lang, (1970) Ultrasonic method for measuring elastic coefficients of bone and results on fresh and dried bovine bones, IEEE Trans. Biomed. Engg., **17**, 101–105.

[24] H. S. Yoon and J. L. Katz, (1976) Ultrasonic wave propagation in human cortical bone: I, Theoretical Considerations for Hexagonal Symmetry, J. Biomechanics, **9**, 407–412.

[25] H. S. Yoon and J. L. Katz, (1976) Ultrasonic wave propagation in human cortical bone: II, Measurements of Elastic Properties and Micro hardness, J. Biomechanics, **9**, 459–464.

[26] R. B. Ashman, J. D. Corin, and C. H. Turner, (1987) Elastic properties of cancellous bone: measurement by an ultrasonic technique, J. Biomech, **20(10)**, 979–986.

[27] E. Lachmann and M. Whelan, (1936) The roentgen diagnosis of osteoporosis and its limitations, Radiology, **26**, 165–177.

[28] E. Lachmann, (1955) Osteoporosis: The potentialities and limitations of its roentgenologic diagnosis, Amer. J. Roentgenology, **74**, 712–715,

[29] I. I. H. Chen and S. Saha, (1987) Wave propagation characteristics in long bones to diagnose osteoporosis, J. Biomech., **20(5)**, 523–527.

[30] F. Y. Wong, S. Pal, and S. Saha, (1983) The assessment of in vivo bone condition in humans by impact response measurement, J. Biomech., **16(10)**, 849–856.

[31] L. L. Stern and J. Yageya, (1980) Bioelectric potentials after fracture of tibia in rats, Acta Orthop. Scand., **51**, 601–608.

[32] S. Saha and R. R. Pelker, (1976) Measurement of fracture healing by the use of stress waves, 22nd Annual ORS, New Orleans, Louisiana.

[33] D. A. Sonstegard and L. S. Mathews, (1976) Sonic diagnosis of bone fracture healing–A preliminary study, J. Biomech. **9**, 689–694.

[34] N. Guzelsu and S. Saha, (1981) Electromechanical wave propagation in long bones, J. Biomech., **14**, 19–33.

[35] G. T. Anast, M. S. Fields, and Siegel, (1958) .Ultrasonic technique for the evaluation of bone fracture, Amer. J. Physical. Med., **37**, 157–159.

[36] S. Saha, V. V. Rao, V. Malakanok, B. D. Gross, and J. A. Albright, (1982) Ultrasonic evaluation of fracture healing, Transactions of the 28th Annual Meeting of the Orthopedic Research Society, ORS, Chicago, 259.

[37] O. O. A. Oni, A. Graebe, M. Parse, and P. J. Gregg, (1989) Prediction of the healing potential of closed adult tibia shaft fractures by bone scientigraphy, Clinical Orthopedics and Related Research, 239–245.

[38] S. M. Bentzen, I. Hivid, and J. Jorgensen, (1987) Mechanical strength of tibial trabecular bone evaluated by X-ray computed tomography, J. Biomech., **20**, 743–752.

[39] T. Sekiguchi and T. Hirayama, (1979) Assessment of fracture healing by vibration, Acta Orthop.Scand., **50**, 391–398.

[40] R. J. Donarski, (1989) Bone Fracture measurement using mechanical vibration, Ph. D. Thesis, University of Kent at Canterbury, UK.

[41] R. Prakash, (1980) Non destructive testing of composites, Composites, **10**, 217–224.

[42] J. Kaiser, (1950) Untersuchungen uber das auftreten gereausen bein Zugersuch, Ph. D. Thesis, Technische Hutchshule, Munich.

[43] A. A. Pollock, (1979) An introduction to acoustic emission and a practical example, J. Environmental Sciences, March/April, 1–4.

[44] S. Radhakrishnan, (1992) The assessment of bone condition by acoustic emission and acousto-ultrasonic techniques. Ph. D. Thesis, Banaras Hindu University.

[45] S. Hanagud, R. G. Clinton, and J. P. Lopez, (1973) Acoustic emission in bone substance, Proceedings of Biomechanics Symposium of the American Society of Mechanical Engineers, ASME, New York, 74.

[46] I. V. Knet-s, U. E. Krauya, and Y. K. Vilks, (1975) Acoustic emission in human bone tissue upon lengthwise stretching, Mekh. Polim, **4**, 685–690.

[47] U. E. Kruya and Y. A. Lyakh, (1978) Acoustic emission in human bone tissue, Mekh. Polim., **1**, 109–112.

[48] A. Peters, (1982) Acoustic emission technique and fracture healing, Med. Biol. Engng. Comput, **20**, 8.

[49] T. M. Wright and J. M. Carr, (1983) Soft tissue attenuation of acoustic emission pulses, Trans. of ASME J. Biomech. Engg, **105(1)**, 21–23.

[50] S. Hanagud, G. T. Hannon, and R. G. Clinton, (1974) Acoustic emission and diagnosis of osteoporosis, Proceedings of Ultrasonics Sym., 77–80.

[51] R. A. Thomas, H. S. Yoon, and J. L. Katz, (1977) Acoustic emission from fresh bovine femora, Proceedings of Ultrasonics Symp. IEEE Cat.No. TICH12G4-ISU, 237–240.

[52] H. S. Yoon, B. R. Caraco, and J. L. Katz, (1980) Further studies on the acoustic emission of fresh animal bone, IEEE Trans. Sonics, Ultrasonic, SU-27, 160.

[53] P. Netz, (1979) The diaphyseal bone under torgue, Acta Orthop. Scand. Suppl., **176**, 1–31.

[54] T. M. Wright, F. Booburgh, and A. H. Burstein, (1981) Permanent deformation of compact bone monitored by acoustic emission, J. Bomech, **14**, 405–409.

[55] R. A. Fischer, S. W. Arms, M. H. Pope, and D. Seligson, (1986) Analysis of the effect of using two different strain rates on the acoustic emission in bone, J. Biomech., **19(2)**, 119–127.

[56] P. J. Nicholls and E. Berg, (1981) Acoustic emission properties of callus, Med. Biol. Engg. Comput, **19**, 416–418.

[57] S. Hanagud, R. G. Clinton, M. D. Chouinard, E. Berg, and P. J. Nicholls, (1977) Soft tissues and acoustic emission based diagnostic tools, 1977 Ultrasonics Symposium Proceedings, IEEE CAT. No. 77CH1264-ISU, 242–245.

[58] M. Martens, R. van Audekercke, P. de Meester, J. C. Mulier, (1986) Mechanical behaviour of femoral bones in bending loading, Journal of Biomechanics, **19(6)**, 443–454.

[59] K. Ono, (1979) Fundamentals of acoustic emission, Los Angeles (CA), UCLA, 167–207.

[60] K. Stromsoe, A. Hoiseth, A. Alho, and W. L. Kok, (1995) Bending strength of the femur in relation to non-invasive bone mineral assessment, Journal of Biomechanics, **28(7)**, 857–861.

[61] B. C. Lentle, Diagnosis of osteoporosis using acoustic emission, The University of British Columbia, Patent no A61B8/08, 1999.

[62] J. G. Wells, (1985) Acoustic emission and mechanical properties of trabecular bone, Biomaterials, **6**, 218–24.

[63] I. Leguerney, K. Raum, A. Saied, H. Follet, G. Boivin, and P. Laugier, (2003) Evaluation of human trabecular bone properties by scanning acoustic microscopy, J. Bone Min. Res., **18**, S187.

[64] R. M. Rajachar, D. L. Chow, C. E. Curtis, N. A. Weissman, and D. H. Kohn, (1999) Use of acoustic emission to characterize focal and diffuse micro damage in bone, in: Acoustic Emissions: Standards and Technology Update, West Conshohocken, PA: American Society for Testing and Materials, 3–19.

[65] Y. Watanabe, S. Takai, Y. Arai, N. Yoshino, and Y. Hirasawa, (2001) Prediction of mechanical properties of healing fractures using acoustic emission, Journal of Orthopedic Research, **19**, 548–553.

[66] S. C. K. Kevin, H. Xiaolin, C. Y. C. Jack, and H. E. John, (2003) Acoustic transmission in normal human hips: Structural testing of joint symmetry, Medical Engineering & Physics, **25(10)**, 811–816.

[67] S. Bumrerraj and J. L. Katz, (2001) Scanning acoustic microscopy study of human cortical and trabecular bone, Ann. Biomed. Engg, **29(12)**, 1034–1042.

[68] I. Eckardt and H. J. Hein, (2001) Quantitative measurements of the mechanical properties of human bone tissues by scanning acoustic microscopy, Ann. Biomed. Engg., **29(12)**, 1043–1047.

[69] Y. Xia, W. Lin, E. Mittra, B. Demes, B. Gruber, C. Rubin, and Y. Qin, (2003) Performance of a confocal acoustic mapping in characterization of trabecular bone quality in human calcaneus, J. Bone Min. Res, **18**, S209.

[70] L. Cardoso, F. Teboul, L. Sedel, C. Oddou, and A. Meunier, (2003) In vitro acoustic waves propagation inhuman and bovine cancellous bone, J. Bone Min. Res, **18(10)**, 1803–1812.

[71] A. Ozan, (2005) Acoustic emission based surveillance system for prediction of stress fractures, Ph. D. Nicholas Wasserman, The University of Toledo Annual report.

[72] M. Browne, A. Roques, and A. Taylor, The acoustic emission technique in orthopaedics–a review, J. Strain Analysis, **40(1)**.

[73] R. P. Franke, P. Dörner , H.-J. Schwalbe, and B. Ziegler, (2004) Acoustic emission measurement system for the orthopedical diagnostics of the human femur and knee joint, University of Ulm, Dept. of Biomaterials, Ulm, Germany, Bad Griessbach, Germany, University of Applied Science Giessen, Giessen, Germany.

[74] A. Tatarinov, S. Noune, and S. Armen, (2005) Use of multiple acoustic wave modes for assessment of long bones: Model study, Journal of Ultrasonics, **43**, 672–680.

[75] V. R. Singh, (1989) Acoustical imaging techniques for bone studies, Applied Acoustics, **27**, 119–128.

[76] A. Alizad, M. Walch, J. F. Greenleaf, and M. Fatemi (2006) Vibrational characteristics of bone fracture and fracture repair: application to excised rat femur, Journal of Bio Medical Engineering, Trans ASME, **128**.

[77] D. Bose, K. Bhalla, C. D. Untaroju, B. J. Ivarsson, and J. R. Crandall, (2008) Injury tolerance and moment response of knee joint to combined valgus brnding and shear loading, Journal of BioMedical Engineering, **130**.

[78] E. K. Tschegg, S. Herndler, P. Weninger, M. Jamek, S. Stanzl- Tschegg, H. Redl, (2008) Stiffness analysis of tibia implant system cylical loading, Material Science and Engineering C, **28**, 1203–1208.

Research on the ultraweak photon emission from anti-cancer plants

Ping Wu[1], Xiang He[1]

[1]Dept. of Applied Physics, Nanjing University of Aeronautics and Astronautics, Nanjing, 210016, China.
Email: pwu2000@nuaa.edu.cn

ABSTRACT

UPE (Ultraweak photon emission) is one kind of a common phenomenon in biological organisms. It contains a wealth of information of biological functions. In this paper, single photon counting system is used to measure UPE of some anti-cancer herbal plants. For the plants, the changes of UPE under different water condition are studied and the varying laws of ultraweak photon number with time are analysed. The results are higher fit double exponential decay law.

1. INTRODUCTION

In 1920's, A. G. Gurwitsch, a former Soviet Union's cell biologist, was the first to discover the phenomena of the ultraweak photon emission from biological object (UPE) during the period of the cell division of onion root tip [1]. UPE was able to be carried on the research until 1950's because of the restrictions of the experimental means. In 1951, B. L. Strehler, *et al.* [2] observed the photon emission from green plants induced by light, and this phenomenon is called "delayed luminescence." In 1955, the L. Coli group used the high sensitivity photomultiplier, which just came out, to detect the photon emission from the wheat, legumes and corn at the germination process [3]. From 1960's to1970's, the former Soviet Union scientists have researched except on plant but also on animal tissue like frog's nerve and muscle, mouse's liver and so on. They discovered that UPE is different from ordinary bioluminescence, for example fluorescence and so on, but is correlative with biological metabolism.

So far, many experimental results show that the presence of UPE in biological organisms including plants, animals, etc. UPE is an intrinsic and spontaneous process of biological organisms and is different from bioluminescence phenomena observed, for example, in fireflies or luminescent bacteria. UPE is not dependent on any particular enzyme or protein. It is the reflection of the general information of the biological function and has inherence relations with the life processes such as cellular metabolism, cell division, growth, death, mutation and cell-to-cell transmission of information. So, the ultraweak photons can transmit the information of biological objects and it is playing an increasingly important role in the development of biological science.

About UPE mechanism now there is no conclusion. There are two major kinds of explain separately in chemistry and in physics. In chemistry, the main explanation is "the mechanism of metabolize emission", which thinks that the oxidation of the unsaturated fatty acid produce peroxide free radical. The peroxide in excited state can be form when peroxide free radical compound, and then UPE will be generated when the peroxide withdraw from excited state [4]. In physics, F. A. Popp, *et al.* put forward "the mechanism of coherent emission" [5,6]. They think that UPE partly or wholly originate from the highly coherent electromagnetic field in biological system and the field is possibly the basis of communication between living tissues. The F. A. Popp's research on the organisms of the light-induced delayed luminescence indicate that the luminescence accord with the law of hyperbolic attenuation. This is precisely the important characteristic of coherent field [7]. But "the mechanism of metabolize emission" and "the mechanism of coherent emission" only can partially explain some experimental results for UPE. This reflects the complexity of UPE mechanism, as well as the limitation which the people knew to it.

At present, the research on UPE also exist a lot of important questions to be resolved, such as the mechanism of producing UPE, the detection technology of ultraweak photon and the interpretation information of UPE and so on. In this paper, we detect the UPE from some kind of anti-cancer plants by using photon count-

ing system, and analyze the time varying law of biological photon counting.

2. EXPERIMENT SYSTEM AND MATERIAL

2.1. Experiment System

The output current signal of the photomultiplier tube is characteristic of the natural discretization under the weak light illumination. The single photon counting system makes use of the characteristic and adopt the technique of pulse height screening and digital counting, so it has high sensitivity. It can detect the very weak photon information whose intensity of the optical flow lower than the thermal noise level (10-14W) of photomultiplier under room temperature, and it can be used for the measure of UPE. The structure of the experiment system is shown in **Figure 1**. In measurement, the sampling interval is 3 minutes, the integral time is 1 minute.

2.2. Experimental Material

The leaves of anti-cancer plant including Barbed Skullcap Herb, Pedate Pinallia Jackinthepulpit Rhizome and Cochinchnese Asparagus Root are chosen as the measured samples. The UPE of the samples at different growth status have be measured by the single photon counting system and the correlation curves of the biological photon counting with time are described.

3. MEASUREMENT RESULTS AND DISCUSSION

3.1. Measurement Results for Different Situations

The UPE of the leaves for three plants in the normal implantation situation and the situation of stopping watering a few days are measured separately and the differences of UPE under different conditions are evident. The measuring curves and fitting curves for the photon counting of the samples with time are shown in **Figure 2**–**Figure 4**.
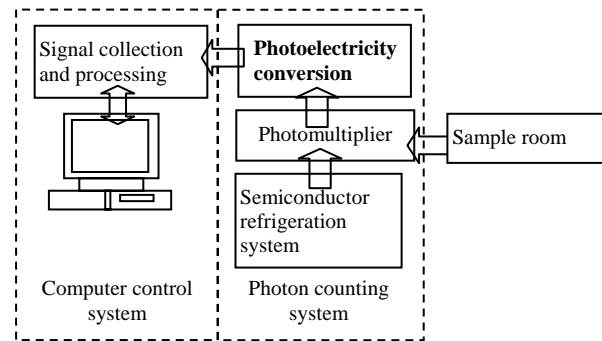
Figure 1. Structure of experiment system.
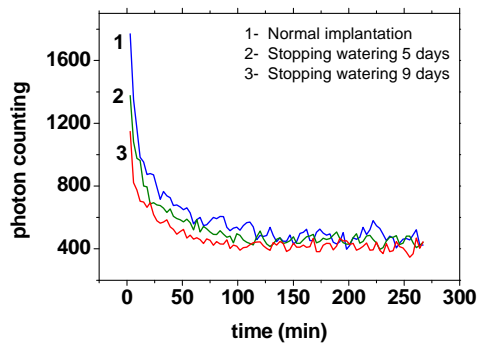
(a) Measuring curves of UPE
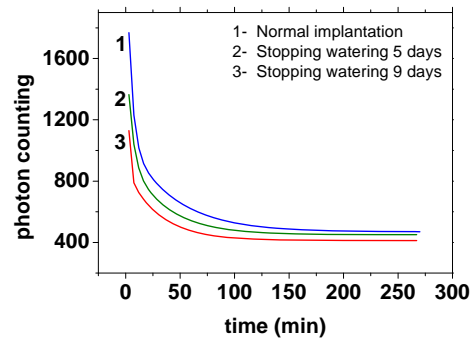
(b) Fitting curves with double exponential decay

Figure 2. Measuring curves and fitting curves of Barbed Skullcap Herb.
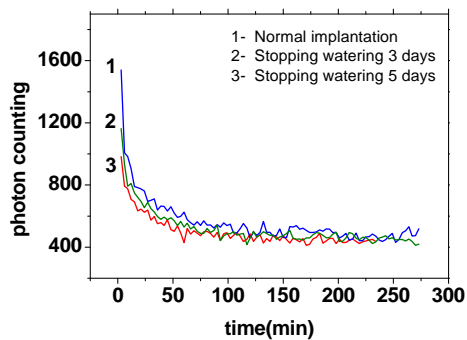
(a) Measuring curves of UPE
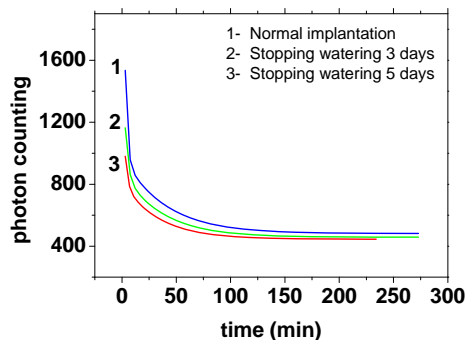
(b) Fitting curves with double exponential decay

Figure 3. Measuring curves and fitting curves of Pedate Pinallia Jackinthepulpit Rhizome.

(a) Measuring curves of UPE

(b) Fitting curves with double exponential decay
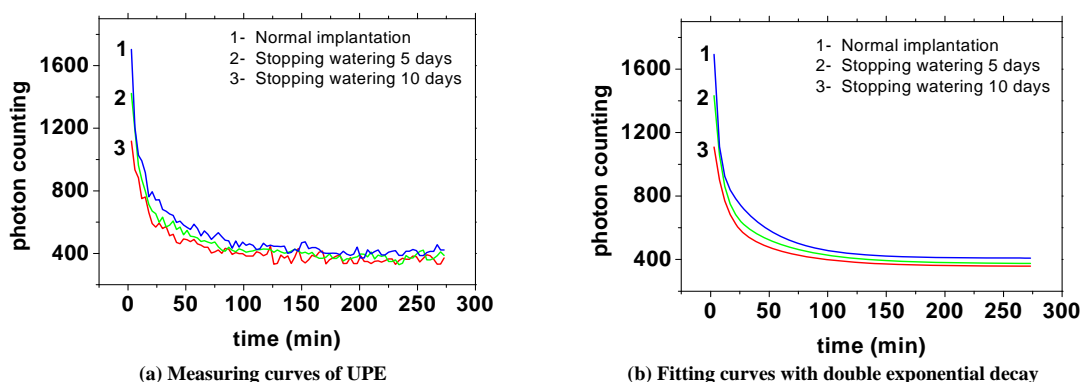
Figure 4. Measuring curves and fitting curves of Cochinchnese Asparagus Root.

Table 1. Fitting results of Barbed Skullcap Herb.

	Double expo-nential decay	Exponential decay	Gaussian function
Normal implantation	0.97083	0.9187	0.90616
Stopping watering 5 days	0.96989	0.94243	0.93253
Stopping watering 9 days	0.95414	0.91233	0.90341

Table 2. Fitting results of Pedate Pinallia Jackinthepulpit Rhizome.

	Double expo-nential decay	Exponential decay	Gaussian function
Normal implantation	0.96815	0.88676	0.87291
Stopping watering 3 days	0.96843	0.92953	0.93457
Stopping watering 5 days	0.95613	0.93143	0.91942

Table 3. Fitting results of Cochinchnese Asparagus Root.

	Double expo-nential decay	Exponential decay	Gaussian function
Normal implantation	0.9875	0.94895	0.9394
Stopping watering 5 days	0.98748	0.94675	0.9352
Stopping watering 10 days	0.97057	0.93394	0.922

From the measurement results, it is clear that the intensity of UPE from the samples display a marked decline under the lacking water condition, and the intensity will further reduce along with the increase in the number of lacking water days. This reflects the growth of plants for water-dependent, in the lacking water condition, the plants appeared the decline of the internal functions.

Comparing of the fitting curves under the lack of water in five days, it may be seen that the reduction of UPE from Barbed Skullcap Herb slower than Pedate Pinallia Jackinthepulpit Rhizome and Cochinchnese Asparagus Root. This is related to their own growth habit. Barbed Skullcap Herb has a certain water-retention capacity, and its branches or leaves, which have been picked off and exposed to the sun, can be survived after inserted into moist soil. Pedate Pinallia Jackinthepulpit Rhizome and Cochinchnese Asparagus Root are all delighted for moist, so the lack of water is of more influences on them.

3.2. Emission Laws Discussion

In order to study the law of UPE from the samples, the measured curves are respectively fitted with double exponential decay, exponential decay and Gaussian function. The results of three different fitting are shown in **Tables 1−3.**

It is not difficult to see from the results in **Tables 1−3**, the fitting of double exponential decay is the best of the three, and it is different from the coherent theory that thinks UPE accord with hyperbolic attenuation. So it reflects that UPE is a very complex biological system, not fully coherent mechanism but a variety of mechanisms have a role in it. There have been some research results shown that the dual-exponential decay law [8], but is still very difficult to explain theoretically. One view is that this is because there are a number of the coherent system in biology and there are interaction between them. In order to reveal the nature of UPE, it is required that a large amount of experimental and theoretical work to be done.

REFERENCES

[1] A. G. Gurwitsch, (1923) Arch Entw Mech Org, **100 (1)**, 11−40.

[2] B. L. Strehler and W. Arnold, (1951) J Gen Physiol, **34,** 809−820.

[3] L. Colli, U. Facchini, and G. Guidotti, (1955) Further measurements on the bioluminescence of the seedlings, Experientia, **11,** 479−481.

[4] X. Gang, (1994) The ultrawesk photon emission in plant and its application in agriculture, Physics, **9,** 548−552.

[5] F. A. Popp, K. H. Li, W. P. Mei, *et al.*, (1988) Physical aspects of biophotons. Experientia, **44**, 576−585.

[6] F. A. Popp, (1988) Biophoton emission, Experientia, **44**, 543−544.

[7] F. A. Popp, Q. Gu, and K. H. Li, (1994) Biophoton emission:Experimental background and theoretical approaches, Modern Physics Letters B, **8 (21&22)**, 1272−1274.

[8] J. L. Chen and Z. G. Lu, (1999) Garlic Delayed Luminescence, Journal of Optoelectronics and Laser, **10**, 365−367.

A muscle spindle model and study the effects of static and dynamic γ stimulations on primary and secondary ending outputs

Glayol Nazari Golpayegani[1], Amir Homayoun Jafari[1]

[1]Biomedical Engineering Department Islamic Azad University, Science and Research Branch Tehran, Iran
Email: Gelayol777@yahoo.com, Amir_j73@yahoo.com

ABSTRACT

A linear lumped-parameter mechanical model of the muscle spindle is presented. It is shown that the model simulation exhibits the spindle behavior in most aspects of transient ramp-stretch performance. The requirements that such a model places on the mechanisms of fusimotor control are discussed. Then the efficacy of static γ and dynamic γ stimulation on primary ending output and secondary ending output is studied. The results of simulations show that primary ending of muscle spindle is affected either by static and dynamic stimulation and Secondary ending of muscle spindle is affected only by static fiber stimulation. The bias of primary ending output is increased by an increase in static γ stimulation. The Ramp of primary ending response is increased by an increase in dynamic γ stimulation. An increase in static γ stimulation in secondary ending of muscle spindle increases the dc level of secondary ending output so the bias of output is increased too.

Keywords: Modeling; Muscle Spindle; Postural Control Systems

1. INTRODUCTION

The mammalian muscle spindle, as recent anatomical studies have shown [1,2,3,4,5], is a highly complex sensory organ connected in parallel with skeletal muscles for detecting change and rate of change in length in those muscles. Each spindle consists of several "interfusal" fibers (as distinct from "extrafusal" fibers of which the bulk of skeletal muscle consists) which appear to fall into two groups, with respect to their anatomical and their physiological characteristics. A simple example is illustrated in **Figure 1**. The larger type of fiber consists of striated contractile tissue with a non contractile equatorial region which possesses nuclei but lacks myofilaments. The distribution of nuclei within the equatorial region has led to naming this type the "nuclear-bag fiber." The smaller fibers have striations and nuclei throughout their entire length and are called "nuclear-chain fibers."

The efferent innervation to the fibers is by way of the gamma-motor (γ-motor) or fusimotor system. It is agreed that there are two anatomically distinct kinds of fusimotor innervation, distinguishable by the nature of the nerve endings. There are "γ-plate" fibers, ending in small end plates similar to those at extrafusal myoneural junctions and "γ-trail" fibers whose endings are more diffuse. (There is actually a third kind of innervation, the β-plate ending, which we will not discuss here). It is not agreed as to whether both types of endings are found on both bag and chain fibers, as Barker [1] holds. According to Boyd [2], plates are only found on bag fibers and trail only on chain fibers.

Activation of skeletal muscle has definite influence in increasing the stiffness and viscosity of the muscle [7]. In all likelihood, this happens to intrafusal muscles too, although it has not been verified experimentally. Such changes in parameter value would modify spindle response to stretch.

The amount of force produced by intrafusal contraction is known only roughly by measurement [8,9] or computation [10,11], and those measurements are of whole spindles without differentiation between bag or chain fiber contraction. Boyd has stated [12,13] that contraction is more pronounced and faster in chain fibers than in bag fibers but much remains to be learned about this aspect of spindle behavior. The very tentative conclusion that has been proposed [14] is that dynamic stimulation controls output mainly through modification of parameter values by trail endings, while static stimulation works through force generated in the chain fibers through the plate endings.

The afferent innervation from the spindles is also of two types. The primary afferent has its endings both on the nuclear bag and on the nuclear chain. The secondary

afferent usually has endings only on the nuclear chain. When the muscle is stretched or the y-motor nerves stimulated, action potentials are recorded in the primary and secondary afferent nerves. Corresponding to the anatomical observations described above, there is an equally bimodal response with respect to both stretch and stimulation as recorded from the two types of nerves.

The purpose of this paper is to describe some simulations of a linear lumped-parameter mechanical model of the muscle spindle as a neurally controlled transducer of stretch and discuss the requirements such a model places on the mechanisms of control. To do this, we shall first summarize the various types of responses to the various types of inputs that have been described by numerous previous investigators [15,16,17,18].

In order to clarify our terminology yet remain reasonably consistent with the physiological literature, let us define three terms: dynamic sensitivity, static sensitivity, and bias. These refer to steady-state behavior after transients have died out. The dynamic sensitivity is a measure of that component of the spindle afferent output which is proportional to the rate of spindle stretch. It has units of pps/mm/s. The static sensitivity is a measure of that component of the spindle afferent output which is proportional to the amplitude of spindle stretch. It has units of pps/mm. The bias is the tonic component of the spindle output that is independent of stretch. It has units of pps. Note that the bias corresponds to they intercept on the length-firing rate curve and, as such, it is sensitive to changes in the slope of that curve. Thus changes in the static sensitivity may be reflected, in part, by proportional changes in bias.

The γ-motor system can be divided into two groups, dynamic and static fusimotor fibers, on the basis of their differential effects on the primary and secondary afferents. These effects are summarized in Table I. The primary afferent is influenced by stimulation of both dynamic an static fibers, the former having their most pronounced effect on the dynamic sensitivity and the latter enhancing the bias and static sensitivity. The secondary afferent is influenced almost solely by the static fusimotor fibers.

This paper is organized as following sections: we describe our model in Section 2. We show our simulation results in Section 3. In Section 4 we study the effects of static γ and dynamic γ stimulation on primary ending output and secondary ending output and we have discussion in last section.

2. MODEL

The model we have chosen for our simulation is shown in **Figure 2**. It is an extremely general viscoelastic system for which we wish to establish, not merely a transfer function of the spindle, but an anatomical-topological equivalence such that displacements of the model nodes give a direct quantitative measure of deformations of the spindle's sensory regions.

The upper half of **Figure 2** is the nuclear-bag fiber which consists of a lumped tendon and series elasticity, two identical contractile sections representing the larger intrafusal muscle fibers, and a non contractile nuclear bag from which part of the primary output is taken. The nuclear chain fiber is the lower half of the figure is at-
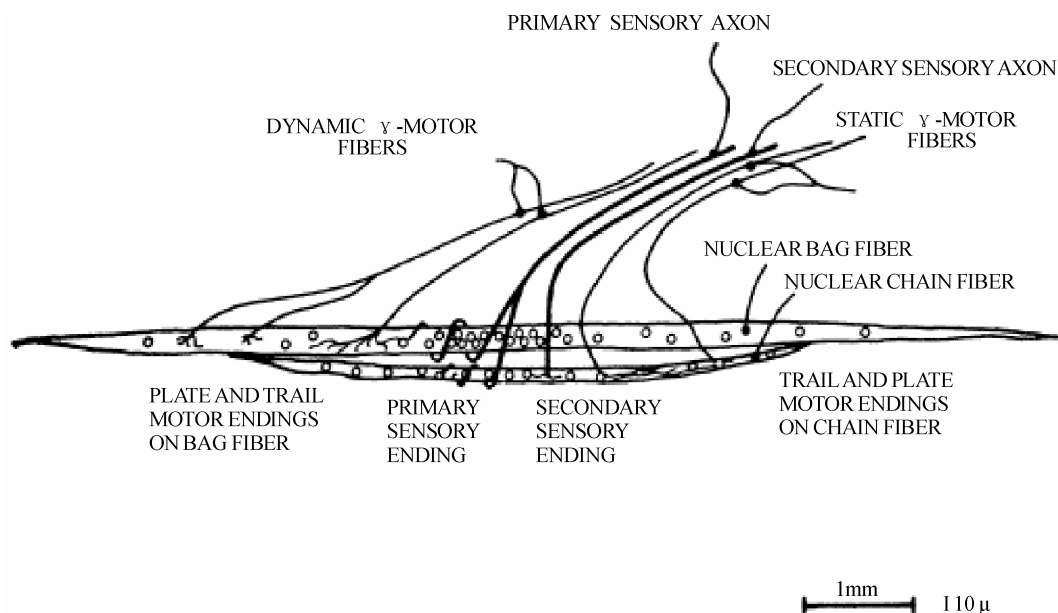

Figure 1. Simple two-fiber mammalian muscle spindle with two types of fibers and efferent and afferent innervation.
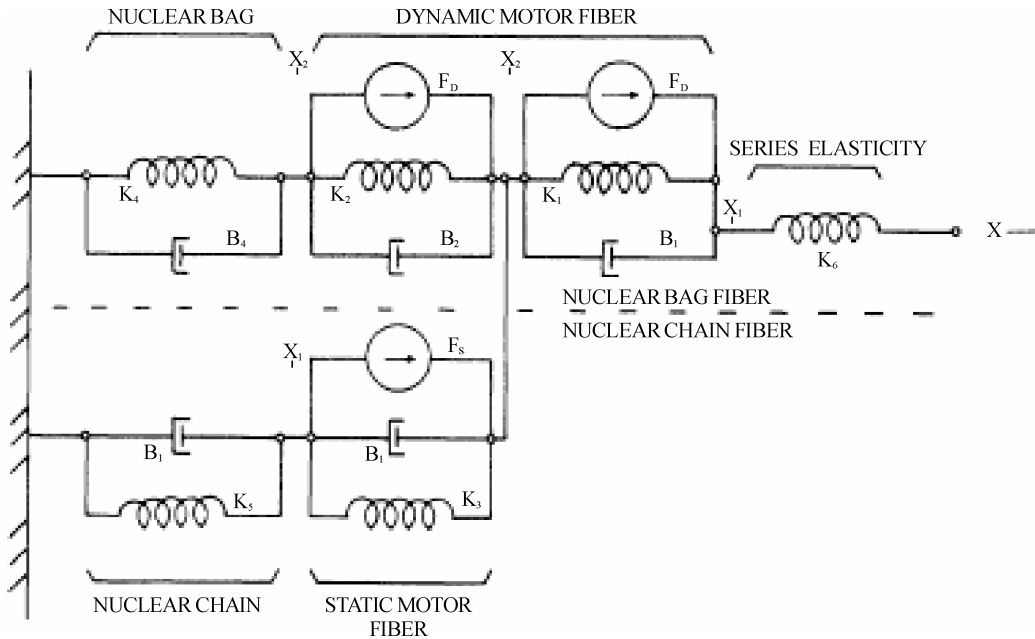
Figure 2. Mechanical model of simple mammalian muscle spindle.

tached to the bag fiber at the mid point between the two contractile sections. It has its own independent con-tractile section and a non contractile sensory segment. This segment provides the other portion of the primary output and all of the secondary output.

Before discussion of our simulations on this system, it would be of value to consider, in qualitative terms, the properties of the system that are important in duplicating spindle behavior. As was pointed out by Crowe and Matthews [18] and demonstrated in previous simulations [11,19], the velocity sensitivity of the bag fiber can be accounted for by assuming that it is considerably stiffer elastically than the contractile tissue. The chain fiber, on the other hand, appears fairly uniform in composition. In terms of the model, it is convenient to talk in terms of a time constant. This time constant is defined by **Eq.1**:

$$T_i = B_i / K_i \qquad (1)$$

The model response to stretch would be appropriate if the time constant of the bag T4 were to be much smaller than that of the muscular segments T1 and T2 while the two chain time constants T3 and T5 were to be of equivalent magnitudes to each other.

When stimulation is introduced, the three measures of spindle response discussed previously, namely, bias, static sensitivity, and dynamic sensitivity, are useful to systematize the discussion. Only the contractile segments are assumed controllable with respect to force output and parameter changes.

The system may be represented by linear differential equations as

$$K_6(x - x_1) = K_1(x_1 - x_2) + B_1(\dot{x}_1 + \dot{x}_2) + F_D \qquad (2)$$

$$K_6(x - x_1) = K_2(x_2 - x_3) + K_3(x_2 - x_4) + B_2(\dot{x}_2 + \dot{x}_3) \\ + B_3(\dot{x}_2 - \dot{x}_4) + F_D + F_S$$

$$(3)$$

$$K_2(x_2 - x_3) + B_2(\dot{x}_2 - \dot{x}_3) + F_D = K_4 x_3 + B_4 \dot{x}_3 \qquad (4)$$

$$K_3(x_2 - x_4) + B_3(\dot{x}_2 - \dot{x}_4) + F_S = K_5 x_4 + B_5 \dot{x}_4 \qquad (5)$$

A set of nonlinear equations in which the elasticities and viscosities are dependent on length and/or velocity were deliberately not used because, as we shall show, almost all the qualitative features of spindle response can be simulated without the vast increase in computational complexity required for such a nonlinear model. An important complicating feature we do require however, is that the intrafusal muscular components K1, K2, K3 and Bi, B2, B3 vary with the level of γ control. In order to avoid the need for time varying parameters, we restricted the inputs in a manner that when stretch and fusimotor inputs were both applied their respective transient responses did not overlap in time. In this manner, stretch would be applied only after the parameters had reached appropriate equilibrium levels for the degree of fusimotor stimulation. Since all the experimental data we found in the literature has been gathered under these same conditions this limitation is not severe at present.

Under the above constraints, we can take the Laplace transform of (2) and then rewrite them as in (3) for analog simulation:

$$x_1 = a_1 \frac{x_1}{s} + a_2 \frac{x_2}{s} + a_3 \frac{x}{s} + a_4 \frac{F_D}{s} + x_2 \qquad (6)$$

$$x_2 = b_1 \frac{x_1}{s} + b_2 \frac{x_2}{s} + b_3 \frac{x_3}{s} + b_4 \frac{x_4}{s} + b_5 \frac{x}{s} + b_6 \frac{F_D}{s}$$
$$+ b_7 \frac{Fs}{s} + b_8 x_3 + b_9 x_4 \qquad (7)$$

$$x_3 = c_1 \frac{x_2}{s} + c_2 \frac{x_3}{s} + c_3 \frac{F_D}{s} + c_4 x_2 \qquad (8)$$

$$x_4 = d_1 \frac{x_2}{s} + d_2 \frac{x_4}{s} + d_3 \frac{Fs}{s} + d_4 x_2 \qquad (9)$$

We chose to rewrite (7) by combining it with (8) and (9) and get (10) (equations for *ai, bi, ci, di,* and *ei* in terms of the model parameters are listed in Appendix I):

$$x_2 = e_1 \frac{x_1}{s} + e_2 \frac{x_2}{s} + e_3 \frac{x_3}{s} + e_4 \frac{x_4}{s}$$
$$+ e_5 \frac{x}{s} + e_6 \frac{F_D}{s} + e_7 \frac{F_S}{s} \qquad (10)$$

The block simulation of these four **Eqs.6, 8, 9, and 10** is shown in **Figure 3**. The output of **Figure 3(c)** is nuclear bag stretch and output of **3(d)** is nuclear chain stretch. The primary output is given by **Eq.11** and the secondary output by **Eq.12**:

$$f_1 = \alpha x_3 + \beta x_4 \qquad (11)$$

$$f_2 = \delta x_4 \qquad (12)$$

3. RESULTS OF SIMULATIONS

Figure 4 shows some results of our simulations for pri-

mary and secondary outputs. The parameters used in the simulation are listed in Appendix II.

In **Figure 4(a)** the primary output in response to stretch and γ stimulation is shown. In the lower curve, the spindle is relaxed and unstretched for 0.5 second and then stretched 3 mm at 6 mm/s. The middle curve shows the effects of adding static γ-motor stimulation of 100 pps starting at t=0 while the upper curve shows the effects of dynamic γ-motor stimulation of 100 pps. Quite clearly, dynamic stimulation effects dynamic and static sensitivity as well as bias by stretching the nuclear bag and by increasing the viscosity of the bag fiber's contractile components. The effects of static stimulation are simply increased bias and static sensitivity from the chain branches of the ending. **Figure 4(b)** shows the output of the secondary afferent for the same inputs. The absence of dynamic sensitivity and the ineffectiveness of dynamic stimulation are apparent. These curves show that our model does mimic spindle behavior in most aspects of transient ramp-stretch performance as listed in **Table 1**.

4. STUDY THE EFFECTS OF STATIC AND DYNAMIC GAMMA STIMULATION ON PRIMARY AND SECONDARY ENDING OUTPUTS

After we simulated our model, we studied the effects of static and dynamic γ stimulation on primary and secondary ending outputs.

4.1. Effects of Static and Dynamic γ Stimulation on Primary Ending Output

As we can see from **Figure 4(a)**, with applying the dynamic γ stimulation on primary ending, we have following results: 1) the ramp of primary ending response is increased, 2) the dc level is increased and 3) final with


Figure 3. Analog computer simulation of model of Figure 2.

unstimulated situation. With applying static γ stimulation on primary ending output, dc level is increased and the ramp of primary ending output dose not change.

Briefly, we have following results for primary ending output with applying dynamic γ stimulation: 1) the bias can be increased by either an increase in k1, k2, or output from the force generators FD. 2) Increased static sensitivity requires an increase in k1, k2. 3) Increased dynamic sensitivity requires an increase in T1/T4 and T2/T4.

4.2. Effects of Static and Dynamic γ Stimulation on Secondary Ending Output

As we can see from **Figure 4(b)**, applying dynamic γ stimulation, almost dose not have any clear effect on secondary ending output and it just increases the static sensitivity a little. With applying static γ stimulation we have following results: 1) the dc level is increased, 2) the ramp of secondary ending response is not changed therefore the dynamic sensitivity is not increased and 3) the static sensitivity is highly increased.

Briefly, we have following results for secondary ending output with applying static γ stimulation: 1) The bias is increased by an increase in k3 or output from the force generator Fs. 2) The static sensitivity is increased by an increase in k3. 3) The dynamic sensitivity is not significantly changed.
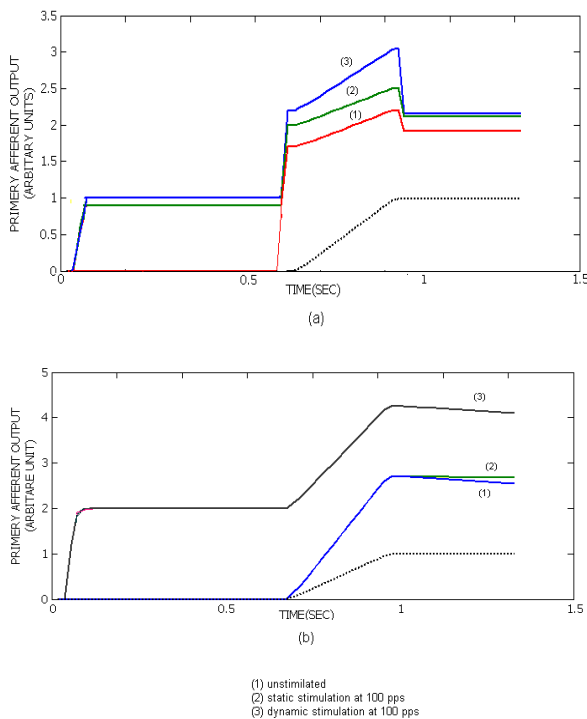
Table 1. Effects of dynamic and static stimulation on bias and dynamic and static stimulation of spindle afferents.

	Unstimulated	Dynamic Fiber Stimulation	Static Fiber Stimulation
Primary ending			
Bias	variable	increase	large increase
Dynamic sensitivity	significant	increase	decrease
Static sensitivity	significant	slight increase	increase
Secondary ending			
Bias	variable	no effect	increase
Dynamic sensitivity	slight	no effect	no effect
Static sensitivity	significant	no effect	increase

The effects of dynamic and static stimulation on bias and dynamic and static sensitivity of spindle afferent is listed in Table I. As we can see from Table I, primary ending is affected either by static and dynamic stimulation. Secondary ending is affected only by static fiber stimulation.

4.3. Effects of an Increase in Dynamic γ Stimulation on Primary Ending Output

Figure 5 shows the effect of an increase in dynamic γ stimulation on primary ending output. Upper curve in **Figure 5** (curve 2) shows the effect of an increase in dynamic γ in compare with mid curve (curve 1) with no increase in dynamic γ stimulation. As we can see from **Figure 5**, with applying an increase in dynamic γ stimulation we observe that: 1) Ramp of primary ending response is increased, therefore dynamic sensitivity is increased too, 2) If we consider primary ending output as a step jump, the height of this step is increased with an increase in dynamic γ, 3) dc level is not changed so we have no change in bias.

4.4. Effects of an Increase in Static γ Stimulation on Primary Ending Output

Figure 6 shows the effect of an increase in static γ stimulation on primary ending output. Upper curve (curve 2) in **Figure 6** shows the primary ending output

(1) unstimilated
(2) static stimulation at 100 pps
(3) dynamic stimulation at 100 pps

Figure 4. Stimulated response of a mammalian muscle spindle during stretch. (a) Primary ending. (b) Secondary ending.
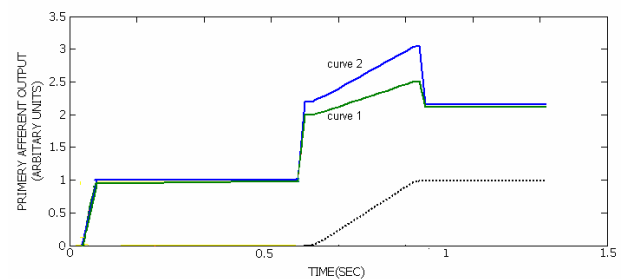
Figure 5. the effect of an increase in γd stimulation on primary ending output. Primary ending output without any increase in γd stimulation (curve 1) and primary ending output with an increase in γd stimulation (curve 2).

with applying an increase in static γ stimulation and mid curve (curve 1) in **Figure 6** shows primary ending output just with applying static γ stimulation. As we can see from **Figure 6**, with applying an increase in γs stimulation, we observe that: 1) The ramp of primary ending response is not changed and as a result, the dynamic sensitivity is not change too. 2) dc level is increased and therefore the bias in increased just a little. 3) Static stimulation is increased just a little.

4.5. Effects of an Increase in Static γ Stimulation on Secondary Ending Output

Figure 7 shows the effect of an increase in static γ stimulation on secondary ending output. Upper curve (curve 2) in **Figure 7** shows the secondary ending output with applying an increase in static γ stimulation and mid curve (curve 1) in **Figure 7** shows primary ending output just with applying static γ stimulation. As we can see from **Figure 6**, with applying an increase in γ stimulation, we observe that: 1) dc level is increased so bias is increased too. 2) static stimulation is increased.

5. DISCUSSION

The greatest difficulty encountered in evaluating the model is quantifying the data on spindle behavior that are presented in the literature. We shall not dwell on that problem here but instead consider the consequences of our chosen model in terms of response to stretch and possible mechanisms of γ control.

Since the model is linear, both primary and secondary steady-state outputs are proportional to the degree of stretch. The primary output is also linearly proportional to stretch velocity if the duration of stretch is not too brief. This is as it should be and is, in fact, the one common feature of the models that have appeared previously [10,11,19,20,21,22].

The most interesting feature of the model however, is that it allows us to isolate the various effects of γ stimulation. To begin with, it is clear that only effect dynamic or static force generators can have is to increase the bias of output. They provide an additive component to the output with no influence on either dynamic or static sensitivities.
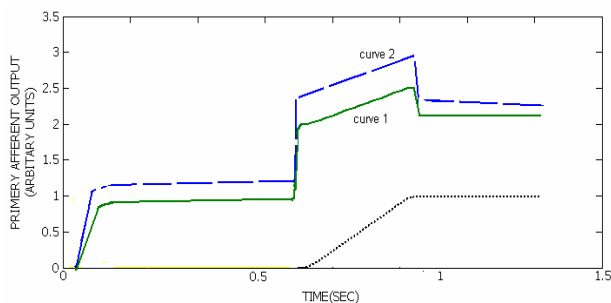
Figure 6. The effect of an increase in γs stimulation on primary ending output.
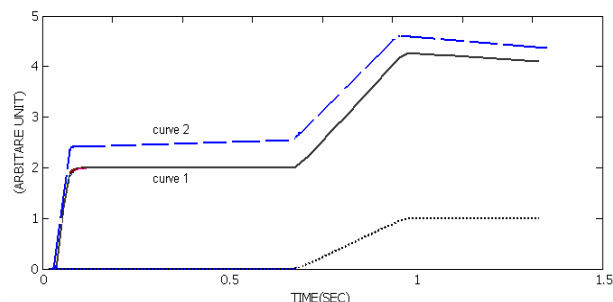
Figure 7. The effect of an increase in γs stimulation on secondary ending output. Secondary ending output without any increase in γs stimulation (curve 1) and secondary ending output with an increase in γs stimulation (curve 2).

The effects of parametric variation are more profound. The static sensitivity is a function solely of the elasticities and any variations in $K1$, $K2$, or $K3$ by γ-efferent activity would appear there. Furthermore, if the spindle is maintained under some degree of passive stretch, an increase in the stiffness of the muscular elasticities will also appear as an increase in the bias, an increase proportional to the change in K and to the initial degree of stretch.

The dynamic sensitivities are more complicated functions of both the elasticities and viscosities but certain eneralizations can be made. In the bag fiber where T4< T1, T2, changes in B1 and B2 will appear as almost proportional changes in primary dynamic sensitivity. By contrast, the dynamic sensitivity of the chain fiber will be only slightly influenced by changes in B1, B2, or B3. Changes in viscosity will not affect the output while the spindle length is constant.

It is instructive, too, to look at the actual degree of deformation of the sensory regions that is caused by stretching the spindle. In the unstimulated case, the peak extension which occurs in the sensory region of the chain fiber is 23 percent of the total spindle stretch. By contrast, the peak extension of the sensory region of the bag fiber is only 0.8 percent of the total stretch. The other 99.2 percent of the deformation occurs in the non-sensory elements. This fact is a direct consequence of the great stiffness of the bag's sensory area compared to the stiffness of the rest of the spindle.

These observations on model behavior suggest that the following conclusions may apply to the physiological spindle.

1) The control exerted by the dynamic γ efferents on the dynamic behavior of the primary afferent may be through modification of the ratio of the viscosity of the nuclear bag to the viscosity of the bag's intrafusal musculature. This effect would be appeared independently of any force generation by the fiber nor would it be seriously affected by a simultaneous increase in muscle stiffness.

2) The control of the static γ efferents on the static

behavior of the two types of afferents may be, in part, modification of the elasticities of either the bag or the chain but may include a large degree of output from the forcegenerators.

3) The control of bias by the γ efferents may be by intrafusal force generation but the existence of this control is open to question because changes in static sensitivity can appear as change in the bias of a stretched spindle.

4) The question of whether the bag fiber contracts in response to dynamic γ stimulation will be difficult to resolve by direct visual observation because the bag is very stiff and deforms only slightly.

5) In light of the above, either of the theories of y-efferent innervation of the intrafusal fibers are acceptable. Even if both plate and trail endings are to be found on both bag and chain fibers, the distinguishing response of the bag fiber would be to only one type (the parametric modifier, presumably the trail ending) while the chain could respond to either or both types of innervation.

6) We should also recognize the fact that the dynamics displayed by the spindle and mimicked by the model are not really sufficiently complex to require a fourth-order transfer function. The purpose of this elaborate model we have presented is to maintain an equivalence between the spindle anatomy and the model topology, but as a black box, simpler models presented previously [10,11], are quite adequate.

REFERENCES

[1] D. Barker, (2002) The motor ininervation of the mammalian muscle spindle, in Nobel Symposium Muscular Afterents and Motor Control, R. Granit, Ed. New York: Wiley.

[2] A. Boyd, (1996) The motor innervation of mammalian muscle spindles, J. Physiol. (London), **159**.

[3] R. W. Banks, (2001) The tenuissiumus muscle of the cat, J. Physiol. (London), **133**.

[4] D. Barker (1999) The innervation of mammalian neuro-mulscular spindles, J. Physiol. (London), **140**.

[5] (2000) Simple and compound mammalian muscle spindles, J. Physiol. (London), **145**.

[6] D. Barker and I. A. Boyd, (2004) in Nobel Symposium Muscular Afterents and Motor Control, R. Granit, Ed. New York: Wiley.

[7] G. C. Agarwal, B. M. Berman, and L. Stark, Studies in postural control systems, part 1: torque disturbance input, **6**, 116−121.

[8] K. Diete-Spiff, (2001) Tension development by isolated muscle spindles of the cat, J. Physiol. (London), **193**.

[9] K. Krnjevk and N. M. Van Gelder, (2002) Tension changes in crayfish stretch receptors, J. Physiol. (London), **159**.

[10] G. C. Agarwal, G. L. Gottlieb, and L. Stark, (March 2004) Models of muscle proprioceptive receptors, presented at the University of Michigan-NASA Conf. Manual Control.

[11] G. L. Gottlieb, G. C. Agarwal, and L. Stark, (March 2003) Stretch receptor models, part I single-efferent single-afferent innervation, IEEE Trans. Man-Machine Systems, MMS-**10**, 17−27.

[12] A. Boyd, (2001) The behavior of isolated mammalian muscle spindles with intact innervation, J. Physiol. (London), **186**.

[13] (2001) The mechanical properties of mammalian intrafusal muscle fibers, J. Physiol. (London), **187**.

[14] P. Bessou and Y. Laporte, (2001) Observations on static fusimotor fibres, in Nobel Synmposium-Muscular Afferents and Motor Control, R. Granit, Ed. New York: Wiley.

[15] P. Bessou, Y. Laporte, and B. Pages, (2001) Similitude des effets (statiques ou dynamiques) exerces par des fibres fusimotrices le chat, J. Physiol, Paris, **58**.

[16] B. Appelberg, P. Bessou, and Y. Laporte, (2001) Action of static and dynamic fusimotor fibres on secondary endings of cats' spindles, J. Physiol. (London), **185**.

[17] E. Emonet-Denand, Y. Laporte, and B. Pages, (2001) Fibres fusimotrices statiques et fibres fusimotrices dynamiques chez le lapin, Arch. Ital. Biol., **104**.

[18] Crowe and P. B. C. Matthews, (2003) The effects of stimulation of static and dynamic fusimotor fibres on the response to stretching of the primary endings of muscle spindles, J. Physiol. (London), **174**.

[19] J. C. Houk, R. Cornew, and L. Stark, (2001) A model of adaptation in amphibian spindle receptors, J. Theoret. Biol., **12**.

[20] Anndersson, G. Lennerstrand, and U. Thoden, Cat muscle spindle model, Dig. 1999 Internatl. Conf. on Medical and Biological Engineering (Stockholm).

[21] M. D. Angers, (2001) Model mecanique de fuseau neuromusculaire de-efferente: Terminaisons primaires et secondaires, Compt. Rend. Acad. Sci. (Paris), **261**.

[22] Crowe, (2003) A mechanical model of the mammalian muscle spindle, J. Theoret. Biol., **21**.

APPENDIX   1

The following equations relate the block simulation parameters (**Figure 3**) to the model parameters (**Figure 2**) as determined by (3) and (4).

1) *a* parameters:

$$a_1 = -\frac{K_1 + K_6}{B_1}, \quad a_2 = \frac{K_1}{B_1}$$

$$a_3 = \frac{K_6}{B_1}, \qquad a_4 = -\frac{1}{B_1}$$

2) *c* parameters:

$$c_1 = \frac{B_2}{B_2 + B_4}, \quad c_2 = \frac{K_2}{B_2 + B_4}$$

$$c_3 = \frac{K_2 + K_4}{B_2 + B_4}, \quad c_4 = \frac{1}{B_2 + B_4}$$

3) *d* parameters:

$$d_1 = \frac{B_3}{B_3 + B_5}, \quad d_2 = \frac{K_3}{B_3 + B_5}$$

$$d_3 = -\frac{K_3 + K_5}{B_3 + B_5}, \quad d_4 = \frac{1}{B_3 + B_5}$$

4) *e* parameters:

$$e_1 = -K_6 H$$

$$e_2 = -\left[\frac{B_4 K_2}{B_2 + B_4} + \frac{B_5 K_3}{B_3 + B_5}\right] H$$

$$e_3 = \left[\frac{B_4 K_2 - B_2 K_4}{B_2 + B_4}\right] H, \quad e_4 = \left[\frac{B_5 K_3 - B_3 K_5}{B_3 + B_5}\right] H$$

$$e_5 = K_6 H, \qquad e_6 = -\left[\frac{B_4}{B_2 + B_4}\right] H$$

$$e_7 = -\left[\frac{B_5}{B_3 + B_5}\right] H$$

where

$$H = \frac{1}{\dfrac{B_2 B_4}{B_2 + B_4} + \dfrac{B_3 B_5}{B_3 + B_5}}$$

APPENDIX   2

The following parameter values were used in the simulation shown in **Figure 4**:

$K_1 = 0.02$ $B_1 = 0.25$

$K_2 = 0.02$ $B_2 = 0.025$

$K_3 = 0.03$ $B_3 = 0.001$

$K_4 = 4.0$ $B_4 = 0.01$

$K_5 = 0.03$ $B_5 = 0.001$

$K_6 = 2.0$

$f_D = $ dynamic γ firing rate

$f_S = $ static γ firing rate

$$\frac{\partial F_D}{\partial f_D} = 0.0003, \qquad \frac{\partial F_S}{\partial f_S} = 0.0003$$

$$\frac{\partial K_1}{\partial f_D} = \frac{\partial K_2}{\partial f_D} = \frac{\partial B_1}{\partial f_D} = \frac{\partial B_2}{\partial f_D} = 0.01$$

$$\frac{\partial K_3}{\partial f_S} = \frac{\partial B_3}{\partial f_S} = 0.01$$

$\alpha / \beta = 30$ (see(5)), K is given in N/m and B in N·s/m

Multi-frequency bioimpedance measurements of rabbit shanks with stress fracture

Xing Zhang[1], Er-Ping Luo[1], Guang-Hao Shen[1], Kang-Ning Xie[1], Tian-Yi Song[1], Xiao-Ming Wu[1], Wen-Ke Gan[1], Yi-Li Yan[1]

[1]Department of Military Medical Equipment & Metrology, Faculty of Biomedical Engineering, the Fourth Military Medical University, Xi'an, China. Correspondence should be addressed to Er-Ping Luo (Luoerping@fmmu.edu.cn), Tel: +86-29-84774849.

ABSTRACT

Purpose: The objective of this research is to investigate whether bioimpedance is useful to indicate a shank's physical condition during training. Methods: Bioimpedance was applied to monitor the condition of 8 rabbits' shanks in 3 weeks, during which the rabbits were trained for regular excessive jump daily. Nine tibias in 16 developed stress fracture after the 3-week training. Results: According to the analysis of the bioimpedance data, we found that changing pattern of bioimpedance properties of shanks which were more liable to suffer from SF was different from that of shanks which were not during training. Conclusions: This suggests that bioimpedance may be used to monitor the physical condition of a limb, imply its liability to develop stress fracture, and indicate stress fracture during training.

Keywords: Bioimpedance Measurements; Stress Fracture; Bioimpedance Monitoring

1. INTRODUCTION

Stress fracture (SF) is caused by repetitive overloading of a bone, exceeding its mechanical capacity. SF can be classified into two types: fatigue fractures, which develop by excessive loads in normal bones, and insufficiency fractures, with normal loads acting up on bones with reduced mechanical properties [1,2]. What we studied was the former type, fatigue fractures.

Incidence of SF is relatively high, especially in military recruits and athletes training. Specifically, tibia is the most commonly involved site. The early symptom can appear between 10 and 12 days after the beginning of training in most SFs. Studies of military recruits reported an incidence varying from 2% to 64% [3].

Rapid and safe recovery is best ensured with the early

diagnosis and conservative therapy. However, SF's diagnosis seems very difficult and costly, and it is often neglected, which could explain why SF always leads to more serious problems in the absence of enough care but still with continuing training. The most important diagnostic study is a plain radiograph. However, in early stages, the sensitivity was as low as 10%, rising to 30–70% at follow-up [4]. Other diagnostic techniques are bone scanning, CT (computed tomography), MRI (magnetic resonance imaging), and SPECT (single photon emission computed tomography) [5,6,7].

If plain radiographs appear normal, some researchers advise referring to MRI, as a number of studies have shown that MRI has a high sensitivity and specificity [8, 9,10,11]. But even with MRI, it is, in some cases, difficult to differentiate SFs from infections, bone infarctions or neoplastic lesions (such as osteosarcoma or Ewing sarcoma) [12,13,14]. Most doctors believe that SPECT is the best diagnostic technique for SF. Some studies have shown that just like MRI, it has a relatively high sensitivity and specificity while still confuses sometimes when some other diseases present [15]. However, all the techniques used are costly, making them difficult to be popularized.

Bioimpedance, defined as the measurement of the electrical impedance of a biological sample, which was first applied to total body water (TBW) measurement [16], is non-invasive and simple, and can be repeated in short time intervals during therapy. Furthermore, it can reflect some interesting physiological conditions and events. Until now, it has been used on cellular measurements, volume changes, body composition, tissue classification, tissue monitoring, electrical impedance tomography, and so on. But there are few reports about the study of its application on monitoring physical condition of a limb.

In this study, electrical bioimpedance of rabbit shanks $Z^*=R+jX$ (the superscript * means that Z is a complex number) was measured at 31 frequencies, ranging from 1kHz to 1MHz. In this range, the frequency response shows a major dispersion: β [17,18]. The β dispersion is associated with Maxwell-Wagner relaxation resulting from the capacitive charging of cell membranes via in-

tracellular and extracellular pathways, which typically occurs in inhomogeneous materials [19]. The objective of this research is to investigate whether bioimpedance is useful to indicate a shank's physical condition and SF during training.

2. MEASUREMENT PROTOCOL

Eight rabbits (white New Zealand rabbits, 4 months old, 2.2 ± 0.2kg weight, 4 male rabbits, 4 female rabbits), were used in the experiment. Every rabbit took part in passive jump training one hour and a half per day by means of discontinuous current stimulation (2.4μA, 10kV), about 7 times per min. The training lasted for 21 days. The stimulating equipment, designed and produced by us, was a cage (2m in length, 1.2m in width and 0.92m in height) with metal pipes on the bottom side by side, and the pipes were electrified by positive and negative current alternately.

We measured electrical bioimpedance of each shank every 3 days. For the measurement, 1260 impedance/ gain-phase analyzer (1260, Solartron Company, UK) was used. The subjects were anesthetized (pentobarbital sodium, 30mg/kg), fixed to experimental table before four Ag-AgCl spiculate electrodes (0.5mm in diameter) were inserted on the shank of the posterior limb for impedance measurement.

A pair of the electrodes served as the current provider and the rest pair as potential detector (**Figure 1**). All the four electrodes were inserted into shank's skin after skin preparation with depth about 1 cm toward the middle of the shank. The potential electrode on proximal shank was placed about 2cm 'downstream' of the current electrode, and the potential electrode on distal shank was placed about 2cm apart from the other current electrode. The distance between two potential electrodes was 6cm. The positions of the electrodes are shown in **Figure 1**. We marked the location of every electrode on every
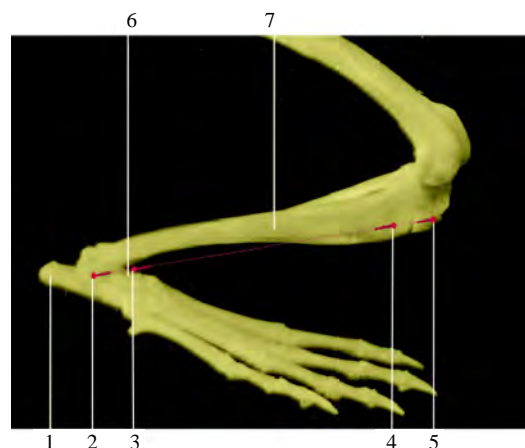
Figure 1. Electrode positions in bioimpedance measurement: 1, calcaneal tuberosity; 2, 5, positions of current electrodes; 3, 4, positions of potential electrodes; 6, talus; 7, tibia.

shank according to its anatomical structure and the distance between electrodes.

Impedance was measured at 31 frequencies, ranging from 1kHz to 1MHz, with a current of 0.5mA. Reactance and resistance at different frequencies are fitted into a semicircle [20] (**Figure 2**).

We measured body mass of each rabbit daily, and controlled it by food. The body mass of each rabbit changed in the range of ±0.2kg referenced to its first measurement.

In the 10th day and 21st day of our experiment, the rabbits were diagnosed by SPECT and X-ray images. Based only on the result of SPECT and X-ray images the doctor suggested that there was no tibia suffered from SF on day 10, and 9 tibias in 16 suffered from SF on day 21. The 9 tibias suffered from SF were rabbit 1's both tibias, rabbit 2's both tibias, rabbit 4's left tibia, rabbit 6's both tibias, rabbit 7's left tibia and rabbit 8's right tibia. An example SPECT results is shown in **Figure 3**.
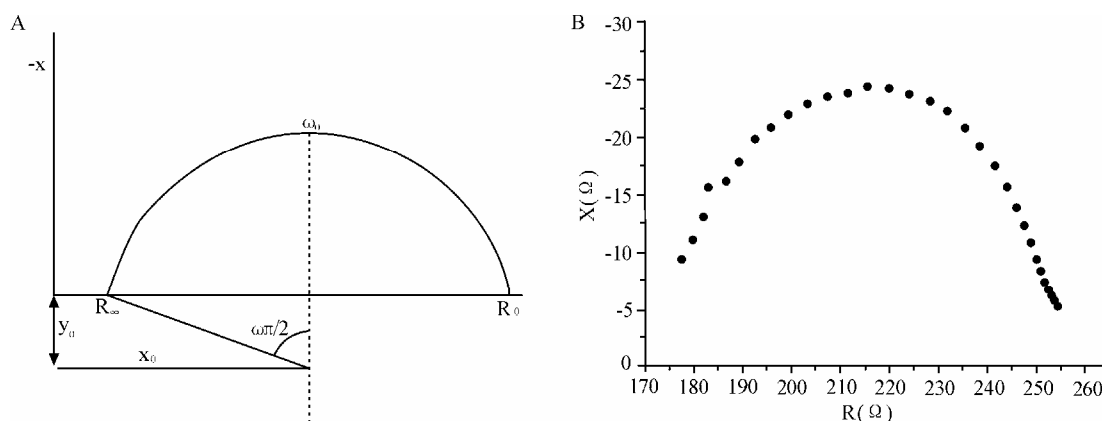
Figure 2. Impedance plotted in complex impedance plane. (A) Cole Plot consists of semicircle with its midpoint below horizontal axis; x_0 and y_0=co-ordinates of midpoint; r =radius of semicircle. Horizontal axis: real part of Z(R); R_0=value of Z at zero frequency; R_∞= value of Z at infinite frequency. Vertical axis: imaginary part of Z (multiplied by minus one); ω_0=angular frequency at maximum reactance X. (B) Bioimpedance data measured; vertical axis: X (reactance); horizontal axis: R (resistance). Each point represents a measurement at a certain frequency, data from one of our measurements.
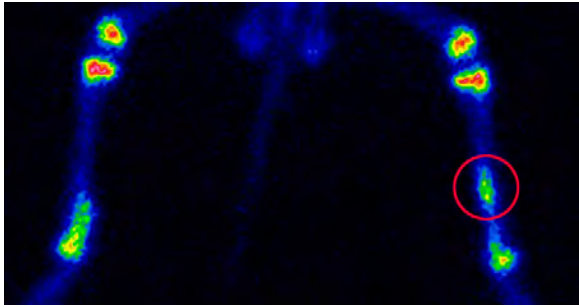
Figure 3. An example SPECT result of a rabbit's shanks. The red circle indicates the SF site. No fracture was found in the counterpart X-ray image.

3. DATA ANALYSIS

The data obtained were values of R, X, Z and Φ at 31 frequencies from 1kHz to 1MHz (R=resistance, X=reactance, Z=impedance, Φ=phase angle). It is assumed that the plot of R against X gives a semicircular arc (eqn 1 is valid) in the complex impedance plane which is called Cole Fitting. This is an approximation and strictly valid only in the case of Debye dispersion ($\alpha=1$). The co-ordinates of the centre (x_0, y_0) and the radius r were calculated by iterative least square fitting algorithm. Then values of other parameters, such as R_0, R_∞, α, etc were calculated easily (R_0 =value of Z at zero frequency, R_∞ = value of Z at infinite frequency, $\alpha\pi/2=$ depressing angle). As already stated the Cole function is given by

$$Z^* = R_\infty + \frac{R_0 - R_\infty}{1 + (j\omega/\omega_0)^\alpha} \qquad (1)$$

The parameters of f_0, R_0, R_∞, etc. are given by (f_0 =frequency at maximum phase angle, ω_0 =angular frequency at maximum reactance X)

$$R_0 = x_0 + \sqrt{r^2 - y_0^{\,2}} \qquad (2)$$

$$R_\infty = x_0 - \sqrt{r^2 - y_0^{\,2}} \qquad (3)$$

$$\alpha = 1 - \frac{2}{\pi}\arcsin(\frac{|y_0|}{r}) \qquad (4)$$

$$\omega_0 = \frac{j\omega}{\left[\frac{R_0 - Z^*}{Z^* - R_\infty}\right]^{\frac{1}{\alpha}}}, \quad f_0 = \frac{\omega_0}{2\pi} \qquad (5)$$

In order to calculate x_0, y_0 and r, we define

$$F(x_0, y_0, r) = \sum_{i=1}^{N}\left[\sqrt{(x_i - x_0)^2 + (y_i - y_0)^2} - r\right]^2 \qquad (6)$$

The equations below optimize the set of parameters x_0, y_0 and r

$$\frac{\partial F}{\partial x_0} = 0, \frac{\partial F}{\partial y_0} = 0, \frac{\partial F}{\partial r} = 0 \qquad (7)$$

Using iterative method, then

$$x_0^{(k+1)} = \frac{1}{N}\left[\sum_{i=1}^{N} x_i - r^{(k)} \sum_{i=1}^{N} \frac{x_i - x_0^{(k)}}{\sqrt{(x_i - x_0^{(k)})^2 + (y_i - y_0^{(k)})^2}}\right] \qquad (8)$$

$$y_0^{(k+1)} = \frac{1}{N}\left[\sum_{i=1}^{N} y_i - r^{(k)} \sum_{i=1}^{N} \frac{y_i - y_0^{(k)}}{\sqrt{(x_i - x_0^{(k)})^2 + (y_i - y_0^{(k)})^2}}\right] \qquad (9)$$

$$r^{(k+1)} = \frac{1}{N}\left[\sum_{i=0}^{N} \sqrt{(x_i - x_0^{(k)})^2 + (y_i - y_0^{(k)})^2}\right] \qquad (10)$$

Using the equations above, with a set of proper initial values and a suitable value of k, parameters can be calculated easily, and this was used in our experiment.

4. MODEL CONSIDERATIONS

There are two important bioimpedance models reported, lumped circuit model, and physiological model. They are both macroscopically models, using global information to explain the microscopical changes of tissue. Lumped circuit model was used in our experiment.

Impedance Z is a complex number

$$Z^* = R + jX (j = \sqrt{-1}) \qquad (11)$$

When −X and R of a biological tissue are plotted on the complex impedance plane over a suitable wide-frequency range, we can get a semicircle, as is shown in **Figure 2** [21].

Considering the main constituents of the cells, a simple electrical model for the cell can be proposed (**Figure 4**). The current injected into the extracellular medium can flow through the cell across the bilayer lipid membrane (BLM) (C_m) or across the ionic channels (R_m) or can circulate around the cell (R_e). Once the current has penetrated into the cell it 'travels' trough the intracellular medium (R_i) and leaves the cell across the membrane ($R_m \| C_m$) (**Figure 4**). The circuit on the right of **Figure 4** is equivalent to the middle model after performing some simplifications. The same simplifications can be applied to reduce a tissue composed by many cells to a single cell equivalent circuit. Of course, this simplification is correct only in an ideal condition. However, it's simple and executable, and can be accepted.

R_e, R_i, and C_m can be calculated by
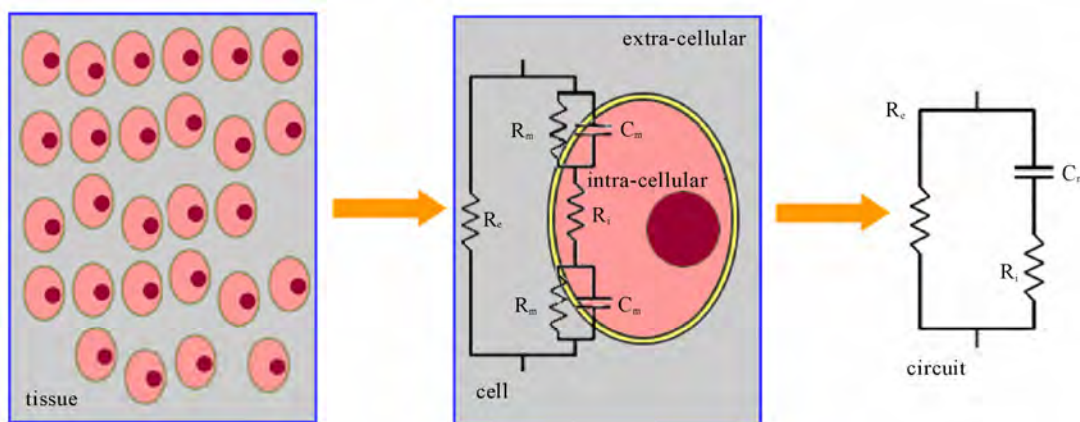
Figure 4. One of lumped circuits that has impedance given by **Eq.1**. R_e= extracellular resistance; R_i = intracellular resistance; C_m: capacitance of cell membrane; R_m: the bilayer lipid membrane (BLM) resistance.

$$R_i = \frac{R_0 R_\infty}{R_0 - R_\infty}, R_e = R_0 \tag{12}$$

$$C_m = \frac{1}{2\pi f_0 (R_e + R_i)} \tag{13}$$

5. RESULTS

Eight rabbits with almost the same age, and almost the same weight, had been trained in 21 days. The impedance at 31 frequencies ranging from 1 kHz to 1MHz was measured repeatedly during their training. Finally, nine tibias developed SF, and others were in healthy state. We grouped the bioimpedance data of the shanks into two groups, one group from shanks suffered from SF finally (group 1), and the other from shanks without SF finally (group 2). Group 1 had 9 tibias and group 2 had 7 tibias.

5.1. Changing Pattern of Bioimpedance Properties of Shanks which are More Liable to Suffer from SF is Different from that of Shanks which are not During Training

From the data, the following parameters were calculated: R_0, R_∞, $\alpha\pi/2$, f_0, C_m, R_i. These parameters between two groups were not significantly different (All P>0.05, unpaired Student's t-test) in the first measurement. We didn't contrast these parameters directly for each shank's individual difference, such as skeleton, muscle and etc. which induced different electric properties, in the following measurements. So, we defined a new parameter d as a measurement of each parameter's change to its first measurement of a shank. That is to say, we used the first measurement as a baseline, and d represented the change of one parameter between its base-

line and one of the following measurements of a shank. For example, d_{R_e}, defined one shank's parameter R_e's change against the shank's first measurement. From the self-contrast of each shank's data, parameters such as x_0, α, R_e, R_0, R_∞, R_i had decreased significantly (All P<0.05, unpaired t-test) in both groups, and parameters such as C_m had increased significantly (All P<0.05, unpaired t-test) in both groups (**Figure 5**).

As it can be seen in **Figure 5**, the bioimpedance parameters changed during training, and these changes were more significant in Group 1 than that in Group 2. We calculated each parameter's Average Growth Rate (AGR, AGR=$\sqrt[n]{d_n/d_0} - 1$), and there was a statistical significance between two groups (All P<0.05, unpaired t-test) (**Figure 6**). Abstract value of AGR of each parameter in Group 1 was higher than that in Group 2.

5.2. Bioimpedance Measurements may be Used to SF's Early Diagnosis

We also contrasted the parameter f_0's changes in two groups, and the changes were more interesting. f_0, as the characteristic frequency, had no significant change in Group 2 during the entire training period, but it had a significant change in Group 1 after the fourth measurement (**Figure 7**). It had increased after the fourth measurement, and we hadn't found any SF from SPECT and X-ray images of the 10th day's diagnosis.

5.3. Female Rabbits are More Likely to Suffer from SF

There were six female shanks, and three male shanks suffered from SF in group 1. With the same content and intensity of training, female rabbits were more likely to suffer from SF.
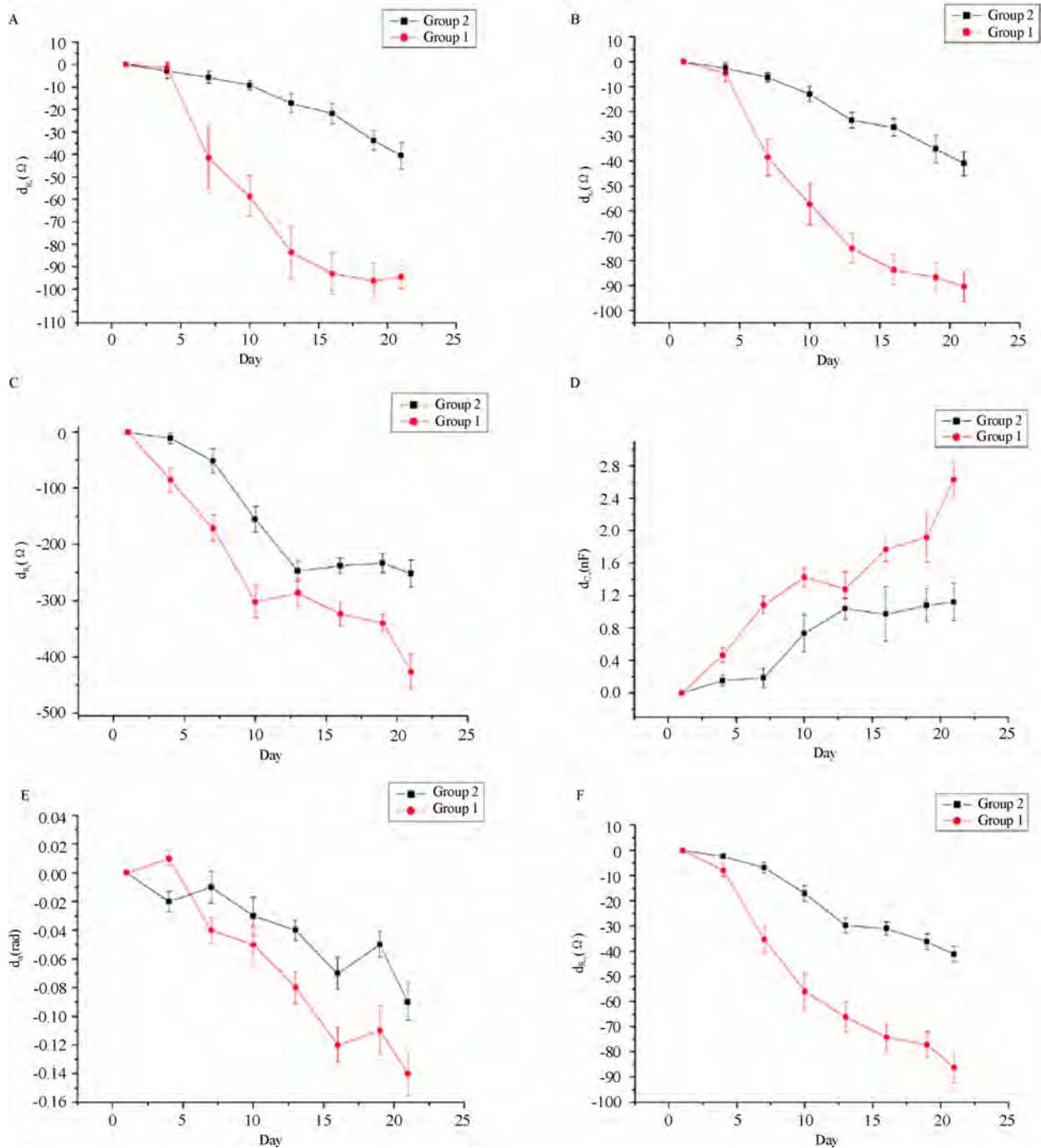
Figure 5. Bioimpedance parameters' changes in two groups: vertical axis: bioimpedance parameter's change; horizontal axis: Day: days after rabbits' training. (A) R_e: extracellular resistance, Ω. (B) x_0: horizontal co-ordinate of center. (C) R_i: intracellular resistance, Ω. (D) C_m: capacitance of cell membrane, nF. (E) α: απ/2 angle of depression (Figure 2), rad. (F) R_∞: resistance at infinite frequency, Ω.

6. DISCUSSION AND CONCLUSIONS

SF's risk factors can be typically grouped into extrinsic and intrinsic risk factors. Extrinsic risk factors for SF are those in the environment or external to the individual, including the type of activity and factors involving training, equipment, and the environment. Intrinsic risk factors for SF refer to characteristics within the individual, including skeleton, muscle, joint, and biomechanical factors, as well as physical fitness and gender [22]. In
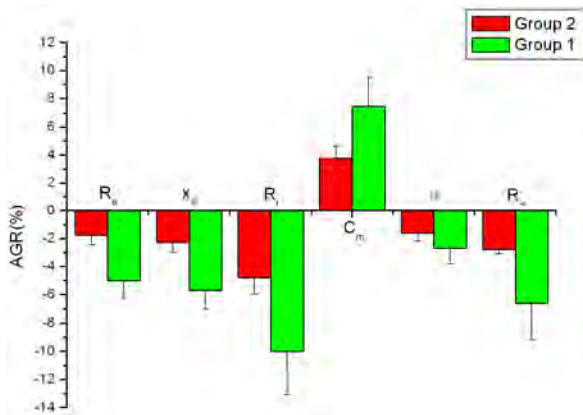
Figure 6. Bioimpedance parameters' AGR in two groups: vertical axis: AGR: average growth rate; horizontal axis: parameters.
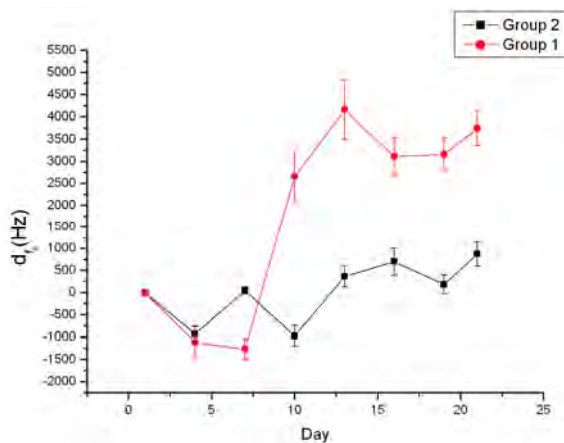
Figure 7. Bioimpedance parameter f_0's changes in two groups: vertical axis: f_0: the frequency at the maximum value of X (reactance), Hz; horizontal axis: Day: days after rabbits' training.

this study, extrinsic risk factors were almost the same to every rabbit, and what were different were intrinsic risk factors. This leaded some of them, not all of them, to suffer from SF.

All rabbit shanks' bioimpedance changed to some extent during the period of training. This may be caused by the changes of rabbit shank cell's structure, and circulation. We can conclude that exercises can decrease tissue cell's extra- and intracellular resistance and increase capacitance of cell membrane. With the same extrinsic factors, individual difference, as one of the most important intrinsic factors, is crucial to SF. Therefore, the bioimpedance parameters' changes may reflect one bone's liability to suffer from SF, and according to the results, shank with quicker changes in these parameters during training time is more likely to suffer from SF.

R_e and R_i's reduction suggest that the extra- and intracellular resistance reduce during training, maybe

caused by the change of the dielectric properties of the cell membranes and their interactions with extra and intracellular electrolytes and the change of the diffusion processes of the ionic species in extra- and intracellular. f_0's increase in group 1 after the tenth day of training may suggest that SF has changed capacitance of cell membrane, caused by the change of the structure of BLM, such as the property of ionic channels and ion pumps.

If f_0 can reflect SF of a bone, then f_0's change is earlier than that of SPECT, making possible bioimpedance measurements as early diagnosis of SF.

Also, tissue injury caused by electrodes puncture could also change properties of tissue's bioimpedance. We ignored this factor because we found that bioimpedance had been changed little by it in our preliminary experiment.

Gender is also a very important risk factor of SF. It's reported that women were more likely to suffer from SF than men [23]. This can be explained in two aspects, anatomical aspect, and physiological aspect. In anatomical considerations, compared with male, female have different characteristics in bones and joints, muscles, and ligaments and joints. For example, lower extremity anatomic differences between genders may predispose female to certain overuse injuries, such as SF. In physiological considerations, changes in estrogen serum levels, percentage of fat, heart size, diastolic and systolic pressures and so on, start to be more obvious between male and female after the stabilization of hormonal axis during the pubertal years.

Many authors argue that it's difficult to imply bone's information from the global bioimpedance of a shank. It's true in the fact that bone's resisitivity is extremely higher than that of muscle and other tissues [24]. If we define rabbit shank as a model of parallel connection of muscle, bone, blood and skin, the current into the cell will 'travel' trough the muscle, blood and skin rather than bone, and then what we get is the information of muscle, blood and skin rather than bone. We agree with this hypothesis to some extent. But SF' causing factor includes the changes of all those tissues. We may not measure the direct information of a bone, but we may use the global information to imply the situation of a bone. Our experiment supports this hypothesis.

We therefore conclude that this method may be used to monitor the physical condition of human tissues, and that SF can be implied by the changing pattern of bioimpedance properties during training.

REFERENCES

[1]   R. H. Daffner and H. Pavlov, (1992) Stress fractures: current concepts, AJR Am J Roentgenol, **159(2)**, 245−252.

[2] R. L. Pentecost, R. A. Murray, and H. H. Bridley, (1964) Fatigue, insufficiency, and pathologic fractures, JAMA, **28(187)**, 1001− 1004.

[3] M. Giladi, C. Milgrom, A. Simkin, and Y. Danon, (1991) Stress fractures: Identifiable risk factors, Am J Sports Med, **19(6)**, 647−652.

[4] M. J. Kiuru, H. K. Pihlajamaki, and J. A. Ahovuo, (2004) Bone stress injuries, Acta Radiol, **45(3)**, 317−326.

[5] M. Murcia, M. D., R. E. Brennan, M. D., and J. Edeiken, M. D., (1982) Computed tomography of stress fracture, Skeletal Radiol, **8**, 193−195.

[6] A. D. Perron, W. J. Brady, T. A. Keats, (2001) Principles of stress fracture management: The whys and hows of an increasingly common injury, Postgrad Med, **110(3)**, 115−8, 123−4.

[7] M. T. Reeder, B. H. Dick, J. K. Atkins, A. B. Pribis, J. M. Martinez, (1996) Stress fractures: current concepts of diagnosis and treatment, Sports Med, **22(3)**, 198−212.

[8] L. M. Fayad, S. Kawamoto, I. R. Kamel, D. A. Bluemke, J. Eng, F. J. Frassica, and E. K. Fishman, (2005) Distinction of long bone stress fractures from pathologic fractures on cross-sectional imaging: How successful are we? AJR Am J Roentgenol, **185(4)**, 915−924.

[9] A. Feydy, J. Drapé, E. Beret, L. Sarazin, E. Pessis, A. Minoui, A. Chevrot, (1998) Longitudinal stress fractures of the tibia: Comparative study of CT and MR imaging, Eur Radio, **8(4)**, 598−602.

[10] M. Gaeta, F. Minutoli, E. Scribano, G. Ascenti, S. Vinci, D. Bruschetta, L. Magaudda, A. Blandino, (2005) CT and MR imaging findings in athletes with early tibial stress injuries: comparison with bone scintigraphy findings and emphasis on cortical abnormalities, Radiology, **235(2)**, 553−561.

[11] I. Elias, A. C. Zoga, S. M. Raikin, J. R. Peterson, M. P. Besser, W. B. Morrison, and M. E. Schweitzer, (2008) Bone stress injury of the ankle in professional ballet dancers seen on MRI, BMC Musculoskelet Disord, **9(1)**, 39, Published online, March 28, 2008.

[12] M. W. Anderson and A. Greenspan, (1996) Stress frac-

tures, Radiology, **199(1)**, 1−12.

[13] A. Fottner and C. Birkenmaier, (2008) Stress fractures presenting as tumours: A retrospective analysis of 22 cases: Reply to Agarwal and Gulati, Int Orthop, Published online, August 6, 2008.

[14] D. Pauleit, T. Sommer, J. Textor, S. Flacke, C. Hasan, K. Steuer, D. Emous, and H. Schild, (1999) MRI diagnosis in longitudinal stress fractures: Differential diagnosis of Ewing sarcoma, Rofo, **170(1)**, 28−34.

[15] S. T. Zwas, R. Elkanovitch, and G. Frank, (1987) Interpretation and classification of bone scintigraphic findings in stress fractures, J Nucl Med, **28(4)**, 452−457.

[16] A. Thomasset, (1962) Bioelectrical properties of tissue impedance, Lyon Medical, **207**, 107−118.

[17] J. R. Bourne (ed.), J. -P. Morucci, M. E. Valentinuzzi, B. Rigaud, C. J. Felice, N. Chauveau, and P. M. Marsili, (1996) Bioelectrical impedance techniques in medicine, Critical Reviews in Biomedical Engineering, **24(4−6)**.

[18] H. P. Schwan, (1957) Electrical properties of tissue and cell suspensions, Adv Biol Med Phys, **5**, 147−209.

[19] B. Rigaud, L. Hamzaoui, N. Chauveau, M. Granie, J. -P. Scotto D. Rinaldi, and J. -P. Morucci, (1994) Tissue characterization by impedance: a multifrequency approach, Physiol Meas, **15**, A13− A20.

[20] K. S. Cole, (1940) Permeability and impermeability of cell membranes for ions, Cold Spring Harbor Symp Quant Biol, **8**, 110−122.

[21] E. T. Mcadams and J. Jossinet, (1996) Problems in equivalent circuit modelling of the electrical properties of biological tissues, Bioelectrochem, Bioenergetics, **40**, 147−152.

[22] S. J. Warden, D. B. Burr, and P. D. Brukner, (2006) Stress fractures: Pathophysiology, epidemiology, and risk factors, Current Osteoporosis Reports, Published online, March 26, 2008.

[23] A. Ivković, M. Franić, I. Bojanić, and M. Pećina, (2007) Overuse injuries in female athletes, Croat Med J, **48(6)**, 767−778.

[24] T. J. C. Faes, H. A. van der Meij, J. C. de Munck, and R. M. Heethaar, (1999) The electric resistivity of human tissues (100Hz–10MHz): A meta-analysis of review studies, Physiol Meas, **20**, R1−R10.

Functional brain imaging with use of a new and powerful neuroimaging technique

Mohammad Karimi Moridani[1]

[1]Biomedical Engineering Department, Science and Research Branch, Islamic Azad University, Tehran, Iran.
Email: Karimi.m@srbiau.ac.ir

ABSTRACT

Most of the information available on the human brain came from subjects who had sustained major head wounds, or who suffered from various mental disorders. By determining the extent of brain damage, and the nature of the loss of function, it was possible to infer which regions of the brain were responsible for which function. With the development of the imaging techniques of computerised tomography (CT) and magnetic resonance imaging it was possible to be more specific as to the location of damage in brain injured patients. The measurement of the electrical signals on the scalp, arising from the synchronous firing of the neurons in response to a stimulus, known as electroencephalography (EEG), opened up new possibilities in studying brain function in normal subjects. However it was the advent of the functional imaging modalities of positron emission tomography (PET), single photon emission computed tomography (SPECT), functional magnetic resonance imaging (fMRI), and magnetoencephalography (MEG) that led to a new era in the study of brain function. In this paper the mechanisms of the techniques mentioned above are outlined, together with an assessment of their strengths and weaknesses. Then an introduction to the Metabolism and Blood Flow in the Brain is given. This is followed by a more detailed explanation of functional MRI and how such experiments are performed.

Keywords: Functional Magnetic Resonance Imaging; Brain Function; EEG

1. INTRODUCTION

Functional brain imaging using MRI (functional MRI or fMRI) has become a valuable tool for studying function/ structure relationships in the human brain in both normal and clinical populations. This paper describes the physiological changes associated brain with activity, including changes in blood flow, volume, and oxygenation. The latter of these, known as Blood Oxygenation Level Depended (BOLD) contrast, is the most common approach for functional MRI, but it is related to brain activity via a variety of complex mechanisms. Blood oxygenation level dependent functional MRI and near infrared optical tomography have been widely used to investigate hemodynamic responses to functional stimulation in the human brain. The temporal hemodynamic response shows an increased total hemoglobin concentration, which indicates an increased cerebral blood volume (CBV) during physiological activation. Blood Oxygenation Level Dependent signal indirect measure of neural activity. The signal variations induced by respiration and cardiac motion decrease the statistical significance in functional MRI data analysis. Physiological noise can be estimated and removed adaptively using signal projecting technique with the actual functional signal preserved. We estimate and remove the physiological noise from the magnitude images. This method is a fully data-driven method, which can efficiently and effectively reduce the overall signal fluctuation of functional MRI data. Assumes that the MRI data recorded on each trial are composed of a signal added with noise Signal (random) is present on every trial, so it remains constant through averaging and Noise randomly varies across trials, so it decreases with averaging Thus, Signal-to-Noise Ratio (SNR) increases with averaging.

2. COMPARISON OF THE FUNCTIONAL BRAIN IMAGING MODALITIES

The brain imaging techniques that had been presented in this paper all measure slightly different properties of the brain as it carries out cognitive tasks. Because of this the techniques should be seen as complementary rather than competitive. All of them have the potential to reveal much about the function of the brain and they will no doubt develop in clinical usefulness as more about the underlying mechanisms of each are understood, and the hardware becomes more available. A summary of the

strengths and weaknesses of the techniques is presented in **Table 1** [5].

2.1. SPECT and PET

The imaging modalities of single photon emission computed tomography (SPECT) and positron emission tomography (PET) both involve the use of radioactive nuclides either from natural or synthetic sources. Their strength is in the fact that, since the radioactivity is introduced, they can be used in tracer studies where a radiopharmaceutical is selectively absorbed in a region of the brain. The main aim of SPECT as used in brain imaging, is to measure the regional cerebral blood flow (rCBF). The earliest experiments to measure cerebral blood flow were performed in 1948 by Kety and Schmidt [1]. They used nitrous oxide as an indicator in the blood, measuring the differences between the arterial input and venous outflow, from which the cellular uptake could be determined.

This could only be used to measure the global cerebral blood flow, and so in 1963 Glass and Harper[2], building on the work of Ingvar and Lassen, used the radioisotope Xe-133, which emits gamma rays, to measure the regional cerebral blood flow. The development of computed tomography in the 1970's allowed mapping of the distribution of the radioisotopes in the brain, and led to the technique now called SPECT [3].

2.2. EEG and MEG

Measuring the electrical signals from the brain has been carried out for several decades [4], but it is only more recently that attempts have been made to map electrical and magnetic activity. The electroencephalogram is recorded using electrodes, usually silver coated with silver chloride, attached to the scalp and kept in good electrical contact using conductive electrode jelly. One or more active sites may be monitored relative to a reference electrode placed on an area of low response activity such as the earlobe. The signals are of the order of 50 microvolts,

and so care must be taken to reduce interference from external sources, eye movement and muscle activity. Several characteristic frequencies are detected in the human EEG. For example, when the subject is relaxed the EEG consists mainly of frequencies in the range 8 to 13 Hz, called alpha waves, but when the subject is more alert the frequencies detected in the signal rise above 13Hz, called beta waves. Measurements of the EEG during sleep have revealed periods of high frequency waves, known as rapid eye movement (REM) sleep which has been associated with dreaming [5].

MEG experiments are carried out in much the same way as their EEG counterpart. Having identified the peak of interest, the signals from all the detectors are analysed to obtain a field map. From this map an attempt can be made to ascertain the source of the signal by solving the inverse problem. Since the inverse problem has no unique solution, assumptions need to be made, but providing there are only a few activated sites, close to the scalp then relatively accurate localization is possible, giving a resolution of the order of a few millimeters.

MEG has the advantage over EEG that signal localisation is, to an extent, possible, and over PET and fMRI in that it has excellent temporal resolution of neuronal events. However MEG is costly and its ability to accurately detect events in deeper brain structures is limited.

2.3. Functional MRI and MRS

Since functional magnetic resonance imaging is the subject of this paper, little will be said in this section as to the mechanisms and applications of the technique. The purpose of this section is to compare fMRI to the other modalities already mentioned, and also to consider the related, but distinct technique of magnetic resonance spectroscopy (MRS) [5].

During an fMRI experiment, the brain of the subject is scanned repeatedly, usually using the fast imaging technique of echo planar imaging (EPI). The subject is required to carry out some task consisting of periods of activity and periods of rest. During the activity, the MR signal from the region of the brain involved in the task normally increases due to the flow of oxygenated blood into that region. Signal processing is then used to reveal these regions. The main advantage of MRI over its closest counterpart, PET, is that it requires no contrast agent to be administered, and so is considerably safer. In addition, high quality anatomical images can be obtained in the same session as the functional studies, giving greater confidence as to the source of the activation. However, the function that is mapped is based on blood flow, and it is not yet possible to directly map neuroreceptors as PET can. The technique is relatively expensive, although comparable with PET, however since many hospitals now have an MRI scanner the availability of the technique is more widespread [5].

Table 1. Comparison of modalities for studying brain function.

Technique	Resolution	Advantages	Disadvantages
SPECT	10 mm	Low cost Available	Invasive, Limited resolution
PET	5 mm	Sensitive, Good resolution, Metabolic studies, Receptor mapping	Invasive, Very expensive
EEG	poor	Very low cost, Sleep and operation monitoring	Not an imaging technique
MEG	5 mm	High temporal resolution	Very Expensive, Limited resolution for deep structures
fMRI	3 mm	Excellent resolution Non-invasive	Expensive, Limited to activation studies
MRS	low	Non-invasive metabolic studies	Expensive, Low resolution

FMRI is limited to activation studies, which it performs with good spatial resolution. If the resolution is reduced somewhat then it is also possible to carry out spectroscopy, which is chemically specific, and can follow many metabolic processes. Since fMRS can give the rate of glucose utilisation, it provides useful additional information to the blood flow and oxygenation measurements from fMRI, in the study of brain metabolism [5].

3. METABOLISM AND BLOOD FLOW IN THE BRAIN

The biochemical reactions that transmit neural information via action potentials and neurotransmitters, all require energy.

This energy is provided in the form of ATP, which in turn is produced from glucose by oxidative phosphorylation and the Kreb's cycle (**Figure 1**) [5].

As ATP is hydrolysed to ADP, energy is given up, which can be used to drive biochemical reactions that require free energy. The production of ATP from ADP by oxidative phosphorylation is governed by demand, so that the energy reserves are kept constant. That is to say, the rate of this reaction depends mainly on the level of ADP present.

This means that the rate of oxygen consumption by oxidative phosphorylation is a good measure of the rate of use of energy in that area [5].

The oxygen required by metabolism is supplied in the blood. Since oxygen is not very soluble in water, the blood contains a protein that oxygen can bind to, called haemoglobin. The important part of the haemoglobin molecule is an iron atom, bound in an organic structure, and it is this iron atom which gives blood it's colour. When an oxygen molecule binds to haemoglobin, it is said to be oxyhaemoglobin, and when no oxygen is bound it is called deoxyhaemoglobin.

To keep up with the high energy demand of the brain, oxygen delivery and blood flow to this organ is quite large. Although the brain's weight is only 2% of the body's, its oxygen consumption rate is 20% of the body's and blood flow 15%. The blood flow to the grey matter, which is a synapse rich area, is about 10 times

Figure 1. Overview of the aerobic metabolism of glucose to ATP following the Kreb's cycle.

that to the white matter per unit volume. Regulation of the regional blood flow is poorly understood, but it is known that localised neural activity results in a rapid selective increase in blood flow to that area [5].

## 4. BLOOD OXYGEN LEVEL DEPENDENT CONTRAST IN MR IMAGES

Since regional blood flow is closely related to neural activity, measurement of the rCBF is useful in studying brain function. It is possible to measure blood perfusion with MRI, using techniques similar to those mentioned. However there is another, more sensitive, contrast mechanism which depends on the blood oxygenation level, known as blood oxygen level dependent (BOLD) contrast. The mechanisms behind the BOLD contrast are still to be determined, however there are hypotheses to explain the observed signal changes.

Deoxyhaemoglobin is a paramagnetic molecule whereas oxyhaemoglobin is diamagnetic. The presence of deoxyhaemoglobin in a blood vessel causes a susceptibility difference between the vessel and its surrounding tissue.Such susceptibility differences cause dephasing of the MR proton signal [6],leading to a reduction in the value of T2*. In a T2* weighted imaging experiment,the presence of deoxyhaemoglobin in the blood vessels [7, 8]causes a darkening of the image in those voxels containing vessels. Since oxyhaemoglobin is diamagnetic and does not produce the same dephasing, changes in oxygenation of the blood can be observed as the signal changes in T2*weighted images [5].

It would be expected that upon neural activity, since oxygen consumption is increased, that the level of deoxyhaemoglobin in the blood would also increase, and the MR signal would decrease. However what is observed is an increase in signal, implying a decrease in deoxyhaemoglobin. This is because upon neural activity, as well as the slight increase in oxygen extraction from the blood, there is a much larger increase in cerebral blood flow, bringing with it more oxyhaemoglobin (**Figure 2**). Thus the bulk effect upon neural activity is a regional decrease in paramagnetic deoxyhaemoglobin, and an increase in signal [5].

The study of these mechanisms are helped by results from PET and near-infrared spectroscopy (NIRS) studies. PET has shown that changes in cerebral blood flow and cerebral blood volume upon activation, are not accompanied by any significant increase in tissue oxygen consumption [9].

NIRS can measure the changes in concentrations of oxy- and deoxyhaemoglobin, by looking at the absorbency at different frequencies. Such studies have shown an increase in oxyhaemoglobin, and a decrease deoxyhaemoglobin upon activation. An increase in the total amount of haemoglobin is also observed, reflecting the increase in blood volume upon activation [2].
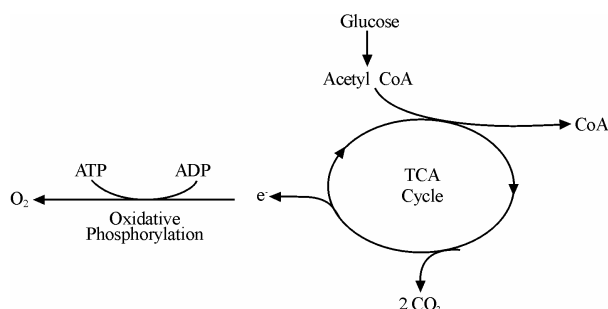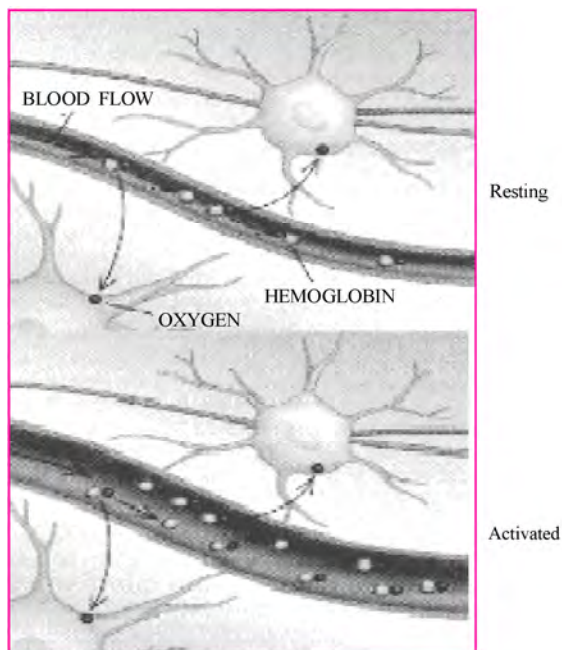
Figure 2. Upon activation, oxygen is extracted by the cells, thereby increasing the level of deoxyhaemoglobin in the blood. This is compensated for by an increase in blood flow in the vicinity of the active cells, leading to a net increase in oxy-haemoglobin.

5. CONCLUSION

Functional magnetic resonance imaging can accurately represent cerebral topography, cortical venous structures and underlying lesions. Functional activation appears to accurately localize appropriate cortical areas and these studies are feasible in the presence of local pathology. It is extremely useful in presurgical planning as well as assessment of operability. Intra-operatively, it shows a great promise in being able to define the exact location and extent of lesions with respect to surrounding functional cortex.

Functional MRI is a new and powerful neuroimaging technique that can create an anatomical and functional model of an individual patient's brain. The concurrent 3-D rendering of cerebral topography, cortical veins and related pathology gives an unprecedented display of critical relational anatomy. Since stereotaxy means simply the three dimensional arrangement of objects, then fMRI may be the ultimate stereotactic system. It allows us to see through the scalp and cortex into subcortical areas which are not visually apparent. It accurately predicts cortical gyral and venous anatomy as well as the subcortical location and extent of lesions. But most importantly, it is capable of mapping specific cortical functions to anatomical regions thereby combining form and function.

We have described the physiological bases of functional MRI and introduced a physiologically relevant model of the vascular response to fMRI. We described the major optimization goals in fMRI and several fMRI acquisition approaches. Substantial progress is being made to reduce artifacts in fMRI as well as to improve the measurement of alternate physiological phenomena using MRI.

The spatial activation pattern of changes indeoxyhemoglobin concentration is consistent with the BOLD signal map. The patterns of oxy-and deoxyhemoglobin concentrations are very similar to one another. The temporal hemodynamic response shows an increased total hemoglobin concentration, which indicates an increment of CBV during physiological activation. It has now been firmly established that magnetic resonance imaging can be used to map brain function.

The main impetus of research and development of the technique, needs to be directed in several areas if fMRI is to become more than 'colour phrenology', intriguing in its results yet having little clinical value. The mechanisms behind the BOLD effect need to be better understood, as does the physiological basis of the observed blood flow and oxygenation changes. The combination of the functional imaging modalities needs attention, since it is unlikely that any one method will provide the full picture. Finally, robust and simple techniques for data analysis need to be developed, allowing those who do not specialise in fMRI, to carry out experiments and interpret results.

REFERENCES

[1] S. S. Kety and C. F. Schmidt, (1948) The nitrous oxide method for the quantitative determination of cerebral blood flow in man: Theory, procedure and normal values, J. Clin. Invest. **27**, 476–483.

[2] H. I. Glass and A. M. Harper, (1963) Measurement of regional blood flow in cerebral cortex of man through intact skull, Br. Med. J., **1**, 593.

[3] D. E. Kuhl and R. Q. Edwards, (1963) Image separation radioisotope scanning, Radiology, **80**, 653–661.

[4] H. Berger, (1929) Über das elektrenkephalogramm des menschen, Arch. Psychiatr Nervenkr, **87**, 527–570.

[5] Veopen, (1995) Magnetic resonance imaging of brain function, Magn. Reson. Med., **22**, 149–166.

[6] K. R. Thulborn, J. C. Waterton, P. M. Matthews, and G. K. Radda, (1982) Oxygen dependence of the transverse relaxation time of water protons in whole blood at high field, Biochim. Biophys. Acta., **714**, 265–270.

[7] S. Ogawa, T. M. Lee, A. S. Nayak, and P. Glynn, (1990) Oxygenation-sensitive contrast in magnetic resonance image of rodent brain at high magnetic fields, Magn. Reson. Med., **14**, 68–78.

[8] S. Ogawa and T. M. Lee, (1990) Magnetic resonance imaging of blood vessels at high fields: In vivo and in vitro measurements and image simulation, Magn. Reson. Med., **16**, 9–18.

[9] P. T. Fox, M. E. Raichle, M. A. Mintun, and C. Dence, (1988) Nonoxidative glucose consumption during physiologic neural activity, Science, **241**, 462–464.

ECG compression and labview implementation

Tatiparti Padma[1], M. Madhavi Latha[2], Abrar Ahmed[3]

[1]GRIET, JNTU, Hyderabad, India, Member IETE; [2]JNTU, Hyderabad, India, Member IEEE; [3]GRIET, Hyderabad, India.
Email: tatipartipadma@gmail.com

ABSTRACT

It is often very difficult for the patient to tell the difference between angina symptoms and heart attack symptoms, so it is very important to recognize the signs of heart attack and immediately seek medical attention. A practical case of this type of remote consultation is examined in this paper. To deal with the huge amount of electrocardiogram (ECG) data for analysis, storage and transmission; an efficient ECG compression technique is needed to reduce the amount of data as much as possible while preserving the clinical significant signal for cardiac diagnosis. Here the ECG signal is analyzed for various parameters such as heart rate, QRS-width, etc. Then the various parameters and the compressed signal can be transmitted with less channel capacity. Comparison of various ECG compression techniques like TURNING POINT, AZTEC, CORTES, FFT and DCT it was found that DCT is the best suitable compression technique with compression ratio of about 100:1. In addition, different techniques are available for implementation of hardware components for signal pickup the virtual implementation with labview is also used for analysis of various cardiac parameters and to identify the abnormalities like Tachycardia, Bradycardia, AV Block, etc. Both hardware and virtual implementation are also detailed in this context.

Keywords: ECG Compression; Labview; Implementation

1. INTRODUCTION

An **electrocardiogram** (**ECG** or **EKG**) is a recording of the electrical activity of the heart over time produced by an **electrocardiograph**. Electrical impulses in the heart originate in the sinoatrial node and travel through the heart muscle where they impart electrical initiation of systole or contraction of the heart. The electrical waves can be measured at selectively placed electrodes (electrical contacts) on the skin. Electrodes on different sides of the heart measure the activity of different parts of the heart muscle. An ECG displays the voltage between pairs of these electrodes, and the muscle activity that they measure, from different directions, also understood as vectors. After acquiring the signal, different signal analysis techniques using MATLAB software where various abnormalities can be traced out in ECG of a particular patient. The signal is then transmitted using wireless technology using Blue-Tooth as a transmitting technique. The device operates at a range of 100−150m, a distance that is ideal for use in a hospital.

Digital analysis of electrocardiogram (ECG) signal imposes a practical requirement that digitized data be selectively compressed to minimize analysis efforts and data storage space. Therefore, it is desirable to carry out data reduction or data compression. Data reduction is achieved by discarding digitized samples that are not important for subsequent pattern analysis and rhythm interpretation. Examples of such data reduction algorithms are: AZTEC, turning point (TP). AZTEC retains only the samples for which there is sufficient amplitude change. TP retains points where the signal curves (such as at the QRS peak) and discards every alternate sample. The data reduction algorithms are empirically designed to achieve good reduction without causing significant distortion error.

Another class of algorithms compresses the data under mathematically rigorous rules, so that digitized samples are compressed and recovered under some reversible mathematical criteria operating under predefined error limits. This approach has the benefit that the original signal can be recovered by with a minimum loss of information.

Einthoven named the waves he observed on the ECG using five capital letters from the alphabet: P, Q, R, S, and T. The width of a wave on the horizontal axis represents a measure of time. The height and depth of a wave represent a measure of voltage. An upward deflection of a wave is called positive deflection and a downward deflection is called negative deflection. A typical representation of the ECG waves is presented in the following **Figure 1**.
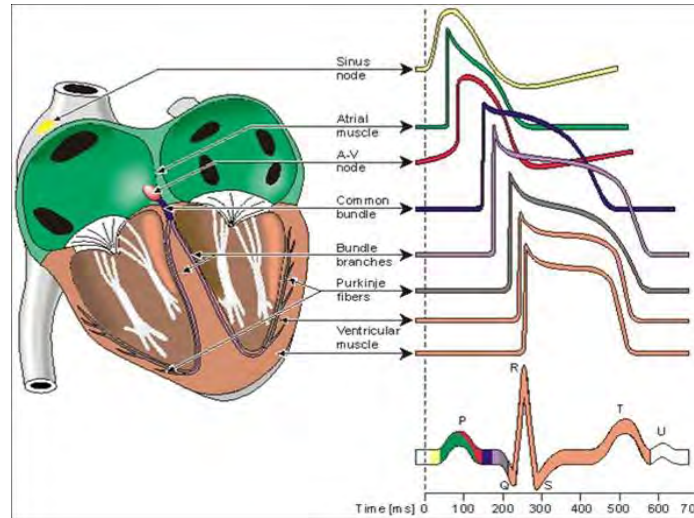
Figure 1. A typical representation of the ECG waves.

2. SYSTEM DESCRIPTION

Continuous monitoring of the electrocardiogram in both inpatients and ambulatory subjects has become a very common procedure during the past thirty years, with diverse applications ranging from screening for cardiac arrhythmias or transient ischemia, to evaluation of the efficacy of anti arrhythmic drug therapy, to surgical and critical care monitoring. The need for automated data reduction and analysis of the ECG has been apparent, motivated by the very large amount of data that must be analyzed (on the order of 10^5 cardiac cycles per patient per day). As clinical experience has led to the identification of more and more prognostic indicators in the ECG, clinicians have demanded and received increasingly sophisticated automated ECG analyzers.

Visual analysis of the ECG is far from simple. Accurate diagnosis of ECG abnormalities requires attention to subtle features of the signals, features that may appear only rarely, and which are often obscured or mimicked by noise. Diagnostic criteria are complicated by inter- and intra-patient variability of both normal and abnormal ECG features. In this paper, the attempt is made to replace the bedside monitors in the intensive care units so as to reduce the workload of the staff and increase the efficiency in interpreting the abnormalities. The basic block diagram of the module is as shown in the **Figure 2**.

The standard lead system used in intensive care units is lead II system; the acquired signal is taken and is fed to an instrumentation amplifier that amplifies the signal. The amplifier is used to set the gain and it also amplifies very low amplitude ECG signal into perceptible view.

The acquisition of pure ECG signal is of higher importance. As we know that the ECG signal will be in the range of milli-volts range, which is difficult to analyze. So the prior requirement is to amplify the acquired signal. The acquisition and amplification of ECG signal is showed in **Figure 3** using an instrumentation amplifier AD620.

The output gain can be programmed by varying the value of R_G. The amplified output is shown in **Figure 4**.
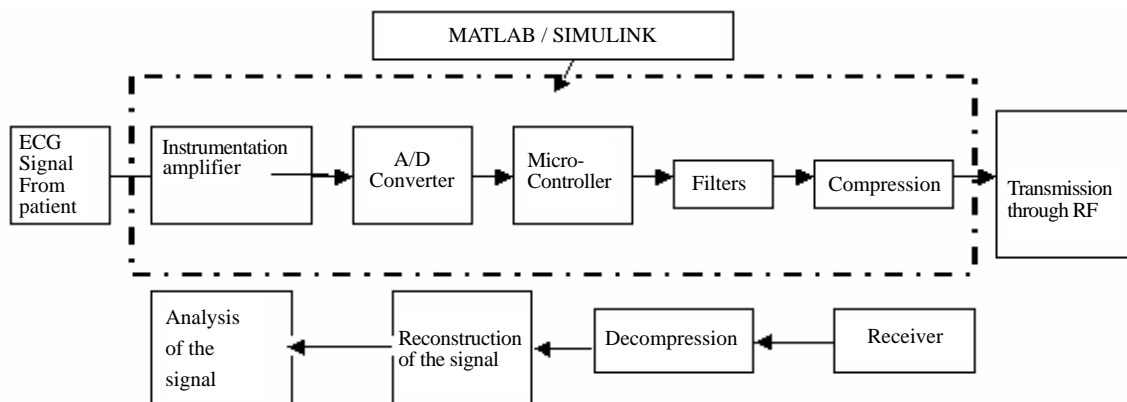
**Figure 2.** Basic block diagram of the ECG module.
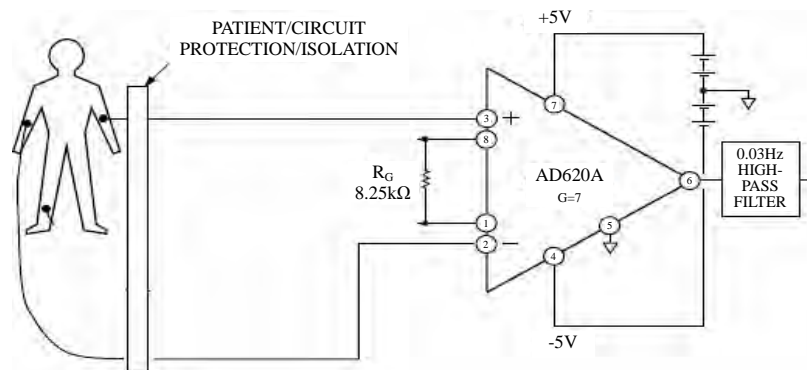
**Figure 3.** ECG acquisition with instrumentation amplifier AD620.
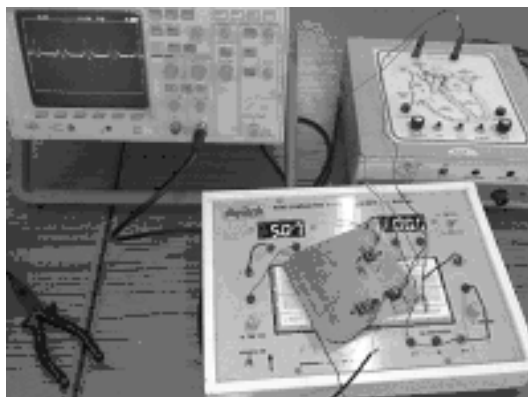
Figure 4. ECG signal output before ADC.

The amplified output is then fed to the analog to digital converter for digitalizing the ECG data using ADC and microcontroller. In this process, micro-controller is used so as to set the clocks for picking up the summation of the signals that are generated form the heart. The heart generates different signals at various nodes that is shown in **Figure 1**. The summation of the signals that are generated by the heart is taken and then it is sent for filtering processes.

The digital output of the ECG is displayed in LCD as shown in **Figure 5**.
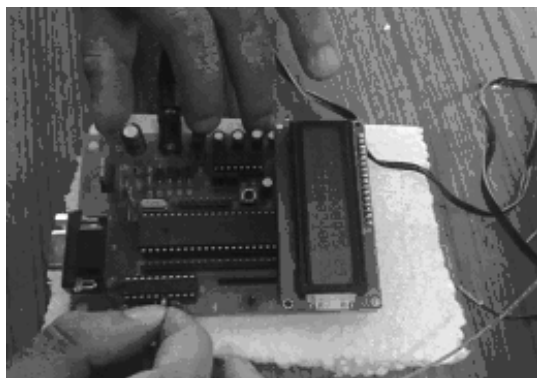
Figure 5. Digital output of the ECG is displayed in LCD.

As the ECG signal is going to be transmitted through wires to the module, it is obviously corrupted by various noises such as power line interference, muscle tremors etc. Hence various filtering techniques are applied to remove the noise and to send the error/noise free signal for further processing. Here adaptive noise filtering is used for removal of 50 Hz that is the power line inter-ference because, the ECG signal also contains 50 Hz signal and if normal band reject filter is used, then the 50 Hz signal which is very important in the ECG signal will be lost. Therefore by opting adaptive noise filtering, the power line frequency can be eliminated at the same time retaining the 50 Hz signal in the original waveform.

After the filtering process, the signal is set for the transmission, but it is important to compress it so as to transmit at a faster rate. In this paper compared various basic compression techniques like Turning point, AZTEC, CORTES and found that CORTES is the better option for the compression of ECG signal as it compresses the signal at a rate of around 100:1. Before transmitting the compressed data, the ECG signal is analyzed.

3. ECG ANALYSIS

The processing and the analysis of the ECG has gained clinical significance. The various cardiac parameters are heart rate, R-R interval, QRS duration; etc can be obtained at any instance of time or continuously depending upon the requirement. The better analysis of the ECG can help doctors to give the appropriate care to the patients and also helps to avoid various severe situations that may arise. Here the ECG signal is analyzed and the result has been displayed as shown in **Figure 6**.

After analysis of ECG signal, it can be compressed using various techniques and hence transmit the compressed data to the main system. The various compression techniques have been explained below.

4. COMPRESSION TECHNIQUES

The various compression techniques like AZTEC, TP, CORTES, DFT, FFT algorithms are compared with PRD and Compression ratio and best suitable was considered.
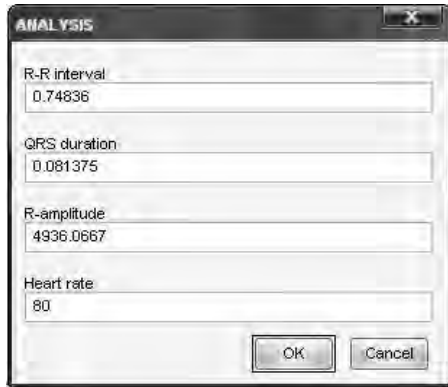
Figure 6. ECG analysis output.

4.1. Turning Point Algorithm

1) Acquire the ECG signal

2) Take the first three samples and check for the condition as mentioned below:

$$(x_1-x_0)*(x_2-x_1)<0$$
$$(or)$$
$$(x_1-x_0)*(x_2-x_1)>0$$

3) If the above condition-1 is correct then x_1 is stored else x_2 is stored.

4) Reconstructing the compressed signal.

The compression ratio of Turning point algorithm is 2:1, if higher compression is required then the same algorithm can be implemented on the already compressed signal so that it is further compressed to a ratio of 4:1. But after the 2nd compression, the required data in the signal may be lost since the signal is overlapped on one another. Therefore, TP algorithm is limited to compression ratio of 2:1. TP algorithm can be applied on the already compressed data to increase the compression ratio to 4:1. As shown in **Figure 7**.

4.2. AZTEC ALGORITHM

Another commonly used technique is known as AZTEC (Amplitude Zone Time Epoch Coding). This converts the ECG waveform into plateaus (flat line segments) and sloping lines. As there may be two consecutive plateaus at different heights, the reconstructed waveform shows discontinuities. Even though the AZTEC provides a high data reduction ratio, the fidelity of the reconstructed signal is not acceptable to the cardiologist because of the discontinuity (step-like quantization) that occurs in the reconstructed ECG waveform. As shown in **Figure 8**.

AZTEC Algorithm is implemented in 2 phases:

4.2.1. Horizontal Mode

1) Acquire the ECG signal

2) Assign the first sample to X_{max} and X_{min} which represents highest and lowest elevations of the current line.

3) Check for the following condition and store the plateau if

  a) If $X_1>X_{max}$ then $X_{max}=X_1$ and

  b) If $X_1<X_{min}$ then $X_{min}=X_1$ and so on till X_n samples, repeat this until the following 2 conditions are satisfied

    ① the difference between VMAX and VMIN is greater than a predetermined threshold or

    ② if line length is > 50 are satisfied

4) The stored values are the length L=S-1, where S is no. of samples and L is length and the average amplitude of the plateau (VMAX+VMIN)/2.

5) Algorithm starts assigning the next samples to X_{max} and $X_{min.}$

4.2.2. Slope Mode

1) If no. of samples <=3, then the line parameters are not saved. Instead the algorithm begins to produce slopes.

Figure 7. Turning point compression analysis.
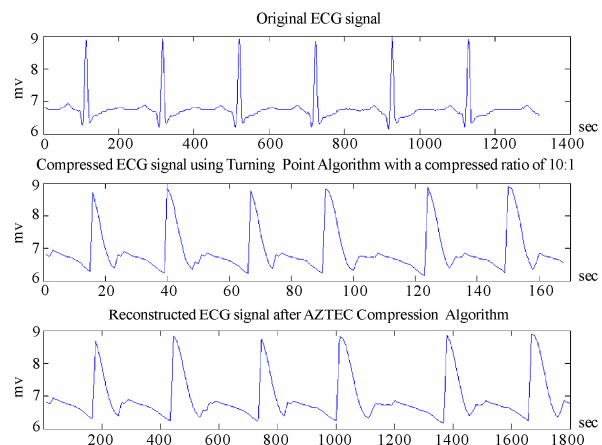
Figure 8. AZTEC compression analysis.

2) The direction of the slope is determined by checking the following conditions.

a) If $(X_2 - X_1) * (X_1 - X_0)$ is +ve then the slope is +ve.

b) If $(X_2 - X_1) * (X_1 - X_0)$ is -ve then the slope is -ve.

3) The slope is terminated if the no. of samples is >=3 and if direction of slope is changed.

4.3. CORTES Algorithm

An enhanced method known as CORTES (Coordinate Reduction Time Encoding System) applies TP to some portions of the waveform and AZTEC to other portions and does not suffer from discontinuities. AZTEC line length threshold Lth, CORTES saves the AZTEC line otherwise it saves the TP data. As shown in **Figure 9**.

1) Acquire the ECG signal

2) Define the Vth and Lth.

3) Find the current Maximum and minimum.

4) If the Sample greater than threshold than   compare the length with Lth

5) If (len>lth)
   AZTEC   Else
   TP

6) Plot the compressed signal

4.4. DCT Compression

1) Separate the ECG components into three components x, y, z.

2) Find the frequency and time between two samples.

3) Find the dct of ecg signal check for dct coefficients (before compression)=0, increment the counter A if it is between +0.22 to -0.22 and assign to Index=0.

4) Check for DCT coefficients(after compression)=0, increment the Counter B.

5) Calculate inverse dct and plot decompression, error.

6) Calculate the compression ratio, PRD.

As shown in **Figure 10**.

4.5. FFT Compression

1) Separate the ECG components into three components x, y, z.
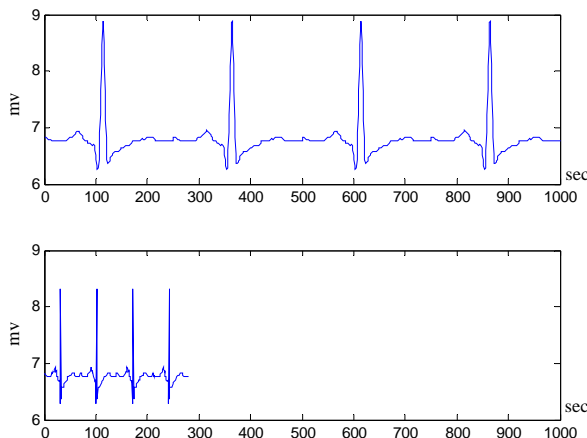
Figure 9. CORTES compression analysis.
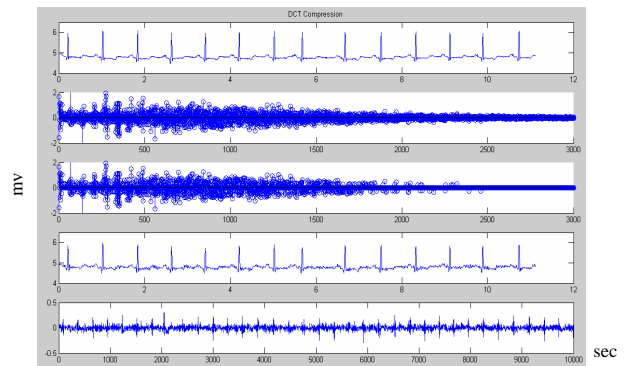
Figure 10. DCT compression analysis.
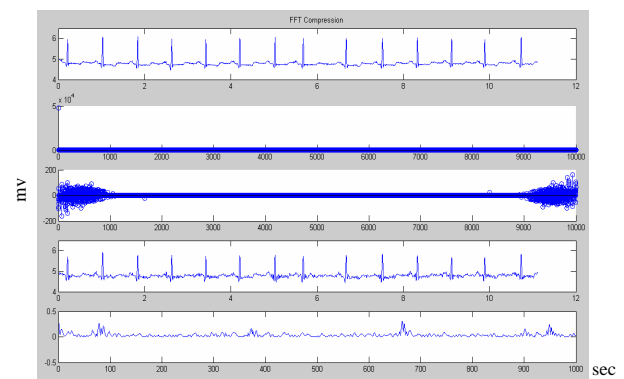
Figure 11. FFT compression analysis.

2) Find the frequency and time between two samples.

3) Find the FFT of ECG signal check for fft coefficients (before compression) =0, increment the counter A if it is between +25 to-25 and assign to Index=0.

4) Check for FFT coefficients (after compression) =0, increment the Counter B.

5) Calculate inverse FFT and plot decompression, error.

6) Calculate the compression ratio, PRD.

As shown in **Figure 11**.

4.6. Summary

Summary of ECG data compression schemes.

The comparison table shown in **Table 1** above, details the resultant compression techniques. This gives the choice to select the best suitable compression method. Hence in this project the DCT found to be compressed 90.43 with PRD as 0.93.

Table 1. Comparison of compression techniques.

METHOD	COMPRESSION RATIO	PRD
CORTES	4.8	3.75
TURNING POINT	5	3.20
AZTEC	10.37	2.42
FFT	89.57	1.16
DCT	90.43	0.93

5. HARDWARE IMPLEMENTATION

The hardware implementation part is rather large and complex and the present trend in the BIOMEDICAL field is moving towards the miniaturization, thereby an efficient design flow is necessary, which was implemented using LABVIEW as shown in **Figure 12**.

The ECG signal is acquired with the help of electrodes that are connected to the patient and the signal is fed for further processing like instrumentation amplifier, Analog to Digital converter, micro controller, and filters. After acquiring the signal, different signal analysis techniques using LABVIEW software where various abnormalities are to be checked for and finally display the problem in ECG of a particular patient.

The standard lead system used in intensive care units is lead II system. (ECG data was acquired from a data file MIT-BIH (.m file)).

The signal is taken and fed to an instrumentation amplifier that amplifies the signal. The amplifier is used to set the gain and it also amplifies very low amplitude ECG signal into perceptible view. Then the signal goes for analog to digital conversion for the sake of easier transmission. The amplified signals are then sent for filtering processes.

The adaptive noise filtering is used for removal of 50 Hz that is the power line interference because, the ECG signal also contains 50 Hz signal and if normal band reject filter is used, then the 50 Hz signal which is very important in the ECG signal will be lost. Therefore by opting adaptive noise filtering, the power line frequency can be eliminated at the same time retaining the 50 Hz signal in the original waveform.

6. RESULTS

Extracting the portion of the signal and finding the R peaks in the signal by a first difference method. Once the R peaks are identified the heart rate is calculated the by knowing the period between successive R-peaks.

$$Y(n) = \frac{x(n+1) - x(n)}{T} \text{; where T is sampling period.}$$

Heart rate Calculation:

$$HR = \frac{60}{Y(n)} == \underline{\hspace{1cm}} \text{ BPM.}$$

7. CONCLUSIONS

The feeling of being in virtual contact with the health care professionals provides a sense of safety to the subjects, without the hassles of permanent monitoring.

Offers a valuable tool for easy measurement of ECG.

Offers first hand help when ever patient requires immediate medical attention.
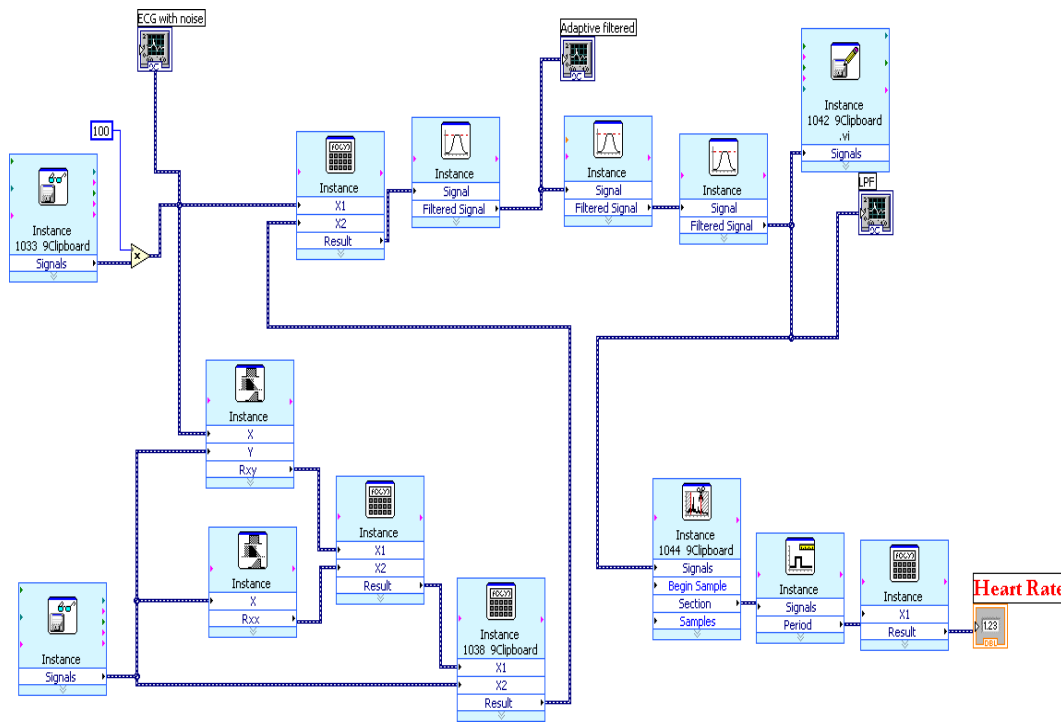
Figure 12. QRS detection & heart rate calculation module.
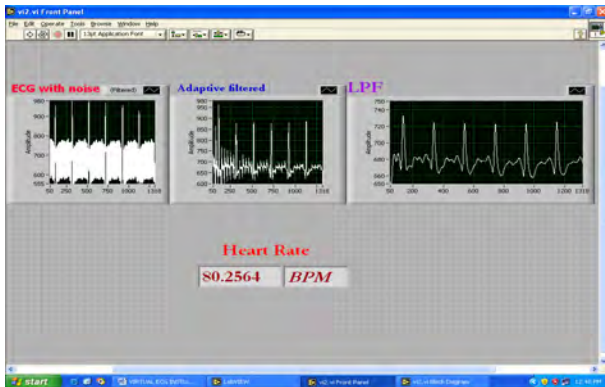
Figure 13. Heart rate display.

The results achieved were quite satisfactory the DCT found to be compressed 90.43 with PRD as 0.93. The signal analysis techniques using LABVIEW software where various abnormalities are to be checked for and finally display the problem in ECG of a particular patient was also given a positive indication, with this as the goal set the further implementation in matlab simulink work is also under the implementation stage.

REFERENCES

[1] S. Jalaleddine, C. Hutchens, R. Stratan, and W. A. Coberly, (1990) ECG data compression techniques-a unified approach, IEEE Trans. Biomed. Eng., **37**, 329−343.

[2] J. R. Cox, F. M. Nolle, H. A. Fozzard, and G. C. Oliver, (1968) AZTEC, a preprocessing program for real time ECG rhythm analysis, IEEE Trans. Biomed. Eng., BME-**15**, 129−129.

[3] B. R. S. Reddy and I. S. N. Murthy, (1986) ECG data compression using fourier descriptors, IEEE Trans. Biomed. Eng., BME-**33**, 428−433.

[4] D. C. Reddy, (2007) Biomedical signal processing-principles and techniques, 254−300, Tata McGraw-Hill, Third reprint.

[5] J. L. Simmlow, Biosignal and biomedical image processing- MATLAB based applications, 4−29.

[6] A. S. Al-Fahoum, (2006) Quality assessment of ECG compression techniques using a wavelet-based diagnostic measure, IEEE Trans. in Biomedicine, **10**, 182−191.

[7] V. Kumar, S. C. Saxena, and V. K. Giri, (2006) Direct data compression of ECG signal for telemedicine, ICSS , **10**, 45−63.

[8] A. Perkusich, G. S. Deep, M. L. B. Perkusich, and M. L. Varani, (1989) An expert ECG acquisition and analysis system, IMTC- **89**, 184−189.

Identifying species-specific subsequences in bacteria transcription terminators-A machine learning approach

Bao-Hua Gu[1], Yi Sun[1]

[1]School of Computing Science, Simon Fraser University, 8888 University Drive, Burnaby, BC, Canada.
Email: {bgu, sunyi}@cs.sfu.ca

ABSTRACT

Transcription Terminators (TTs) play an important role in bacterial RNA transcription. Some bacteria are known to have Species-Specific Subsequences (SSS) in their TTs, which are believed containing useful clues to bacterial evolution. The SSS can be identified using biological methods which, however, tend to be costly and time-consuming due to the vast number of subsequences to experiment on. In this paper, we study the problem from a computational perspective and propose a computing method to identify the SSS. Given DNA sequences of a target species, some of which are known to contain a TT while others not, our method uses machine learning techniques and is done in three steps. First, we find all frequent subsequences from the given sequences, and show that this can be efficiently done using generalized suffix trees. Second, we use these subsequences as features to characterize the original DNA sequences and train a classification model using Support Vector Machines (SVM), one of the currently most effective machine learning techniques. Using the parameters of the resulting SVM model, we define a measure called subsequence specificity to rank the frequent subsequences, and output the one with the highest rank as the SSS. Our experiments show that the SSS found by the proposed method are very close to those determined by biological experiments. This suggests that our method, though purely computational, can help efficiently locate the SSS by effectively narrowing down the search space.

1. INTRODUCTION

Bacterial genomes are organized into units of expression that are bounded by sites where transcription of DNA into RNA is initiated and terminated. The former site is called *Transcription Promoter*, which determine what region and which strand of DNA will be transcribed into RNA. The later site is called *Transcription Terminator* (TT), which is a stop signal to terminate the transcription process [1].

Although the mechanism of transcription termination in bacteria is *rho-independent*, or intrinsic, the TTs in different bacteria have a common hairpin-like RNA structure as shown in **Figure 1**: typically a stem-loop structure with dyadic stempairing high in guanine (G) and cytosine (C) residue content, followed by a uracil-rich (U) stretch of sequence proximal to the termination site [2].

This particular RNA structure is encoded in the certain region of the corresponding DNA sequence. It is well known that the DNA sequences of some bacteria have species-specific subsequences (SSS) for the TTs. That is, the subsequence appears significantly more frequently in certain species than in others. For example, for bacterium *Neisseria Meningitidis*, the SSS is *GCCGTCTGAA*, while for bacterium Haemophilus Influenzae, the SSS is *AAGTGCGGT* [3]. Having found many DNA sequences of TTs of many bacteria, biologists are wondering whether these bacteria also have such SSS. The biological motivation behind is that the SSS might provide better understanding of the terminator evolution and how it functions in genetic exchange between pathogens.

Of course, the SSS can be determined by biological experiments. However, such experiments tend to be costly and time-consuming because every subsequence has to be examined and the number of such subsequences can be prohibitively large due to the length of the DNA sequences. To overcome the difficulty, biologists typically apply domain knowledge to narrow down the search space. However, the process of obtaining such knowledge itself would also be time-consuming and highly expensive if they are not available yet. Therefore, it is desirable to study alternative ways to effectively identify the SSS from the given DNA TT sequences.
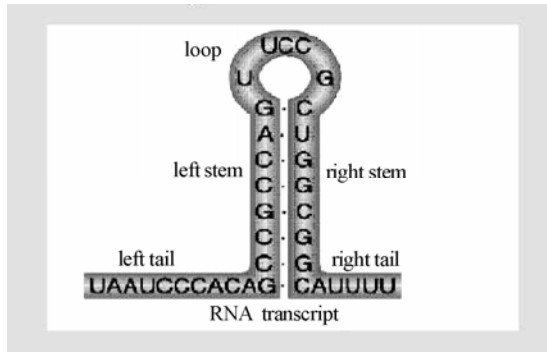
Figure 1. The stem-loop structure of bacteria transcription terminators.

In this paper we consider the problem from computational perspective. We apply machine learning techniques and propose a method to compute the SSS. Our method has three steps. In the first step, we finds out all frequent subsequences that occur more than a given threshold (or minimum support) by using generalized suffix tree. In the second step, we take the frequent subsequences as features to vectorize the DNA sequences and train an SVM classifier. In the third step, we define a measure of *subsequence specificity* and output the most significant features based on the measure as the SSS. Our experimental results show that the SSS found by our method are very close to the known SSS for some well known bacteria. This demonstrates that the proposed method is effective in identifying the SSS.

Our main contribution here is to introduce a machine learning approach to identifying the SSS.

We have seen successful applications of machine learning and data mining approaches to other biological problems. However, to our best knowledge, this work is the first that applies machine learning techniques to this problem. An advantage of our method is that it does not require biological domain knowledge although such knowledge would further improve the accuracy. Besides, our method does not make any assumption specific to this particular problem, and thus is potentially applicable to other similar problems.

Moreover, we also contribute to computing community by trying out new ways of using classification techniques. Traditionally, a classifier is used to predict class labels for future unseen examples. But in this paper, we use the classifier in two new ways: the tested precision of the trained classification model is used to judge whether there would be any SSS, and if so the feature weights contained in the model are used to rank the features in the model. In a word, our method can be considered as a novel application of classification to computational biology.

The rest of this paper is organized as follows: Section 2 discusses related research. The detail of the proposed method is presented in Section 3. Section 4 describes the

experimental method, results and discussions. Section 5 summarizes this paper and points out our future work.

2. RELATED WORK

Given a bacteria DNA sequence, how to locate the segment corresponding to the RNA structure of TTs has been well studied in molecular biology and biochemistry. Interested readers are referred to [2] for research in this area. In this paper, we are dealing with a different problem: given DNA sequences that encode TTs of certain bacterium, find out whether there would be any subsequence specific to this bacterium and if so what it is. As far as we know, this problem has not been well studied in the literature of machine learning and data mining.

Support Vector Machines (SVM) has been widely studied and applied in machine leaning [4] and data mining [5] since introduced by [6]. In recent years, it has been applied to solve classification problems in bio-computing. For example, it has been used in predicting outer membrane proteins of bacteria in [7] and remote protein homology detection in [2].

We notice that in these applications, SVM lassifiers are mainly used in a traditional way, in which the classifier is built from training sequences and then applied to predicting the class labels of future unseen sequences. In our method, the classifier is used in a very different way: we use it as an indicator of whether there exist features sufficiently specific to distinguish the positive class from the negative class. If the precision of the classifier is much higher than the odds of making a random guess, we think this classification is good and reliable. Then we let the classifier to tell us which features are more important to the classification, based on which we then define the subsequence specificity measure to rank the subsequences. The most significant ones are reported as the SSS.

In our method, the DNA sequences have to be converted into vectors in the feature space solvable by SVM. The conversion is done by taking all frequent subsequences (frequent in terms of a predefined minimum number of occurrences) found in DNA sequences as features in the SVM feature space. This sort of conversion is not new, and has proved to be a very effective way to express genome/protein sequences for classification, because it is able to capture the sequential relations of the genome/protein sequences [7,8]. The frequent subsequences can be efficiently found by using generalized suffix trees.

Suffix tree is a very useful data structure for string matching problem, and has been well studied and widely applied. Interested reader are referred to [9] for more details.

3. THE PROPOSED METHOD

Basically, we treat the target problem of finding SSS as a classification problem. The intuition is that if there exists

any subsequence specific to one species, then we should be able to build a good classifier to separate this species from others. Such a classifier should have contained the SSS as features. As SVM has the state-of-the-art performance for classification, we will train the classifiers using SVM.

In general, our method can be divided into three steps. In the first step, it finds out all frequent subsequences that occur more than a given threshold (called minimum support) by using generalized suffix trees. Second, it takes the frequent subsequences as features to vectorize the original DNA sequences for building the SVM classifier. If the precision of the classifier is higher than the odds of making a random guess, we think this is a good classification. Then we define a measure of subsequence specificity and output the most significant features based on the measure. We will describe each step in more detail in the following subsections.

3.1 Frequent Subsequences Generation

Note that SVM requires the input data to be vectorized. In this paper, the training examples are given in the form of DNA sequences, which are basically strings of letter A, C, G and T, representing the four basic amino acids of DNA. In order to convert a DNA sequence into a vector format, we need a feature space. Here we use the frequent subsequences to be the features, by which the original sequence are transformed. We hope that the subsequences can keep sufficient sequential information about the original DNA sequences.

Here is a toy example: Given 3 DNA sequences, S1 = ACGT, S2 = CGTA, S3 = GTAC. If the minimum support=2 (i.e., a subsequences must appear at least twice to be considered as frequent), then the frequent subsequences are {A,C, G, T,CG,GT,AC}.

It is a nontrivial task to find all frequent subsequences from thousands of DNA sequences, each of which may contain more than hundreds of letters, because the total number of frequent subsequences could be very large. Although any methods that can output frequent subsequences from the original sequences would work as long as they are computationally feasible. To make it efficient, we make use of generalized suffix tree [9]. Suffix tree has proved to be an effective data structure for finding common substrings in linear time and linear space in terms of the total number of letters in the given string. While a generic suffix tree is built for only one string, it can be easily generalized to contain multiple strings. The generalized suffix tree provides an efficient way to finding frequent subsequences in multiple DNA sequences. Interested readers are referred to the abovementioned references for details on (generalized) suffix tree algorithms.

3.2 DNA Sequences Vectorization

Having obtained frequent subsequences, we take each

subsequences as a feature in the feature space, and convert an original DNA sequence into a vector of the feature space.

Readers familiar with text categorization may draw an analogy from this step to the text representation, by viewing a DNA sequence as a document and a frequent subsequence as a word. Similar to text categorization, we can have different codings to represent a DNA sequence using the frequent subsequences. In our later experiments, we mainly use the binary coding: if a sequence contains a subsequences feature, it is given value "1" on that feature, otherwise, the feature value is "0". This expression, though simple, proves to be very effective. It is also possible to use other expression such as TFIDF [10].

Here is a toy example (continued): following the above toy example, the three sequences can be vectorized using the binary coding. Let the feature space be the frequent subsequences set {A,C, G, T,AC,CG,GT}, the sequence S1 = ACGT is converted to vector (1,1,1,1,1,1, 1), S2 = CGTA becomes (1,1,1,1,0,1,1), and the sequence S3 = GTAC becomes (1,1,1,1,1,0,1).

3.3 SVM Classification

SVM is based on the structural risk minimization principle from statistical learning theory introduced by V. Vapnik [6].

In its basic form, SVM learns linear decision hyperplane $h(\vec{x}) = sign\{\vec{w} \cdot \vec{x} + b\}$, described by a weight vector $\vec{w}$ and a threshold b. The input is a set of n training example $S_n = ((\vec{x_1}, y_1), \cdots, (\vec{x_n}, y_n)) \in R^N, \quad y_i \in \{+1, -1\}$. For a linearly separable Sn, the SVM finds the hyperplane with maximum Euclidean distance to the closest training examples. This distance is called the margin δ, as depicted in **Figure 2**. For a nonlinearly separable Sn, the SVM uses either a kernel function to map the original data into another dimensional space where the data points are linearly separable, or a hyperplane with a soft margin the allows some degree of training error in order to obtain a large margin. Computing the hyperplane is
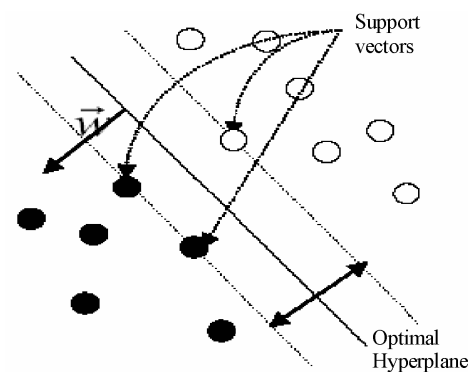

Figure 2. A linear SVM for a two dimensional training set.

equivalent to solving an optimization problem. The resulting model is actually the decision hyperplane, expressed by $\vec{w}$ and b.

Note that the resulting weights can be actually viewed as a ranking of the features: a positive (negative) weight means the corresponding feature values contribute to the positive (negative) class; the larger the absolute weight value, the more important the feature is to the classification; weights of zero or very small values have little contribution to classification. Later we will use this ranking information to define what we call the measure of subsequence specificity.

We decide to use SVM for classification because it has proved to have a number of advantages over other classification algorithms. First, it can easily handle very high dimensional input space [11]. Second, it works well when the problem contain few irrelevant features [11]. Third, it does not require feature selection as a preprocessing step, because it can automatically ignore irrelevant features during the optimization [11]. Fourth, the weights contained in the resulting SVM model can be used to rank the features. All these are essential to solving the target problem.

In this paper, we use the popular SVM-light implementation of SVM [12]. Note that when training SVM classifier, one can select a kernel function suitable for the studied problem. Motivated by the fact that text documents are in general linearly separable [11], in our later experiments we only consider linear SVM model which is used by default in SVMlight.

3.4 Measure of Good Classifiers

Usually the performance of a classifier is measured by classification accuracy, precision and/or recall. They are defined based on a confusion matrix as shown in Table I. The Precision of the positive class is defined as P= TP=(TP+FP), while the Recall of the positive class is defined as R=TP/(TP+FN). The overall Accuracy is defines as A=(TP+TN)/(TP+FP+TN+FN). In our method, the performance of SVM classifier is not measured by the overall accuracy, because negative training sequences would be much more than those positives, and the overall accuracy would be heavily affected by the overwhelming negatives.

Besides, as our goal is to identify the specific subsequences in positive species, we hope to maximize the precision (i.e., the probability of the classifier making a correct prediction is high). Therefore, we will only use precision as the measure of classifier's performance. At the same time, we will report corresponding recalls for reference. Note that the precision of the classifier should be higher than the odds that one makes a random guess for the positive class label, in order to be considered as a good classification. Otherwise, the classifier does not make sense. For example, if a training data set contains

Table 1. Confusion matrix in classification.

	Actual number of positive examples	Actual number of negative examples
Number of examples classified as positive	True Positive (TP)	False Positive (FP)
Number of examples classified as negative	False Negative (FN)	True Negative (TN)

100 positive examples and 100 negative examples, if one randomly guesses for the class label of any of the 200 examples, the probability of making a correct guess is obviously 50%. If a classifier than a random guess, then the classifier is useless. A bad classification may suggest that the information contains in the training examples is probably insufficient for the classifier to distinguish the positive examples from the negative examples.

In our method, we take this as an indication that the positive species probably contains no SSS. In other words, we consider a classifier is good only when its precision is much higher than the random guess odds. In our later experiments, the precision is obtained by testing against a reserved portion of the total data, which is unseen during the classifier is trained.

3.5 Subsequence Specificity Measure

Note that the resulting classifier will not be used as usual to predict class label for an unseen sequence. Remember the task here is to identify the SSS. For this purpose, we make use of the weights of features in the SVM model, to define what we call subsequence specificity to measure how specific a subsequence f is to the positive species as follows:

$$spec(f)=svm\_weight(f)\times support(f,+)$$
$$\times confidence(f,+).$$

here weight (f) is the weight of feature f obtainable from the learned SVM model, support (f,+) is a measure of how many sequences of positive species contain f, and confidence(f,+) is a measure of how many sequences that contain f belong to positive species.

The definition of the subsequence specificity is based on the following observations and expectations:

1) An SSS should occur frequently in the positive species. This means it should have a high support.

2) An SSS should occur more frequently in the positive species than in the negative species. This means it should have a high confidence.

3) Having a high support and/or a high confidence does not necessarily mean a high distinguishing power, while this can be reliably judged by the feature weights in SVM model.

4) SVM may give more weight on features having low support and/or confidence. This means the weights alone are insufficient to measure the specificity.

5) Each of the three quantities alone characterizes the subsequence specificity from an unique angle. Combing

them together should be able to give a more accurate characterization of the specificity, and thus is expected to be a more reliable measure.

4. EVALUATION

4.1 The Data Set

The data set used in this project is provided by the Brinkman Libratory of SFU Molecular Biology and Biochemistry Department. It contains known rho-independent transcription terminator sequences for 42 bacteria genomes. The source of the data set is The Institute for Genomic Research (TIGR). Each record of the data set contains one terminator sequence (including left tail, stem and loop, and right tail) and the taxonomy id of the corresponding bacterium. The total number sequences is 12763, and 18 species have less than 100 terminator sequences.

Besides, we are also provided with a file containing the taxonomy information of all bacteria species. Figure 3 shows the taxonomy tree for the 42 bacteria, obtained from the file. The tree shows the evolution paths for the 42 bacteria. Each node in the tree represents a bacterium species, and marked by its taxonomy id. The leaf nodes are enclosed by a parenthesis. Note that among the 42 bacteria, 41 are at leaf nodes, except species 562, which has species 83334 as its children. This is the only pair of species that has a direct parent-children relationship in the given data set.

The task is to identify those DNA subsequences that are specific to certain species. The hope is that this should provide a better understanding of bacteria evolution and how it plays a role in genetic exchange between pathogens. Note that for a given species, it does not necessarily have any subsequences specific to it. Also, when talking about the specificity, one should consider the corresponding scope. That is, with respect to which species a subsequence is considered specific. For example, a subsequence can be specific to bacterium A with respect to another bacterium B. Also, the subsequence can be specific to bacterium A with respect to all other bacteria.

Among the 42 species, we evaluate our methods on four bacteria whose SSS for the TTs are already known biologically. The four species are: Haemophilus influenzae, Neisseria meningitidis, Pasteurella multocida, and Pseudomonas aeruginosa [3]. As the SSS for the four bacteria are all found in the left inverted repeat (i.e., the left stem) of corresponding TTs, we will also use the left stem of each TT sequence to find the SSS. For each of the four species, we employ the one-against-all-others approach to build classifier by taking all its TT sequences (the left stems) as positive sequences while those of the other 41 species as negative sequences.

4.2. Experimental Methodology

All experiments are done using 5-fold cross validation. Averaged values over the five round experiments are reported. The linear classifiers are trained using SVM-light default settings. The frequent subsequences are obtained from the positive training sequences by setting the minimum support to be 1% of the total number of positive sequences (and the absolute support number no less than 2). These frequent subsequences represent statistically significant features with regard to the positive species, while resulting in substantially lower dimensions compared to the feature space of all potential subsequences. The classification performance is evaluated by the precisions, while the corresponding recalls are reported for reference.

4.3 Experimental Results

The results are given in Table II, from which we can see that the precisions for all the four species are significantly higher than the respective random guess odds. This implies that there are subsequence features that can distinguish the positive species from all the others. We then output the top 10 subsequences based on the subsequence specificity measure. The results are given in **Table 2**. In **Table 3**, the resulting subsequences that are the closest to the known SSS are underlined.

We can see that for species Pasteurella multocida and Pseudomonas aeruginosa, the underlined subsequences are exactly the same as the known SSS. For the Haemophilus influenzae and Neisseria memingitidis, our results are very close to the known SSS: the underlined ones are very close to the known SSS. In all cases, our top 10 subsequences are almost the substrings of the known SSS. This shows that our method is rather effective in finding SSSs. Note that the known SSS are found by applying biological domain knowledge [3], for example, discarding those biologically meaningless subsequences and/or limiting the length of the subsequences, which is not considered in our method. Therefore, it can be expected that our method can be improved by incorporating domain knowledge.

Table 2. Classification performance for the four bacteria.

Name of the Positive Species	# of Freq Subseq	Classifier Precision	Classifier Recall	Odds of Random Guess
Haemophilus influenzae	325	55.81%	14.18%	3.19%
Neisseria meningitidis	360	99.61%	50.67%	3.62%
Pasteurella multocida	389	48.0%	1.09%	3.73%
Pseudomonas aeruginosa	296	67.77%	9.34%	4.28%

Table 3. The top 10 subsequences with the greatest specificity values for the four species.

Top spec rank	The Subsequences found for each Bacterium			
	Haemophilus Influenzae	Neisseria meningitidis	Pasteurella multocida	Pseudomonas aeruginosa
1	TGCGGT	GCCGTC	TGCGGTC	*GCCCCGC*
2	*GTGCGGT*	CGTCTG	GTGCGGTC	CCCCGC
3	GTGCGG	CGTCTGA	ACCGCAC	GCCCCG
4	CGCACTT	CGTCTGAA	CCGCAC	CCCGC
5	CCGCACT	GCCGTCT	TGCGGT	GCCCC
6	CCGCACTT	CCGTCTG	*GTGCGGT*	CCCGGC
7	GCGGT	CCGTCTGA	GCGGTC	GCCC
8	CGCACT	CGTCT	GGCGAA	GCC
9	TGCGG	*CCGTCTGAA*	ACCGCA	GGCGACC
10	TGCGGTT	GTCTGA	CGGTC	GGC
actual SSS	AAGTGCGGT	GCCGTCTGAA	GTGCGGT	GCCCCGC

5. CONCLUSION

In this paper, our goal is to find the species-specific subsequences for bacteria transcription terminators. By treating the problem as a classification problem, we propose a solution based on frequent subsequences and Support Vector Machines. We first find frequent subsequences from the terminator DNA sequences of the positive species. We then take all such subsequences as feature space to transform the original DNA sequences into SVM readable vectors and train SVM classifiers. The resulting classifiers are used indicators of the existence of the SSSs. In order to extract the target subsequences from the SVM model, we make use of the SVM weights on the features and define a measure called subsequence specificity. The most significant features based on the measure are output as the SSS. Our experiments show that this method is effective. As a conclusion, we have presented a novel application of classification to computational biology.

Although the proposed method is designed and evaluated on DNA terminator sequences of bacteria, we believe that it is applicable to other similar biology tasks with perhaps minor modifications. As for future work, it is desirable to evaluate the proposed method on more bacteria. Besides, the proposed method itself can be improved in many ways. For example, to refine the specificity measure to make it more accurate, and to find better methods to express DNA sequences for classification.

REFERENCES

[1] P. Turner, (2000) Molecular Biology.

[2] M. D. Ermolaeva, H. G. Khalak, O. White, H. O. Smith, and S. L. Salzberg, (2000) Prediction of transcription terminators in bacterial genomes, Journal of Molecular Biology, **301**, 27–33.

[3] T. Davidsen, E. A. Rodland, K. Lagesen, E. Seeberg, and T. Rognes, (2004) Biased distribution of dna uptake sequences towards genome maintenance genes, Nucleic Acids Research, **32(3)**, 1050–1058.

[4] C. J. C. Burges, (1998) A tutorial on support vector machines for pattern recognition, Knowledge Discovery and Data Mining, **2(2)**.

[5] T. Joachims, (2002) Optimizing search engines using clickthrough data, in Proceedings of the ACM Conference on Knowledge Discovery and Data Mining (KDD-2002).

[6] V. Vapnik, (1995) The Nature of Statistical Learning Theory. Springer.

[7] S. Rong, F. Chen, K. Wang, M. Ester, J. L. Gardy, and F. S. L. Brinkman, (2003) Frequent-subsequence-based prediction of outer membrane proteins, in Proceedings of 2003 ACM SIGKDD Conference.

[8] M. Deshpande and G. Karypis, (2002) Evaluation of techniques for classifying biological sequences, in Proceedings of Pacific Asia Conference on Knowledge Discovery and Data Mining (PAKDD-2002).

[9] D. Gusfield, (1997) Algorithms on strings, trees, and sequences: computer science and computational biology, Cambridge University Press.

[10] G. Salton and C. Buckley, Term weighting approaches in automatic text retrieval, Information Processing and Management, **24(5)**, 1988.

[11] T. Joachims, (1998) Text categorization with support vector machines: Learning with many relevant features, in Proceedings of the European Conference on Machine Learning (ECML-1998).

[12] (2002) Svmlight support vector machine, web.

[13] B. Gu, (2007) Discovering species-specific transcription terminators for bacteria, School of Computing Science, Simon Fraser University, Tech. Rep.

[14] J. R. Quinlan, (1993) C4.5: Programs for machine learning, Morgan Kaufmann Publisher.

[15] L. Breiman, J. H. Friedman, R. A. Olshen, and C. J. Stone, (1984) Classification and regression trees, Wadsworth.

[16] H. O. Lancaster, (1969) The chi-squared distribution, John & Sons.

Descriptively probabilistic relationship between mutated primary structure of von Hippel-Lindau protein and its clinical outcome

Shao-Min Yan[1], Guang Wu[2*]

[1]National Engineering Research Center for Non-food Biorefinery, Guangxi Academy of Sciences, 98 Daling Road, Nanning, Guangxi Province, CN-530007, China; [2]Computational Mutation Project, DreamSciTech Consulting, 301, Building 12, Nanyou A-zone, Jiannan Road, Shenzhen, Guangdong Province CN-518054, China; *Corresponding author (hongguanglishibahao@yahoo.com), Tel: +86 771 2503 930, Fax: +86 755 2664 8177.

ABSTRACT

In this study, we use the cross-impact analysis to build a descriptively probabilistic relationship between mutant von Hippel-Lindau protein and its clinical outcome after quantifying mutant von Hippel-Lindau proteins with the amino-acid distribution probability, then we use the Bayesian equation to determine the probability that the von Hippel-Lindau disease occurs under a mutation, and finally we attempt to distinguish the classifications of clinical outcomes as well as the endocrine and nonendocrine neoplasia induced by mutations of von Hippel-Lindau protein. The results show that a patient has 9/10 chance of being von Hippel-Lindau disease when a new mutation occurs in von Hippel-Lindau protein, the possible distinguishing of classifications of clinical outcomes using modeling, and the explanation of the endocrine and nonendocrine neoplasia in modeling view.

Keywords: Amino Acid; Bayes' Law; Cross-Impact Analysis; Distribution Probability; Mutation; Von Hippel-Lindau Disease

1. INTRODUCTION

Perhaps, the first step to study the genotype-phenotype relationship is to determine a protein in relation to a disease, and the second step would be to build a quantitative relationship between mutant protein and its clinical outcome. Then we may be in the position to predict the clinical outcome based on such a quantitative relationship, even to predict new functions led by new mutations.

Thus, we need the methods, which can quantify a protein sequence as a numeric sequence in order to build a quantitative relationship. In fact, we have various ways

to quantify a protein sequence, for example, to use the physicochemical property of amino acid to quantify a protein sequence [1].

Since 1999, we have developed three approaches to quantify each amino acid in a protein as well as a whole protein (for reviews, see [2,3,4]), and our quantifications indeed differ before and after mutation, thus it is possible to use our approaches to build a quantitative relationship between changed primary structure and changed function of protein.

In 1911 and 1926, von Hippel and Lindau described the von Hippel-Lindau disease [5,6], later on Melmon and Rosen established the notion of the von Hippel-Lindau disease [7], which is an autosomal dominant disorder characterized by cerebellar, spinal cord, and retinal hemangioblastomas; cysts of the kidney, pancreas, liver, and epididymis; and has an increased frequency of renal cancer (renal cell carcinoma or hypernephroma), pancreatic cancer, and pheochromocytoma [8,9,10]. The von Hippel-Lindau disease has a birth incidence of about 1 in 36000 and about 20% of cases arise as de novo mutations without a family history [11,12].

The von Hippel-Lindau disease tumor suppressor gene was identified in 1993 [13], of which mutations are the major cause for developing the von Hippel-Lindau disease. Pathologically relevant is inactivation of the von Hippel-Lindau gene and subsequent loss of the function of the von Hippel-Lindau protein, and Elongin B, C complex [14,15]. The dysfunction of the ubiquitination of hypoxia-inducible factors is an important step in the development of various tumors [15,16,17,18,19]. Also, a recent study elucidated the role of NGF/JunB/ EglN3-related pathways in developmental apoptosis linking to tumourigenesis [20].

Clinically the von Hippel-Lindau disease is classified into two types: type I without pheochromocytoma and type II with pheochromocytoma [10,17]. On the other hand, more than 300 different von Hippel-Lindau muta-

tions have been described at DNA level [21,22,23,24], and more than 100 at protein level. It would be great helpful if we can build a quantitative relationship between von Hippel-Lindau protein mutation and von Hippel-Lindau disease status, that is, the relationship between mutant protein and its clinical outcome.

In this study, we build a descriptively quantitative relationship between changed primary structure of mutated von Hippel-Lindau protein and the classification of its clinical outcome, distinguish the classifications of clinical outcomes as well as the endocrine and nonendocrine neoplasia induced by mutations of von Hippel-Lindau protein.

2. MATERIALS AND METHODS

2.1. Data

The human von Hippel-Lindau disease tumor suppressor with total 132 mutations (accession number P40337; December 4, 2007; Entry version 91) is obtained from UniProtKB/Swiss-Prot entry [25]. Among them, 123 are missense point mutations, 7 deletions and 3 insertions.

2.2. Amino-Acid Distribution Probability

Among three approaches developed by us, the amino-acid distribution probability is mainly related to the positions of amino acids along the protein, which is suitable for mutation analysis, and we have used this approach in a number of our previous studies [2,3,4,26,27,28,29,30,31,32,33,34,35,36,37, 38,39,40,41,42,43,44]. The quantification is developed along such a thought, for example, how do two amino acids distribute along a protein sequence? Our intuition may suggest that there would be one amino acid in the first half of the sequence and another one in the second half. In fact, there are only three possible distributions, 1) both amino acids are in the first half, 2) one amino acid is in each half and 3) both amino acids are in the second half. Thus, each distribution has the probability of 1/3. If we do not distinguish either the first half or second half but are simply interested in whether both amino acids are in both halves or in any half, there will be the probability of 1/2 for each distribution.

If we are interested in the distribution probability of three amino acids in a protein, we naturally imagine to grouping the protein into three partitions, and our intuition may suggest that each partition contains an amino acid. If we do not distinguish the first, second and third partition, actually there are totally three types of distributions, i.e. 1) each amino acid is in each partition, 2) two amino acids are in a partition and an amino acid is in another partition, and 3) three amino acids are in a partition.

In this situation, the distribution probability can be calculated according to the statistical mechanics, which classifies the distribution of elementary particles in energy states according to three assumptions of whether distinguishing each particle and energy state, i.e. Maxwell-Boltzmann, Fermi-Dirac and Bose-Einstein as-

sumptions [45]. We actually use the Maxwell-Boltzmann assumption for computing amino-acid distribution probability, which is equal to $\dfrac{r!}{q_0! \times q_1! \times \ldots \times q_n!} \times$ $\dfrac{r!}{r_1! \times r_2! \times \ldots \times r_n!} \times n^{-r}$ [45], where r is the number of amino acids, n is the number of partitions, r_n is the number of amino acids in the n-th partition, q_n is the number of partitions with the same number of amino acids, and ! is the factorial function.

Thus, the distribution probabilities are different for these three types of distributions of three amino acids, say, 0.2222 for 1), 0.6667 for 2) and 0.1111 for 3). Clearly the protein can only adopt one type of distribution for these three amino acids, which is the actual distribution probability.

For four amino acids, there are five distributions, 1) each partition contains an amino acid, 2) a partition contains two amino acids and two partitions contain an amino acid each, 3) two partitions contain two amino acids each, 4) a partition contains an amino acid and a partition contains three amino acids, and 5) a partition contains four amino acids. Their distribution probabilities are 0.0938 for 1), 0.5625 for 2), 0.1406 for 3), 0.1875 for 4), and 0.0156 for 5). Furthermore, there are seven distributions for five amino acids, 11 distributions for six amino acids, 15 distributions for seven amino acids, and so on.

2.3. Quantification of Wild-Type von Hippel-Lindau Protein

Table 1. Amino acids, their composition and distribution probability in wild-type human von Hippel-Lindau protein. (A, alanine; R, arginine; N, asparagine; D, aspartic acid; C, cysteine; E, glutamic acid; Q, glutamine; G, glycine; H, histidine; I, isoleucine; L, leucine; K, lysine; M, methionine; F, phenylalanine; P, proline; S, serine; T, threonine; W, tryptophan; Y, tyrosine; V, valine.)

Amino acid	Number	Distribution probability
A	10	0.0476
R	20	0.0067
N	9	0.1770
D	11	0.1077
C	2	0.5000
E	30	0.0001
Q	8	0.0673
G	18	0.0389
H	5	0.0640
I	6	0.1543
L	20	0.0422
K	3	0.1111
M	3	0.6667
F	5	0.2880
P	19	0.0319
S	11	0.0404
T	7	0.2142
W	3	0.6667
Y	6	0.2315
V	17	0.1280

With respect to the wild-type von Hippel-Lindau protein, for example, there are eight glutamines "Q" in von Hippel-Lindau protein (**Table 1**). We may ask how these eight Qs distribute along the von Hippel-Lindau protein? According to the problem of the occupancy of subpopulations and partitions [45], the simple way to answer this question is to imagine that we would divide the von Hippel-Lindau protein into eight equal partitions, and each partition has about 27 amino acids (213/8=26.625) because the von Hippel-Lindau protein is composed of 213 amino acids, then there would be 22 configurations for all the possible distributions of eight Qs (**Table 2**).

Here, we calculate two distribution probabilities in **Table 2** as example according to the above equation. For eight Qs equally distribute in each partition (the second row in **Table 2**), we have $q_0=0$, $q_1=8$, . . . $q_8=0$; and $r_1=1$, $r_2=1$, . . . $r_8=1$. Thus, we have the distribution probability,

$$\frac{8!}{0!\times 8!\times 0!\times 0!\times 0!\times 0!\times 0!\times 0!\times 0!}\times\frac{8!}{1!\times 1!\times 1!\times 1!\times 1!\times 1!\times 1!\times 1!}\times 8^{-8}$$

$$=\frac{40320}{1\times 40320\times 1\times 1\times 1\times 1\times 1\times 1}\times\frac{40320}{1\times 1\times 1\times 1\times 1\times 1\times 1\times 1}\times\frac{1}{16777216}=0.0024$$

Clearly, the von Hippel-Lindau protein can adopt only one distribution pattern, which is that two partitions contain zero Q, five partitions contain one Q and one partition contains three Qs (the fourth row in **Table 2**).

So we have $q_0=2$, $q_1=5$, $q_2=0$, $q_3=1$, $q_4=0$, $q_5=0$, $q_6=0$, $q_7=0$, $q_8=0$; and $r_1=0$, $r_2=0$, $r_3=1$, $r_4=1$, $r_5=1$, $r_6=1$, $r_7=1$, $r_8=3$, that is,

$$\frac{8!}{2!\times 5!\times 0!\times 1!\times 0!\times 0!\times 0!\times 0!\times 0!}\times\frac{8!}{0!\times 0!\times 1!\times 1!\times 1!\times 1!\times 1!\times 3!}\times 8^{-8}$$

$$=\frac{40320}{2\times 120\times 1\times 1\times 1\times 1\times 1\times 1}\times\frac{40320}{1\times 1\times 1\times 1\times 1\times 1\times 6}\times\frac{1}{16777216}=0.0673$$

In such a manner, we can quantify each amino acid in wild-type von Hippel-Lindau protein. Thereafter, we can assign these probabilities to each amino acid in the von Hippel-Lindau protein as shown in **Figure 1**, from which we get the visual sense of how these distribution probabilities go along the von Hippel-Lindau protein, and more importantly we can sum up these distribution probabilities together for all 213 amino acids in the protein.

Actually, the Maxwell-Bolzmann assumption provides us a way to estimate the position of amino acid in a protein, because there is a standard method for the computation using Maxwell-Bolzmann assumption, which saves us from inventing new computational methods. Moreover, the primary structure is the base for higher-level structure, thus any mutation in primary structure would lead to the change in distribution probability, in higher-level structure, and finally the biological function. This is the biological meaning of use of Maxwell-Bolzmann assumption for quantify-

Table 2. All possible distributions of eight glutamines in von Hippel-Lindau protein. (Bold and italic is the real distribution.)

| Partition 1	Partition 2	Partition 3	Partition 4	Partition 5	Partition 6	Partition 7	Partition 8	Probability
1	1	1	1	1	1	1	1	0.002403
	1	1	1	1	1	1	2	0.0673
		1	*1*	*1*	*1*	*1*	*3*	*0.0673*
			1	1	1	1	4	0.0280
				1	1	1	5	5.6076e-3
					1	1	6	5.6076e-4
						1	7	2.6703e-5
							8	4.7684e-7
		1	1	1	1	2	2	0.2523
			1	1	1	2	3	0.2243
				1	1	2	4	0.0421
					1	2	5	3.3646e-3
						2	6	9.3460e-5
			1	1	2	2	2	0.1682
				1	2	2	3	0.0841
					2	2	4	4.2057e-3
				2	2	2	2	0.0105
				1	1	3	3	0.0280
					2	3	3	5.6076e-3
					1	3	4	5.6076e-3
						4	4	1.1683e-4
						3	5	1.8692e-4
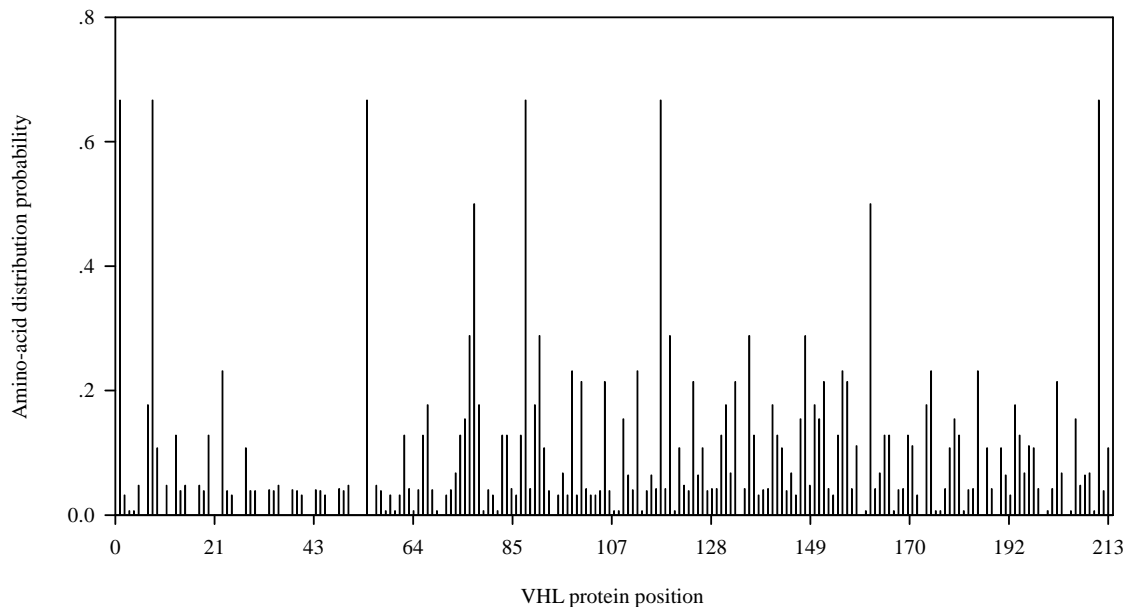
Figure 1. Visualization of amino-acid distribution probability in wild-type human von Hippel-Lindau protein.

cation of protein sequence.

In this context, any clinical manifestations related to mutation in proteins would have different distribution probabilities determined by Maxwell-Bolzmann assumption. This is the association between them.

2.4. Quantification of Mutated von Hippel-Lindau Proteins

The calculation in the above subsection is referred to the amino-acid distribution probability before mutation, say, the amino-acid distribution probability in wild-type von Hippel-Lindau protein. Obviously any point mutation leads an amino acid to change to another one, which certainly would change the distribution pattern of both

original and mutated amino acids, thus the amino-acid distribution probability would differ for both original and mutated amino acids between before and after mutation.

For example, the missense mutations at the CpG mutation hotspot at codon 167 can mutate arginine "R" to glycine "G", or glutamine "Q" or tryptophan "W" [13, 46] leading to type I-II, type II and type II von Hippel-Lindau disease, respectively. In above subsection, we have calculated the distribution probability of Qs (**Table 2**) before mutation, and now we show the calculation of distribution probability after R167Q mutation.

After this mutation, there are nine Qs in the von Hippel-Lindau mutant (**Table 3**), for which we have

$$\frac{9!}{5!\times 1!\times 1!\times 2!\times 0!\times 0!\times 0!\times 0!\times 0!\times 0!} \times \frac{9!}{0!\times 0!\times 0!\times 2!\times 0!\times 1!\times 3!\times 0!\times 3!} \times 9^{-9} = 0.0197$$

while its distribution probability before this mutation is 0.0673, so the mutation decreases the distribution probability of Q. On the other hand, there are 20 and 19 Rs before and after this mutation. Their distribution probabilities are 0.0067 and 0.0030 before and after mutation, so this mutation decreases the distribution probability of R, too. The overall effect for this mutation is (0.0030–0.0067)+ (0.0197–0.0673)=–0.0513, that is, the mutation reduces the distribution probability for von Hippel-Lindau protein.

Since von Hippel-Lindau protein functions as whole, we can calculate the change led by the mutation in following way. The sum of all the distribution probability is 19.6114 in wide-type von Hippel-Lindau protein (**Figure 1**), while the above calculated mutation leads the sum of all the distribution probability to be 19.1731, thus this

mutation results in 2.23% decrease in the measure [(19.1731–19.6114)/19.6114%].

In this way, we have the quantitative measure for the changed primary structure of von Hippel-Lindau mutants and we also have documented clinical manifestations induced by the mutations of von Hippel-Lindau protein, thus we can build a quantitative relationship between changed structure and clinical outcome.

2.5. Descriptively Probabilistic Relationship

For building quantitative relationship between mutation and clinical outcome, we use the descriptively probabilistic method, as our quantification is the amino-acid distribution probability and each individual mutation related to its clinical outcome is presented as frequency. Therefore, we use the cross-impact analysis to couple

Table 3. Distribution pattern of glutamines before and after mutation at position 167 in von Hippel-Lindau protein.

Partition	I	II	III	IV	V	VI	VII	VIII	IX
Before mutation	0	0	1	1	1	1	1	3	-
After mutation	0	0	0	2	0	1	3	0	3

them [35,47,48,49,50,51,52,53], because the amino-acid distribution probability either increases or decreases after mutation, which is a 2-possibilty event, and the clinical outcome either occurs or does not occur after mutation, which is a yes-and-no event. Thereafter, we can use the Bayesian equation to calculate the probability of occurrence of clinical outcome under a mutation.

2.6. Classification of Clinical Outcomes

It is extremely challenging how to use a mathematical modeling to distinguish the clinical outcomes with respect to mutant von Hippel-Lindau protein because of the variety of clinical outcomes. In an effort towards solving this problem, we employ our second quantification, amino-acid pair predictability, whose relational and applications have been published intensively (for reviews, see [2,3,4]).

This quantification is based on permutation, and can be calculated in the following way. For example, there are 30 glutamic acids "E" and 20 Rs in von Hippel-Lindau protein, the predicted frequency of amino-acid pair ER would be 3 ($30/213 \times 20/212 \times 212 = 2.817$), while we do find three ERs in the protein, so the amino- acid pair ER is predictable. Still, the predicted frequency of EE would be 4 ($30/213 \times 29/212 \times 212 = 4.085$), but actually the EE appears nine times in reality. This is the case that the actual frequency is larger than its predicted one. In this manner, we can quantify a protein sequence according to the percentage of how many amino-acid pairs are predictable among all the amino-acid pairs in given protein as well as its mutants. For instance, the predictable portion of amino-acid pairs is 27.54% in wild-type von Hippel-Lindau protein and 31.88% in its P25L mutant.

2.7. Statistics

The data are presented as mean±SD for normal distribution or median with interquatile range for non-normal distribution. The Kruskal-Wallis one-way ANOVA and Chi-square are used for statistical inference, and P < 0.05 is considered significant.

3. RESULTS AND DISCUSSION

After computing amino-acid distribution probability in wild-type von Hippel-Lindau protein and in its 132 mutants, we have 132 changed amino-acid distribution probabilities. Firstly, we can use the cross-impact analysis to build a quantitative relationship between the increase/decrease of distribution probability after muta-

tions and the clinical diagnosis, because the cross-impact analysis is particularly suited for two relevant events coupled together [35,47,48,49,50,51,52,53].

Figure 2 displays the cross-impact analysis on the relationship between changed primary structure and von Hippel-Lindau disease. At the level of amino-acid distribution probability, $P(2)$ and $P(\bar{2})$ are the decreased and increased probabilities induced by mutations, and 53 and 79 mutations result in the distribution probability decreased and increased, respectively. At the level of clinical diagnosis: 1) $P(1|\bar{2})$ is the impact probability (conditional probability) that the von Hippel-Lindau disease is diagnosed under the condition of increased distribution probability, and 70 mutations have such an effect. 2) $P(\bar{1}|\bar{2})$ is the impact probability that other disease is diagnosed under the condition of increased distribution probability, and 9 mutations work in such a manner. 3) $P(1/2)$ is the impact probability that the von Hippel-Lindau disease is diagnosed under the condition of decreased distribution probability, and 44 mutations play such a role. 4) $P(\bar{1}|2)$ is the impact probability that other disease is diagnosed under the condition of decreased distribution probability, and 9 mutations fall into this category. At the level of combined events, we can see the combined results of changed structure and von Hippel-Lindau disease.

Table 4 lists the calculated probabilities with respect to **Figure 2**, from which several interesting points can be drawn. 1) As $P(\bar{2})$ is larger than $P(2)$, a mutation has a larger chance of increasing the distribution probability in von Hippel-Lindau mutant. 2) As $P(1|\bar{2})$ is much larger than $P(\bar{1}|\bar{2})$, a mutation that increases the distribution probability has about nine tenth chance of being von Hippel-Lindau disease. 3) As $P(1/2)$ is much larger than $P(\bar{1}|2)$, a mutation that decreases the distribution probability has much larger chance of being von Hippel-Lindau disease.

Table 4. Computed probabilities in reference to the cross-impact analysis in **Figure 2**.

$P(2)=53/132=0.4015$

$P(\bar{2})=1-P(2)=1-0.4015=0.5985=79/132$

$P(1|\bar{2})=70/79=0.8861$

$P(\bar{1}|\bar{2})=1-P(1|\bar{2})=1-0.8861=0.1139=9/79$

$P(1|2)=44/53=0.8302$

$P(\bar{1}|2)=1-P(1/2)=1-0.8302=0.1698=9/53$

$P(1\bar{2})=P(1|\bar{2})\times P(\bar{2})=70/79\times79/132=0.5303=70/132$

$P(\bar{1}\bar{2})=P(\bar{1}|\bar{2})\times P(\bar{2})=9/79\times79/132=0.0682=9/132$

$P(12)=P(1/2)\times P(2)=44/53\times53/132=0.3333=44/132$

$P(\bar{1}2)=P(\bar{1}|2)\times P(2)=9/53\times53/132=0.0682=9/132$
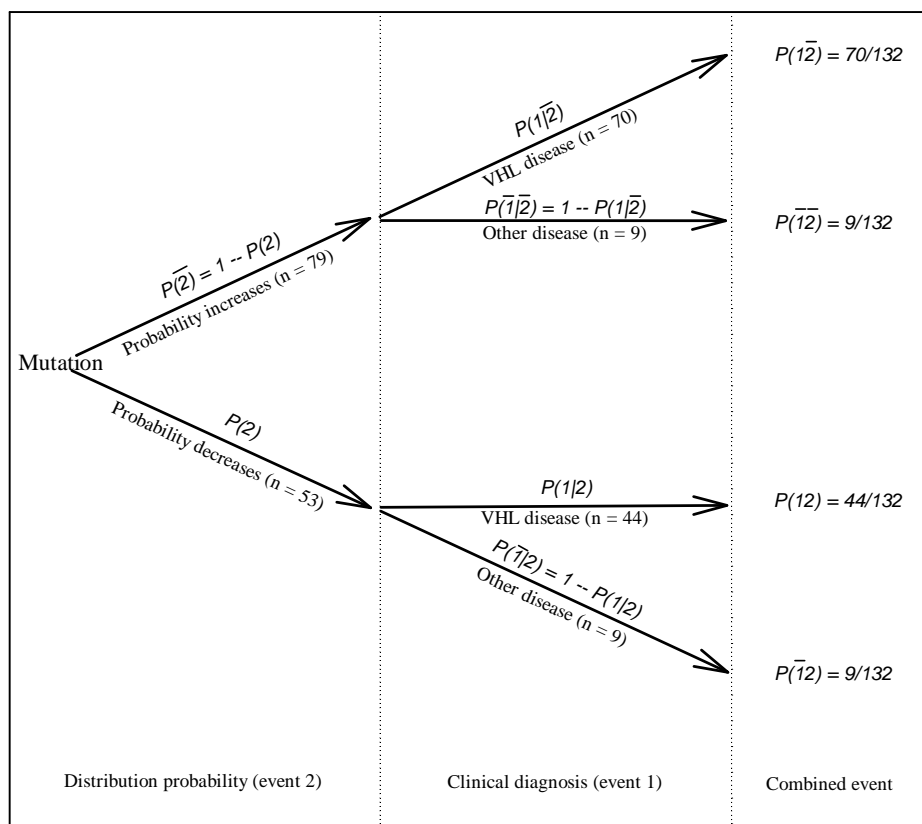
Figure 2. Cross-impact relationship among von Hippel-Lindau protein mutation, changed amino- acid distribution probability, and clinical diagnosis.

Secondly, we use the Bayes' law $P(1|2) = P(2|1)\frac{P(1)}{P(2)}$, which indicates the probabilities of occurrences of two events [54], to determine the probability, $P(1)$, von Hippel-Lindau disease under a mutation, because $P(2)$ and $P(1|2)$ have already been defined in cross- impact analysis, while $P(2|1)$ is the probability that the distribution probability decreases under the condition that the von Hippel-Lindau disease is diagnosed.

As $P(1/2)=44/53=0.8302$ (**Table 4**), and $P(2|1) = 44/(44+70)=0.3860$, $P(1) = \frac{P(1|2)}{P(2|1)}P(2) = \frac{0.8302 \times 0.4015}{0.3860}$ $=0.8635$, namely, the patient has nine tenth chance of being von Hippel-Lindau disease when a new mutation is found in von Hippel-Lindau protein.

Among patients with von Hippel-Lindau disease, about 40% of mutations are genomic deletions and the rest are predominantly truncating or missense mutations, which do not occur within the first 53 amino acids [55,56]. In this study, we focus on the mutations of von Hippel-Lindau protein. From a probabilistic viewpoint, our results indicate the chance of being diagnosed as the von Hippel-Lindau disease when a new von Hippel-

Lindau mutant occurs.

The von Hippel-Lindau disease is characterized by marked phenotypic variability [57,58], due to mosaicism [59], modifier effects [60], and mainly allelic heterogeneity [61]. All these result in complicated clinical classifications. Thus, we use the predictable portion of amino-acid pairs to model the classifications.

Figure 3 illustrates the classification with respect to the predictable portion of amino-acid pairs. Although there are large overlaps among classifications, our quantification already distinguishes them to some degree. For example, in comparison with von Hippel-Lindau disease, our quantification shows relatively lower in pheochromocytoma and higher in other disorders ($P=0.079$, Kruskal-Wallis one-way ANOVA). The lack of statistical significance is certainly, in part, due to few cases in some groups, however the trend is clear, which paves the way for further classification using more sophisticated mathematical models.

Genotype-phenotype relationships have revealed that a certain number of missense mutations are associated with a high risk of pheochromocytoma but the mutations that totally loss their functions are associated with a low risk. Most patients with type II von Hippel-Lindau disease have missense mutations whereas the large dele-
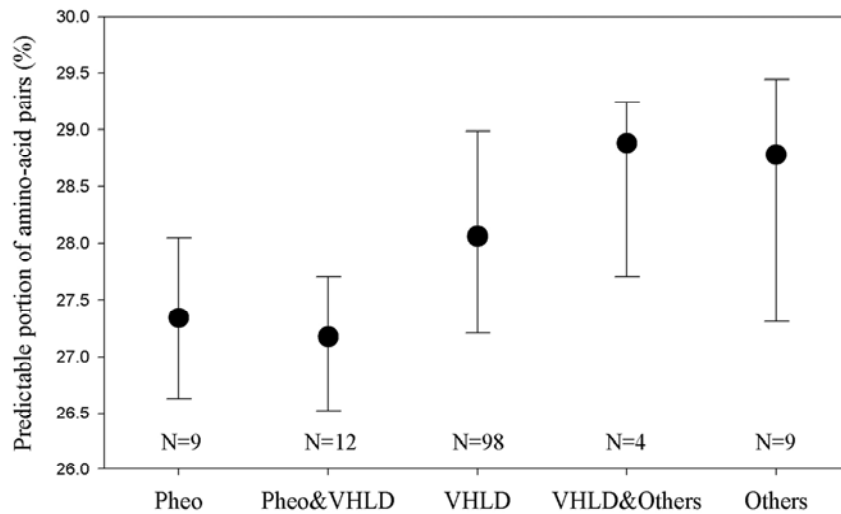
Figure 3. Predictable portion of amino-acid pairs induced by mutations of von Hippel-Lindau protein in pheochromocytoma (Pheo), von Hippel-Lindau disease and other disorders. The data are presented as median with an interquatile range ($P = 0.079$, Kruskal-Wallis one-way ANOVA).
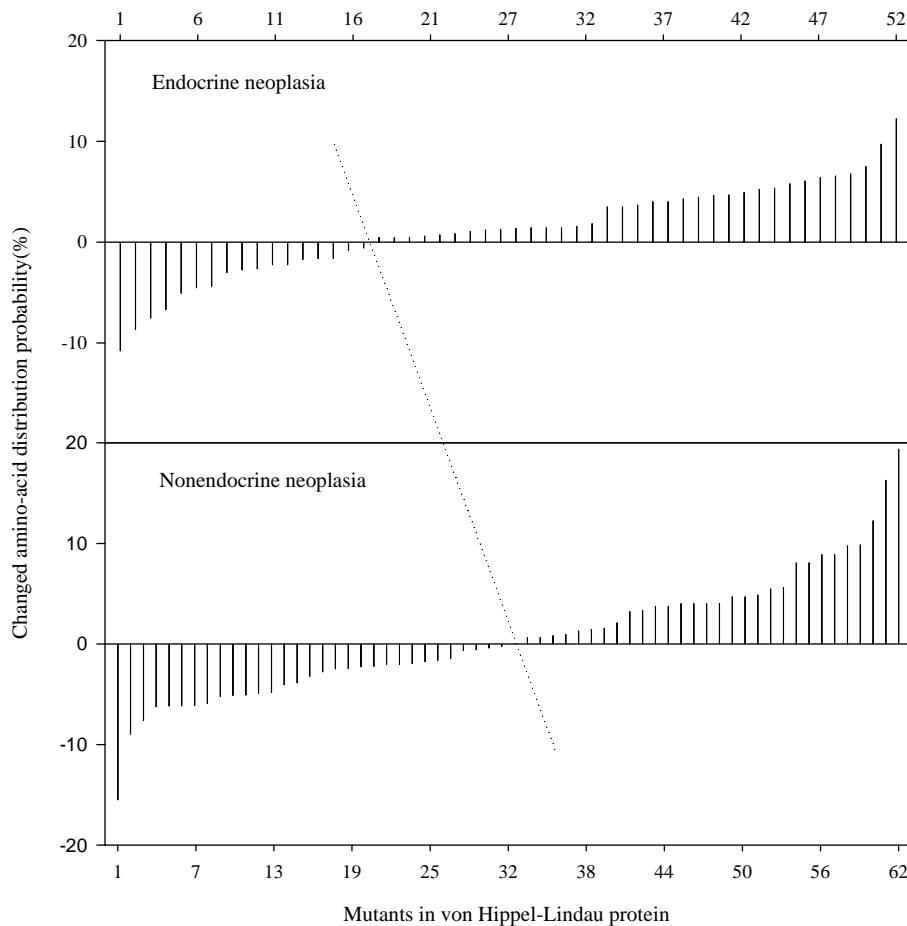

Figure 4. Distribution of changed amino-acid distribution probability in endocrine and nonendocrine neoplasia induced by mutations of von Hippel-Lindau protein ($P = 0.094$, Chi-square).

tions and truncating mutations predominate in type I families [11,19,62,63]. Many missense mutations causing a type I phenotype are involved in the core hydrophobic residues and were predicted to disrupt protein structure, whereas type II phenotype missense mutations are involved in substitutions at a surface amino acid that does not cause a total loss of function [64,65].

Figure 4 displays the distribution of changed amino-acid distribution probability in endocrine neoplasia (pheochromocytoma, type II von Hippel-Lindau disease) and nonendocrine neoplasia (type I von Hippel-Lindau disease). As can be seen, the mutations that led to the endocrine neoplasia have the trend to increase the amino-acid distribution probability (upper panel), whereas the mutations that led to nonendocrine neoplasia have the effect to either increase or decrease the amino-acid distribution probability (lower panel). The difference between two panels is mainly considered from view of symmetry. As the x-axis is related to the number of von Hippel-Lindau mutations, this figure would be different when more mutations would be found in future, which might provide the much clearer pattern, although we did not find the statistical difference between two panels (P=0.094, Chi-square) now.

From a theoretical viewpoint, one could consider to calculate the distribution probability of all 19 potential types of mutations at each position of von Hippel-Lindau protein, and then find the link between mutations and clinical outcomes. However, the amount of computation is huge because it would be equal to 2.369×10^{272} mutations (19^{213}), which is not only beyond the capacity of any computers, but also beyond the capacity for comparison. Actually, we really know that each position does not have 19 types of potential mutations, because this mutation process is governed by the translation probability between RNA codon and mutated amino acids [66,67,68]. On the other hand, our study is focused on the documented data rather than the simulated data.

In this study, we use a single value, the sum of all distribution probability to represent the normal von Hippel-Lindau protein and its mutated proteins, respectively, because there is no other way to use a single value dynamically to represent a protein, namely, the value is different when a protein is different. Without such a measure, we cannot model a protein dynamically with its mutations. To the best of knowledge, currently it is only the accession number that can represent a protein uniquely, however it has nothing to do with the protein itself, i.e. composition, length, function, etc.

In general, one would hope to verify this type of study against the real-life cases, which is possible in future although it would deal with a large-scale collaboration because this type of diseases is not frequently seen in clinical settings, for example, the von Hippel-Lindau disease has a birth incidence of about 1 in 36 000 [11,12].

It will take years to verify what a theoretical study finds with fast-speed computational technique. Even, we cannot verify all the theoretical studies, for example, we cannot create another earth without global warming.

The implications of this study include two aspects. 1) The relationship between changed primary structure and changed function is very meaningful, because it provides the dynamic rather than static relationship between mutant protein and its function. This can furthermore provide us the basis for building a dynamic model to predict the new function in mutant proteins. Nevertheless, we need to quantify the proteins in order to build a dynamic model and this study is doing in such a way. 2) From the clinical viewpoint, the classification of von Hippel-Lindau disease as well as many mutation related diseases needs a considerable amount of clinical assays. Our approach can provide a probabilistic estimate for disease classification after determining which amino acid has mutated, because the primary structure of protein is the base for its high-level structure and function.

4. ACKNOWLEDGEMENTS

REFERENCES

[1]   K. C. Chou, (2004) Structure bioinformatics and its impact to biomedical science, Curr. Med. Chem, **11**, 2105‒2134.

[2]   G. Wu and S. Yan, (2002) Randomness in the primary structure of protein: Methods and implications, Mol. Biol. Today, **3**, 55‒69.

[3]   G. Wu and S. Yan, (2006) Mutation trend of hemagglutinin of influenza A virus: A review from computational mutation viewpoint, Acta Pharmacol. Sin., **27**, 513‒526.

[4]   G. Wu and S. Yan, (2008) Lecture notes on computational mutation, Nova Science Publishers, New York, 2008.

[5]   Von Hippel, (1911) Die anatomische Grund lage der von mir beschriebenen 'sehr seltenen Erkrankung der Netzhaut', Graefes. Arch. Ophthalmol., **79**, 350‒377.

[6]   A. Lindau, (1926) Studien uber kleinhirncysten, bau, pathogenese und bezoejimgem zur angiomatosis retinae, Acta Pathol. Microbiol. Scand., Suppl **1**, 1‒128.

[7]   K. L. Melmon and S. W. Rosen, (1964) Lindau's disease, Am. J. Med., **36**, 595‒617.

[8]   V. V. Michels, (1988) Investigative studies in von Hippel-Lindau disease, Neurofibromatosis, **1**, 159‒163.

[9]   H. P. Neumann, (1987) Basic criteria for clinical diagnosis and genetic counselling in von Hippel-Lindau syndrome, Vasa, **16**, 220‒226.

[10]   R. R. Lonser, G. M. Glenn, M. Walther, E. Y. Chew, S. K. Libutti, W. M. Linehan, and E. H. Oldfield, (2003) von Hippel-Lindau disease, Lancet, **361**, 2059‒2067.

[11]   E. R. Maher, A. R. Webster, F. M. Richards, J. S. Green, P. A. Crossey, S. J. Payne, and A. T. Moore, (1996) Phenotypic expression in von Hippel-Lindau disease: Corre-

lations with germline VHL gene mutations, J. Med. Genet., **33**, 328−332.

[12] F. M. Richards, S. J. Payne, B. Zbar, N. A. Affara, M. A. Ferguson-Smith, and E. R. Maher, (1995) Molecular analysis of de novo germline mutations in the von Hippel-Lindau disease gene, Hum. Mol. Genet., **4**, 2139−2143.

[13] F. Latif, K. Tory, J. Gnarra, M. Yao, F. M. Duh, M. L. Orcutt, *et al.*, (1993) Identification of the von Hippel-Lindau disease tumor suppressor gene, Science, **260**, 1317−1320.

[14] P. O. Schnell, M. L. Ignacak, A. L. Bauer, J. B. Striet, W. R. Paulding, and M. F. Czyzyk-Krzeska, (2003) Regulation of tyrosine hydroxylase promoter activity by the von Hippel-Lindau tumor suppressor protein and hypoxia-inducible transcription factors, J. Neurochem., **85**, 483−491.

[15] W. G. Jr. Kaelin, (2002) Molecular basis of the VHL hereditary cancer syndrome, Nat. Rev. Cancer, **2**, 673−682.

[16] W. G. Jr. Kaelin, (2003) The von Hippel-Lindau gene, kidney cancer, and oxygen sensing, J. Am. Soc. Nephrol., **14**, 2703 −2711.

[17] T. Shuin, I. Yamasaki, K. Tamura, H. Okuda, M. Furihata, and S. Ashida, (2006) Von Hippel-Lindau disease: Molecular pathological basis, clinical criteria, genetic testing, clinical features of tumors and treatment, Jpn. J. Clin. Oncol., **36**, 337−343.

[18] M. Ohh, (2006) Ubiquitin pathway in VHL cancer syndrome, Neoplasia, **8**, 623−629.

[19] F. Chen, T. Kishida, M. Yao, T. Hustad, D. Glavac, M. Dean, J. R. Gnarra, M. L. Orcutt, F. M. Duh, G. Glenn, J. Green, Y. E. Hsia, J. Lamiell, H. Li, M. H. Wei, L. Schmidt, K. Tory, I. Kuzmin, T. Stackhouse, F. Latif, W. M. Linehan, M. Lerman, and B. Zbar, (1995) Germline mutations in the von Hippel-Lindau disease tumor suppressor gene: Correlations with phenotype, Hum. Mutat., **5**, 66−75.

[20] S. Lee, E. Nakamura, H. Yang, W. Wei, M. S. Linggi, M. P. Sajan, R. V. Farese, R. S. Freeman, B. D. Carter, W. G. Jr. Kaelin, and S. Schlisio, (2005) Neuronal apoptosis linked to EglN3 prolyl hydroxylase and familial phaeochromocytoma genes: developmental culling and cancer. Cancer Cell, **8**, 1−13.

[21] Clinical Research Group for VHL in Japan, (1995) Germline mutations in the von Hippel-Lindau disease (VHL) gene in Japanese VHL, Hum. Mol. Genet., **4**, 2233−2237.

[22] H. P. Neumann, B. Bender, I. Zauner, D. P. Berger, C. Eng, H. Brauch, and B. Zbar, (1996) Monogenetic hypertension and pheochromocytoma, Am. J. Kidney Dis., **28**, 329−333.

[23] S. Olschwang, S. Richard, C. Boisson, S. Giraud, P. Laurent- Puig, F. Resche, and G. Thomas, (1998) Germline mutation profile of the VHL gene in von Hippel-Lindau disease and in sporadic hemangioblastoma, Hum. Mutat., **12**, 424−430.

[24] C. Stolle, G. Glenn, B. Zbar, J. S. Humphrey, P. Choyke, M. Walther, S. Pack, K. Hurley, C. Andrey, R. Klausner, and W. M. Linehan, (1998) Improved detection of germline mutations in the von Hippel-Lindau disease tumor suppressor gene, Hum. Mutat., **12**, 417−423.

[25] A. Bairoch and R. Apweiler, (2000) The SWISS-PROT protein sequence data bank and its supplement TrEMBL in 2000, Nucleic Acids Res., **28**, 45−48.

[26] N. Gao, S. Yan, and G. Wu, (2006) Pattern of positions sensitive to mutations in human haemoglobin α-chain, Protein Pept. Lett., **13**, 101−107.

[27] G. Wu and S. Yan, (2000) Prediction of distributions of amino acids and amino acid pairs in human haemoglobin α-chain and its seven variants causing-thalassemia from their occurrences according to the random mechanism, Comp. Haematol. Int, **10**, 80−84.

[28] G. Wu and S. Yan, (2001) Analysis of distributions of amino acids, amino acid pairs and triplets in human insulin precursor and four variants from their occurrences according to the random mechanism, J. Biochem. Mol. Biol. Biophys., **5**, 293−300.

[29] G. Wu and S. Yan, (2001) Analysis of distributions of amino acids and amino acid pairs in human tumor necrosis factor precursor and its eight variants according to random mechanism, J. Mol. Model, **7**, 318−323.

[30] G. Wu and S. Yan, (2002) Random analysis of presence and absence of two-and three-amino-acid sequences and distributions of amino acids, two- and three-amino-acid sequences in bovine p53 protein, Mol. Biol. Today, **3**, 31−37.

[31] G. Wu and S. Yan, (2002) Analysis of distributions of amino acids in the primary structure of apoptosis regulator Bcl-2 family according to the random mechanism, J. Biochem. Mol. Biol. Biophys, **6**, 407−414.

[32] G. Wu and S. Yan, (2002) Analysis of distributions of amino acids in the primary structure of tumor suppressor p53 family according to the random mechanism, J. Mol. Model, **8**, 191−198.

[33] G. Wu and S. Yan, (2004) Determination of sensitive positions to mutations in human p53 protein, Biochem. Biophys. Res. Commun., **321**, 313−319.

[34] G. Wu and S. Yan, (2005) Searching of main cause leading to severe influenza A virus mutations and consequently to influenza pandemics/epidemics, Am. J. Infect. Dis., **1**, 116−123.

[35] G. Wu and S. Yan, (2005) Prediction of mutation trend in hemagglutinins and neuraminidases from influenza A viruses by means of cross-impact analysis, Biochem. Biophys. Res. Commun., **326**, 475−482.

[36] G. Wu and S. Yan, (2006) Timing of mutation in hemagglutinins from influenza A virus by means of amino-acid distribution rank and fast Fourier transform, Protein Pept. Lett., **13**, 143−148.

[37] G. Wu and S. Yan, (2006) Prediction of possible mutations in H5N1 hemagglutinins of influenza A virus by means of logistic regression, Comp. Clin. Pathol., **15**, 255−261.

[38] G. Wu and S. Yan, (2006) Prediction of mutations in H5N1 hemagglutinins from influenza A virus, Protein Pept. Lett., **13**, 971−976.

[39] G. Wu and S. Yan, (2007) Improvement of model for prediction of hemagglutinin mutations in H5N1 influenza

viruses with distinguishing of arginine, leucine and serine, Protein Pept. Lett., **14**, 191–196.

[40] G. Wu and S. Yan, (2007) Improvement of prediction of mutation positions in H5N1 hemagglutinins of influenza A virus using neural network with distinguishing of arginine, leucine and serine, Protein Pept. Lett., **14**, 465–470.

[41] G. Wu and S. Yan, (2007) Prediction of mutations engineered by randomness in H5N1 neuraminidases from influenza A virus, Amino Acids, **34**, 81–90.

[42] G. Wu and S. Yan, (2007) Prediction of mutations in H1 neuraminidases from North America influenza A virus engineered by internal randomness, Mol. Divers., **11**, 131–140.

[43] G. Wu and S. Yan, (2008) Prediction of mutations initiated by internal power in H3N2 hemagglutinins of influenza A virus from North America, Int. J. Pept. Res. Ther., **14**, 41–51.

[44] G. Wu and S. Yan, (2008) Prediction of mutation in H3N2 hemagglutinins of influenza A virus from North America based on different datasets, Protein Pept. Lett., **15**, 144–152.

[45] W. Feller, (1968) An introduction to probability theory and its applications, 3rd ed, Wiley, New York, **1**, 34–40.

[46] B. Zbar, T. Kishida, F. Chen, L. Schmidt, E. R. Maher, F. M. Richards, P. A. Crossey, A. R. Webster, N. A. Affara, M. A. Ferguson-Smith, *et al*., (1996) Germline mutations in the Von Hippel-Lindau disease (VHL) gene in families from North America, Europe, and Japan, Hum. Mutat., **8**, 348–357.

[47] T. G. Gordon and H. Hayward, (1968) Initial experiments with the cross-impact matrix method of forecasting, Futures, **1**, 100–116.

[48] T. G. Gordon, (1969) Cross-impact matrices - an illustration of their use for policy analysis, Futures, **2**, 527–531.

[49] S. Enzer, (1970) Delphi and cross-impact techniques: an effective combination for systematic futures analysis, Futures, **3**, 48–61.

[50] S. Enzer, (1970) Cross-impact techniques in technology assessment, Futures, **4**, 30–51.

[51] A. P. Sage, (1977) Methodology for large-scale systems, McGraw-Hill, New York, 165–203.

[52] G. Wu, (2000) Application of cross-impact analysis to the relationship between aldehyde dehydrogenase 2 and flushing, Alcohol Alcohol., **35**, 55–59.

[53] G. Wu and S. Yan, (2008) Building quantitative relationship between changed sequence and changed oxygen affinity in human hemoglobin-chain, Protein Pept. Lett., **15**, 341–345.

[54] Wikipedia, (2008) Bayes' theorem, http://en.wikipedia.org/wiki/ Bayes'_theorem.

[55] S. O. Ang, H. Chen, K. Hirota, V. R. Gordeuk, J. Jelinek, Y. Guan, E. Liu, A. I. Sergueeva, G. Y. Miasnikova, D. Mole, P. H. Maxwell, D. W. Stockton, G. L. Semenza, and J. T. Prchal., (2002) Disruption of oxygen homeostasis underlies congenital Chuvash polycythemia, Nature Genet., **32**, 614–621.

[56] Y. Pastore, K. Jedlickova, Y. Guan, E. Liu, J. Fahner, H. Hasle, J. F. Prchal, and J. T. Prchal., (2003) Mutations of von Hippel- Lindau tumor-suppressor gene and congenital polycythemia, Am. J. Hum. Genet., **73**, 412–419.

[57] E. R. Maher, (2004) Von Hippel-Lindau disease, Curr. Mol. Med., **4**, 833–842.

[58] E. R. Woodward and E. R. Maher, (2006) Von Hippel-Lindau disease and endocrine tumour susceptibility, End. Relat. Cancer, **13**, 415–425.

[59] M. T. Sgambati, C. Stolle, P. L. Choyke, M. M. Walther, B. Zbar, W. M. Linehan, and G. M. Glenn, (2000) Mosaicism in von Hippel-Lindau disease: lessons from kindreds with germline mutations identified in offspring with mosaic parents, Am. J. Hum. Genet., **66**, 84–91.

[60] A. R. Webster, F. M. Richards, F. E. MacRonald, A. T. Moore, and E. R. Maher, (1998) An analysis of phenotypic variation in the familial cancer syndrome von Hippel-Lindau disease: evidence for modifier effects, Am. J. Hum. Genet., **63**, 1025–1035.

[61] P. A. Crossey, C. Eng, M. Ginalska-Malinowska, T. W. J. Lennard, J. R. Sampson, B. A. J. Ponder, and E. R. Maher, (1995) Molecular genetic diagnosis of von Hippel-Lindau disease in familial phaeochromocytoma, J. Med. Genet., **32**, 885–886.

[62] P. A. Crossey, F. M. Richards, K. Foster, J. S. Green, A. Prowse, F. Latif, M. I. Lerman, B. Zbar, N. A. Affara, M. A. Ferguson-Smith, and R. Maher, (1994) Buys CHCM, identification of intragenic mutations in the von Hippel-Lindau disease tumour suppressor gene and correlation with disease phenotype, Hum. Mol. Genet., **3**, 1303–1308.

[63] E. R. Maher, A. R. Webster, F. M. Richards, J. S. Green, P. A. Crossey, S. J. Payne, and A. T. Moore, (2000) Phenotypic expression in von Hippel-Lindau disease: correlations with germline VHL gene mutations, J. Med. Genet., **37**, 62–63.

[64] C. E. Stebbins, W. G. Jr. Kaelin, and N. P. Pavletich, (1999) Structure of the VHL-ElonginC-ElonginB complex: Implications for VHL tumor suppressor function, Science, **284**, 455–461.

[65] S. J. Marx and W. F. Simonds, (2005) Hereditary hormone excess: Genes, molecular pathways, and syndromes, End. Rev., **26**, 615–661.

[66] G. Wu and S. Yan, (2005) Determination of mutation trend in proteins by means of translation probability between RNA codes and mutated amino acids, Biochem. Biophys. Res. Commun., **337**, 692–700.

[67] G. Wu and S. Yan, (2006) Determination of mutation trend in hemagglutinins by means of translation probability between RNA codons and mutated amino acids, Protein Pept. Lett., **13**, 601–609.

[68] G. Wu and S. Yan, (2007) Translation probability between RNA codons and translated amino acids, and its applications to protein mutations, in: Leading-Edge Messenger RNA Research Communications, ed. Ostrovskiy M. H. Nova Science Publishers, New York, Chapter **3**, 47–65.

Effects of granulocyte colony-stimulating factor and stem cell factor, alone and in combination, on the biological behaviours of bone marrow mesenchymal stem cells

Feng-Ping Tang[1], Xing-Huo Wu[2], Xi-Lin Yu[1], Shu-Hua Yang[2], Wei-Hua Xu[2], Jin Li[2]

[1]Wuhan Medical & Health Center for Women and Children, Wuhan, China; [2]Department of Orthopaedics, Union Hospital, Tongji Medical College, Science and Technology of Huazhong University, Wuhan, China; Corresponding author: Xing-Huo Wu, Fax: 086-027-85351627.
Email: wuxinghuo_71@yahoo.com.cn

ABSTRACT

Aim: The effects of granulocyte colony- stimulating factor (G-CSF) and stem cell factor (SCF) on the proliferation and osteogenic differentiation capacity of bone marrow mesenchymal stem cells (MSCs) were studied in the experiment. Methods: Bone marrow MSCs were collected from rabbits successfully, and treated with various concentrations of G-CSF, SCF or a combination of the two. Flow cytometric analyse, MTT test, CFU-F assay, and alkaline phosphatase (ALP) activity measurement were employed. Results: The results of flow cytometry showed that immunophenotype of the cells were CD29$^+$/CD45$^-$, CD105$^+$/ CD34$^-$, CD90$^+$/ HLADR$^-$. MSCs were shown to constitutively express low levels of c-kit which could be enhanced by SCF. G-CSF and SCF had an obvious facilitative effect on the proliferation of MSCs in a dose-dependent fashion. In addition, G-CSF and SCF would be effective in reversibly preventing their differentiation, as showed by the decrease of ALP activity, leading to self-renewal rather than differentiative cell divisions. The effects of G-CSF were superior to SCF. And cells in the group treated with combination of G-CSF and SCF showed more powerful effects than the groups treated with G-CS, SCF, or none of the two. Conclusion: On the whole, these studies demonstrated that MSCs responded to G-CSF, SCF, and to G-CSF plus SCF in a manner that suppressed differentiation, and promotes proliferation and self-renewal, and support the view that these factors could act synergistically.

Keywords: Granulocyte Colony-Stimulating Factor; Stem Cell Factor; Synergistic Effect; Bone Marrow Mesenchymal Stem Cells

1. INTRODUCTION

Bone marrow is composed of various types of cells of specific phenotypes and function. Bone marrow cells can be transplanted either as total, unfractionated bone marrow or as a well-defined subpopulation of bone marrow mesenchymal stem cells (MSCs) [1,2]. MSC is a group of multipotent cells that can expand, self-replicate, and differentiate into many cell types under appropriate conditions [3,4]; their progeny includes chondrocytes, tendon cells, haematopoiesis-support stromal cells, adipocytes and osteoblasts [5,6,7]. MSCs, similar to other stem cells, have an essential role in the regeneration/ maintenance of the adult tissues submitted to physiological modelling/turnover or following injury. At present, MSCs show great promise for use in a variety of cell-based therapies, include repair of defects in cardiovascular muscle, spinal cord, bone, and cartilage.

Recently, enhancement of bone repair in the necrotic zone by bone marrow MSCs has been highlighted for the treatment of osteonecrosis before collapse of the head [8,9]. MSCs can be delivered into the injured tissue either by invasive or by noninvasive means. Of primary importance to the success of such a strategy is the production of viable, reproducible protocols for stem cell population expansion. Invasive method is done on a surgically exposed necrotic head. Isolated primary mesenchymal stem cells are low in numbers, in vitro expansion is necessary. Although it is known that adult bone marrow MSCs can be rapidly expanded in vitro, migrate, and differentiate into multiple tissues in vivo. However, the expansion potential is limited and in vitro aging leads to loss of multipotency and replicative senescence. In addition, many transplanted cells die shortly after implantation as a result of physical stress from the implantation procedure itself, inflammation, or hypoxia. Under consideration of noninvasive methods of targeting

the injured tissue with stem cells that take advantage of endogenous mechanisms. Recent studies in a rat model showed that endogenous signaling via cytokines can enhance mobilization, homing, and transdifferentiation of stem cells [10]. MSCs can be mobilized from the bone marrow (central pool of stem cells) and directed to the injured tissue or organ. Currently, little is known about the signals involved in the mobilization and homing of stem cells to the injured tissue. It is believed that the cytokines SCF, G-CSF, and stromal-cell-derived factor-1 (SDF-1) and their receptors play a major role (1).

MSCs constitutively expressed mRNA for interleukin (IL), colony-stimulating factor (CSF), and stem cell factor (SCF) [11]. G-CSF is a polypeptide hematopoietic factor that stimulates survival, proliferation, and maturation of neutrophilic granulocyte progenitors and enhances their functions. Stem cell factor (SCF) is a potent costimulatory molecule for many cytokines. Its synergy with granulocyte colony-stimulating factor (G-CSF) results in important biologic and clinical effects, although the mechanism by which this occurs remains poorly understood [12]. Notwithstanding, cytokine-induced mobilization of bone marrow stem / progenitor cells in the necrotic foci may represent a promising strategy for replacing necrotic bone. A better understanding of the kinetics of MSC and MSC derived progenitor cell proliferation and differentiation is of great current interest from both a clinical and tissue engineering perspective [13,14,15]. Consequently, in the present study, we investigated the biological effects of G-CSF and SCF, alone and in combination, on proliferation and osteogenic differentiation capacity of bone marrow MSCs.

2. MATERIALS AND METHODS

2.1. Generation of Rabbit BM-MSCs

The BM-MSCs were prepared as described previously with slight modification [16]. Bone marrow cells were harvested from iliac crest aspirates from healthy 3-month old New Zealand white rabbits, and the procedures were used in accordance with the procedures approved by the animal experimentation and ethics committees of Tongji Medical College. Approximately 10 ml of iliac bone marrow was aspirated and suspended in 20 ml of DMEM-LG medium (Gibco) containing 2000 U of heparin sodium. Mononuclear cells (MNCs) were separated on Ficoll-Paque density gradient (1.077g/mL) and washed in PBS. Then MNCs were seeded at a density of 1×10^6 cells/cm^2 in growth medium containing DMEM- LG and 10% FBS (HyClone) and incubated at 37°C in 5% CO_2/95% air. Medium was changed first after 24 h and then every 3 days. MSCs were used at passage 3 to 4.

2.2. Flow Cytometric Analyses

To evaluate the lineage and surface marker phenotype of passage 3 cultures of MSCs, cells were detached and incubated in phosphate-buffered saline containing 1% bovine serum albumin with the following fluorescent antibodies: anti-human CD29 (integrin b1 chain)–PE, anti-huaman CD90 (Thy-1)-FITC, anti-human CD105 (endoglin)-PE, anti-human CD34-FITC, anti-human CD45-FITC, anti-human HLA-DR-PE(Santa Cruze, USA), and were analyzed by FACS caliber flow cytometry (BD, USA). To examine the expression of G-CSFR(G-CSF receptor) and c-kit (SCF receptor) on the cultured MSCs, PE- conjugated mouse anti-human G-CSFR (CD114) monoclonal antibody (Becton- Dickinson, America), mouse anti-human c-kit(CD117) monoclonal antibody and secondary antibodies conjugated with FITC (Zymed，America）were used. Isotype-identical antibodies served as controls. Meanwhile, immunofluorescence staining was used to test cultured MSCs as well. Primary antibody was anti-vimentin, and secondary antibody was anti-gout polyvalent-Cy3 conjugate (Sigma).

2.3. Cell Proliferation of MSCs

MSCs of passage 3 were harvested by treatment of the cells with Trysin/EDTA and washed twice with DMEM. The cells were then resuspended (1×10^4 cells per ml) in DMEM containing 10% FBS and plated in 96-well culture plates (100ul /well). After 48 h culture, culture medium and nonadherent cells were removed. Every experimental group was given 100ul growth medium containing DMEM-LG, 2% FBS, and various concentration of SCF and G-CSF, and cultured in the CO_2 incubator. Assessment of cell proliferation was measured in terms of optical absorbance (OD) per well by a semi-automated tetrazolium- based colorimetric assay using MTT. The growth rate was calculated according to the formula: (OD $_{treated}$/OD $_{control}$ -1)×100%. And the cell growth curves were drawn with the culture time (d) as the abscissa and the mean OD value as the ordinate.

2.4. Colony-Forming Unit-Fibroblast (CFU-F) Assay

The frequency of CFU-F was measured using the method of Castro-Malaspina with slight modification [17]. BMSCs (at 5×10^5 cells/ml) were suspended in growth medium containing DMEM-LG, 10% FBS, antibiotics, and various concentration of SCF and G-CSF (0.1,1,10,100, and 1000 ng/mL), and cultured in the CO_2 incubator. Each flask contained 1×10^6 cells. The medium was completely renewed every 3 days. The fibroblast colonies were counted on day 12 of culture. Cell clusters containing > 50 cells were scored as CFU-F colonies. Based on the number of colonies generated in the various concentrations of CSF, a dose-response curve to each growth factor was graphed.

2.5. Alkaline Phosphatase (ALP) Detection of MSCs

MSC (3×10^6 cells per well) were plated in 48-well culture plates, then being induced by an osteogenic supplement (1×10^{-7}mol/L dexamethasone, 5.0 mmol/L b- glycerophosphate, 50 mg/L ascorbic acid) and treated with G-CSF and/or SCF at final concentrations of 0.1, 1, 10, 100, and 1000 ng/ml for 5d at 37°C in an atmosphere containing 5% CO_2. Culture was washed with phosphate-buffered saline (PBS), fixed in a solution of cold 70% ethanol for 15 min and stained for alkaline phosphatase (ALP) activity. For quantitative analysis, the plates were washed thrice with ice-cold PBS and lysed by two cycles of freezing and thaw. Aliquots of supernatants were subjected to alkaline phosphatase activity using an alkaline phosphatase kit (Nanjing Jiancheng Bioengineering Institute, China). The osteogenic differentiation rate was calculated according to the formula: (ALP activity$_{treated}$/ALP activity$_{control}$ -1)$\times100\%$.

2.6. Statistical Analysis

Data were expressed as mean ± SEM of at least three separate experiments. Comparisons were made using 2-tailed unpaired Student t test and Mann-Whitney signed rank test as appropriate. A P value of <0.05 was considered significant.

3. RESULTS

3.1. Identification of MSCs

The expression of stem cell markers assessed with flow cytometric analyses showed that after passage 3 these cells were nearly completely negative for haematopoietic cell markers (CD34, CD45, and HLADR) and positive for CD29, CD90 and CD105, which were markers of MSCs. MSCs presented as a homogeneous fibroblast-like cell population. They were positive in immuno-cytochemical staining with anti-vimentin antibody. This population was considered to be MSC based on its immunophenotype profile (**Figure 1**).
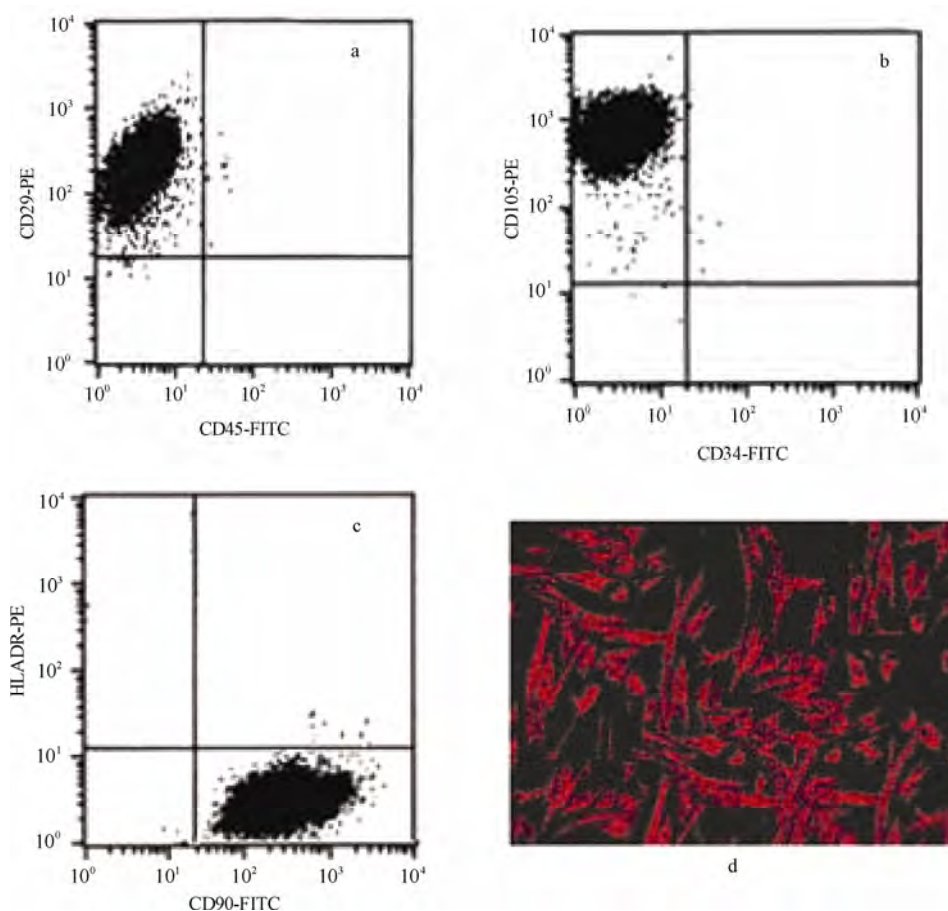
Figure 1. Immunophenotype of cultured MSCs. A. Immunophenotype of bone marrow MSCs by FACS analysis. The immunophenotype was CD29$^+$/CD45$^-$ (a),CD105$^+$/CD34$^-$ (b), CD90$^+$/HLADR$^-$(c). B. Immunofluorescence staining of vimentin were observed in all cells (d).

### 3.2. The Expression of G-CSFR and C-Kit on Surface of MSCs

We analysed the expression of receptors for G-CSF (G-CSFR) and SCF (c-kit) on rabbit bone marrow MSCs. Flow cytometric analysis showed that G- CSFR was expressed at extremely level in MSCs ($1.2 \pm 0.5\%$). Although the expression of G-CSFR was higher after G-CSF administration ($4.2 \pm 1.6\%$), the difference was not statistically significant ($P > 0.05$). MSCs were shown to constitutively express low levels of c-kit at the cell surface, as shown by flow cytometric analysis. SCF treatment induced a significant increase in the number of c-kit+ cells. The number of c-kit+cells was significantly larger in the SCF-treated group ($28.4 \pm 4.8\%$) than in the control group ($13.6 \pm 3.6\%$) ($P < 0.05$ vs. control group) (**Figure 2**).

3.3. Effects of G-CSF/SCF on the Proliferation of MSCs

As well, we also found that G-CSF and SCF could promote MSCs proliferation significantly (*$P < 0.05$, **$P < 0.01$). Treating MSCs with G-CSF and SCF ($0.1 \sim 100$ ng/ml) resulted in a positive dose-dependent increase in cell proliferation, and the maximal growth rate was 42.2% and 34.2%, respectively. When the dose reached 1000ng/ml, the growth rate stepped down, instead. As time proceeded, cells in the group treated with combination of G-CSF and SCF growed more faster than the groups treated with G-CSF,SCF , or none of them, and the same cell population was advanced over 2 to 3 days. Moreover, a shift to the left in the growth curve and a advance in multiplication point was observed. A comparison for the promotion of cell proliferation, the combination of G-CSF and SCF was superior to the better of the two agents given alone (**Figure 3**).

3.4. CFU-F-Colony Formation of MSCs Response to Different Doses of G-SCF and SCF

MSCs have been recognized to derive from single-cell suspensions of bone marrow by the selective growth of plastic-adherent fibroblast-like cell colonies. Such a colony of adherent marrow stromal cells, each derived from a single precursor cell, is termed a CFU-fibroblast (CFU-F) [7]. The number of CFU-Fs formed per 1×10^6 MSCs plated varied among groups. Treating MSCs with G-CSF and SCF ($0.1 \sim 100$ ng/ml) resulted in a positive dose-dependent increase in the formation of CFU-F. G-CSF and SCF significantly increased the number of CFU-F compared with control. The effect of G-CSF was powerful than SCF, and the maximal CFU-F formation occurred with exposure to the combination of G-CSF (100 ng/mL) and SCF (100 ng/mL). (*$P < 0.05$, **$P < 0.01$) (**Figure 4**).
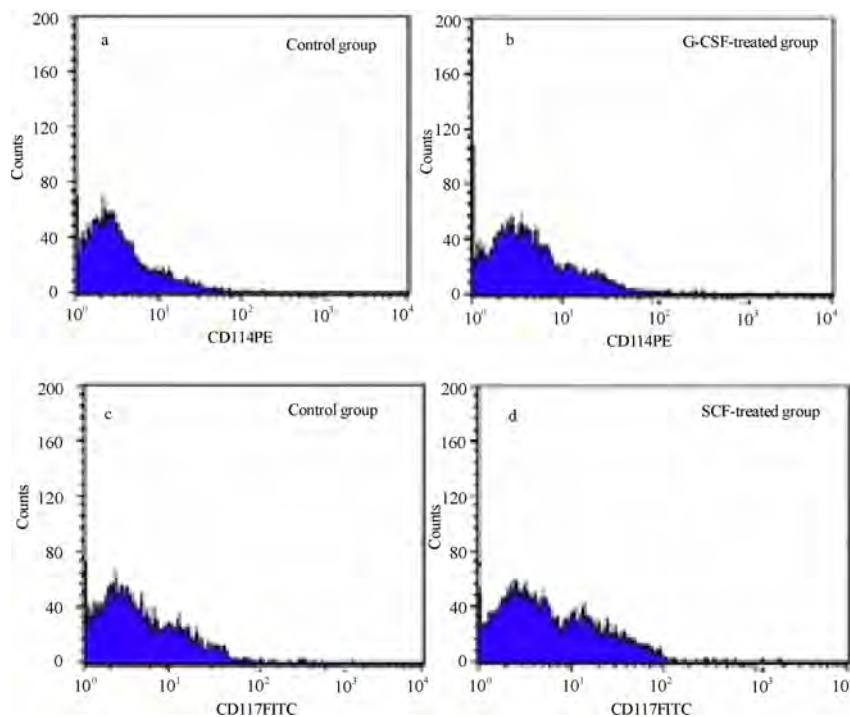
Figure 2. Immunophenotyping of cultured MSCs by flow cytometric analysis. The histograms show specific mAbs(CD114/CD117) in control group and treated group.(a) Control group; (b) G-CSF treated group;(c)Control group; (D) SCF treated group.
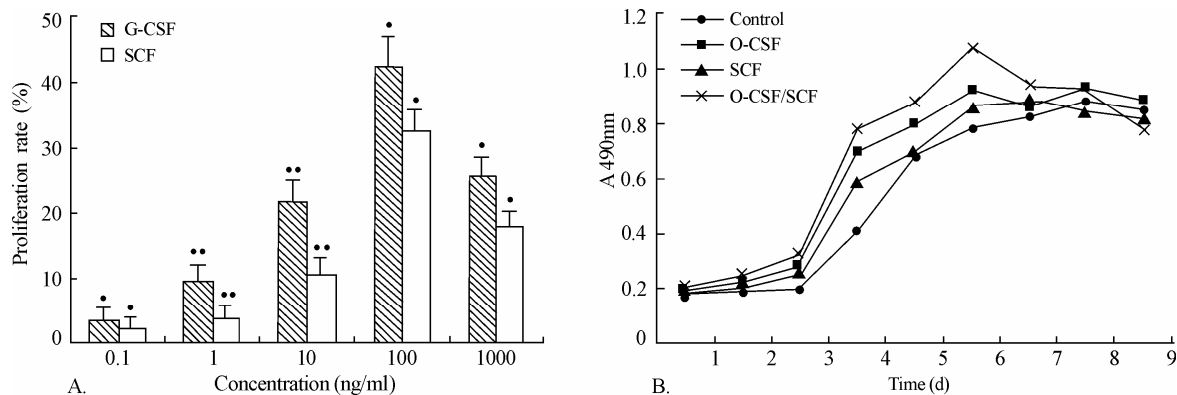
Figure 3. Effects of G-CSF/SCF on the proliferation of MSCs . A. The effect of G-CSF and SCF on the proliferation rate of MSCs. G-CSF and SCF at final concentrations of 0.1, 1, 10, 100, and 1000 ng/ml . B. To examine the effects of G-CSF, SCF, alone or in combination on MSCs growth curve. G-CSF,100 ng/ml; SCF, 100 ng/ml .Values represent means ±SEM .The asterisk indicates statistical difference (*P < 0.05, **P < 0.01).
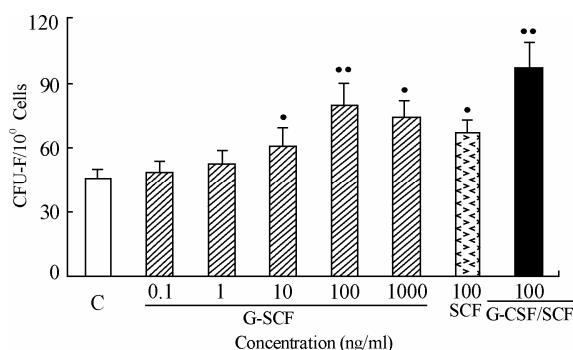
Figure 4. Colony-forming unit-fibroblast (CFU-F) assay. CFU-F- colony formation by MSCs on response to different doses of colony-stimulating factors (G-CSF and SCF, alone or in combination). The optimal dose of SCF and G-CSF was 100 ng/ml. The combination of G-CSF and SCF had the best activity. C= control group. The results are presented as the number of CFU-F (mean±SEM). The asterisk indicates statistical difference (*P < 0.05, **P < 0.01).

3.5. Effects of G-CSF and SCF on the Osteogenic Differentiation of MSC

In repeated ex vivo experiments, we observed that G-CSF and SCF had obvious inhibitory action on the osteogenic differentiation of MSC. High Alkaline phosphatase (ALP) activity was an osteoblastic phenotype. When cultured in osteogenic conditions, MSCs acquired an osteoblastic morphology demonstrated by an upregulation of ALP activity (**Figure 5(a), 5(b)**). ALP activity in every group was measured quantitativly at different time point. ALP activity of cells cultured with G- CSF and SCF was low at one day, and increased time-dependently. Inhibitory effect of G-CSF on ALP activity superior to SCF, and the combination of G-CSF and SCF had the most powerful effect, as compared to control (P<0.05) (**Figure 5(c)**). The concentration-effect relationship of G-CSF and SCF was described. It wasn't shown here that dose-response measurements generated

a linear plot of inhibitor concentration. The calibration curve was validated and linear over the concentration range from 0.1 to 100 ng/ml, and the maximal inhibition rate was obtained at a dosage of 100 ng/ml (54.12％ and 34.38％, respectively)and did not increase more at the dosage of 1000 ng/ml (*P<0.05,**P<0.01) (**Figure 5(d)**).

4. DISCUSSION

In addition to hematopoietic stem cells, it is now clear that adult bone marrow contains a rare population of mesenchymal stem/progenitor cells (MSCs) (0.01% to 0.001%) (18). MSCs are of great therapeutic potential because of their ability to self-renew and differentiate into multiple tissues. They can be extensively expanded in vitro and, when cultured under specific permissive conditions, retain their ability to differentiate into multiple lineages including bone, cartilage, tendon, muscle, nerve, and stromal cells [18,19]. There is increasing evidence of the potential use of MSC infusion for clinical purposes, such as hematopoietic support, tissue repair, immunosuppressive cell therapy, and anticancer gene therapy [20,21,22,23,24]. Thus, it is of great interest to study which factors may have a role in MSC adhesion, migration, expansion, maintenance of MSC stem cell plasticity, and interaction with normal and pathologic cells once the MSCs are recruited and included in proliferating tissues.

The cytokine G-CSF is widely used to mobilize stem/ progenitor cells. How G-CSF mobilizes stem cells and progenitor cells from the bone marrow into the circulation is not clear. In addition, G-CSF plays an essential role in proliferation, survival, and differentiation of granulocyte precursors in the marrow. Generally, G-CSF acts by binding to its receptor (G-CSFR), a single-chain member of the cytokine receptor superfamily, which lacks tyrosine kinase activity. Binding of G-CSF to its receptor induces the tyrosine phosphorylation of a
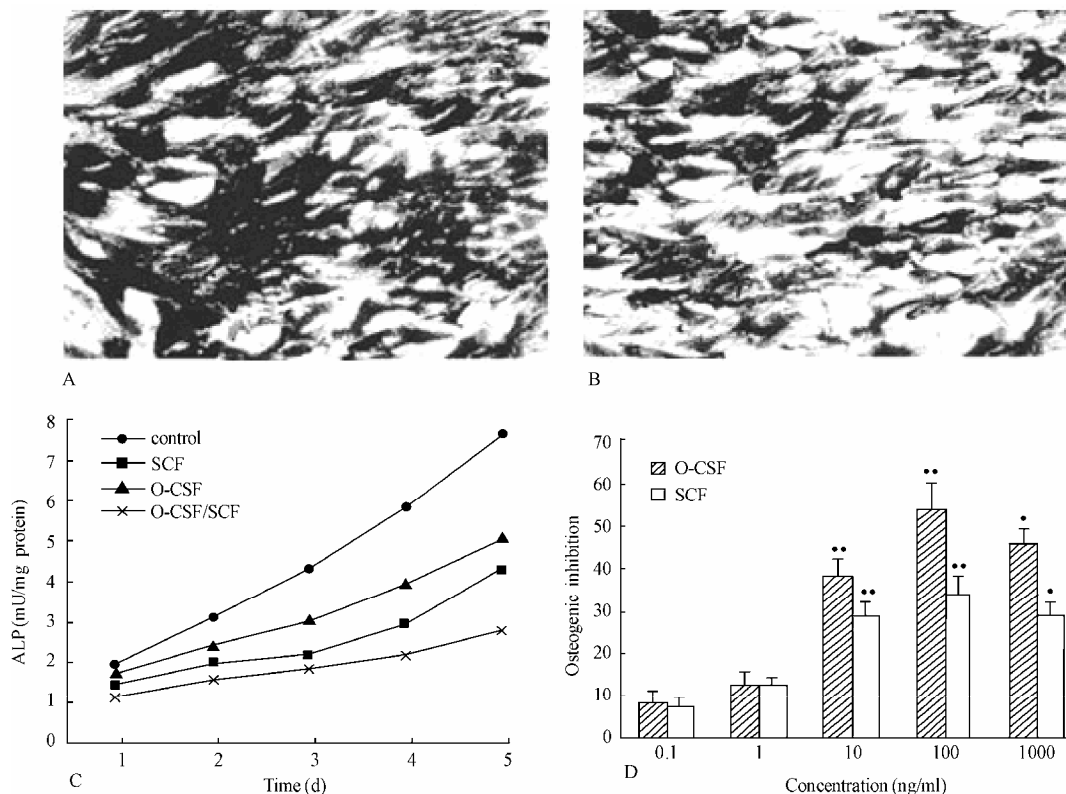
Figure 5. Effects of G-CSF and SCF on the osteogenic differentiation of MSC. (A,B) Alkaline phosphatase(ALP) staining was carried out using an Ca–Co staining method. Representative images of ALP staining were shown. A, control group; B, G-CSF/SCF treated group. C. The effects of G-CSF/SCF on the ALP activity in BMSCs (mU/mg protein). G-CSF,100 ng/ml; SCF, 100 ng/ml.   D. Osteogenic inhibition rate of G-CSF/SCF on MSCs. G-CSF and SCF at final concentrations of 0.1, 1, 10, 100, and 1000 ng/ml . Values represent means ±SEM .The asterisk indicates statistical difference (*P < 0.05, **P < 0.01).

number of cellular proteins and activates signal transduction pathways, including Ras/Raf/MAPK, PI3- kinase, and JAK/STAT cascades [25,26,27]. But confusing results trickled in, flow cytometric analysis showed that bone marrow MSCs expressed very low levels of G-CSFR, even treated with G-CSF. This suggested that an indirect mechanism might exist. For example, G-CSF stimulation potentiates the homing abilities of cytokine-stimulated BMSCs, an action that can be inhibited by pretreatment with anti-CXCR4 antibodies [28]. In contrast to the G-CSF receptor, the receptor for SCF, possesses intrinsic tyrosine kinase activity. Binding of SCF to c-kit induces kinase activation and transphosphorylation of the receptor chains. Recent exciting evidence has shown the central role of SCF, c-kit, and matrix metalloproteinase- 9 in the mobilization of stem and progenitor cells from the bone marrow [29]. As shown by flow cytometric analysis, MSCs were shown to constitutively express c-kit at the cell surface and which could be increased materially by SCF intervention. The increasing evidence showed that the combination of G-CSF and SCF could generate synergistic effect.

Bodine, *et al*. [30] found that mice bone marrow cells collected 14 days after in vivo administration of G-CSF and SCF have a 10 times greater ability to repopulate than untreated bone marrow. Cell cycle analysis revealed that the enhanced proliferative state induced by SCF and G-CSF cotreatment was associated with a direct effect of these cytokines on cell cycle distribution, specifically a marked shortening of the duration of G_0/G_1 [11]. Despite increased understanding of G-CSF and SCF signaling pathways, the mechanism by which this biologically and clinically important interaction between SCF and G-CSF occurs remains poorly understood.

In vitro isolation and characterization of MSCs is based on their adherence, rapid expansion in serum-containing medium, expression of specific cell surface antigens as well as their ability to differentiate into various mesodermal tissues such as fat, bone, cartilage and muscle [31,32,33,34]. Morphologically, MSCs in their undifferentiated state are spindle shaped and resemble fibroblasts. They do not express hematopoietic markers, but a specific pattern of molecules. At flow cytometry, the isolated cells showed a homogeneous expression of

markers commonly used to identify hMSCs, i.e., CD29, CD90, CD105 positivities, and CD34, CD45, HLADR negativities, consistent with that reported for bone marrow-derived MSCs [20,34]. Although these markers have been used by various groups, there is still no general consensus on the optimal marker combination for MSCs. At present we did not know how long MSCs will maintain innate characteristics, so we used early MSCs not exceeding 4 passages based on the assumption that early passage cells would be more likely to have the innate characteristics of MSCs.

Cell proliferation was determined using MTT assay, which showed the combination of G-CSF and SCF was superior to the better of the two agents given alone. Usually, MSCs were typically defined by their capacity to adhere on plastic and form a fibroblastic colony (CFU-F). The colony forming unit fibroblast (CFU-F) assay was a well-established method for the quantification of marrow stromal cells (MSCs). We observed that G-CSF/SCF enhanced ex vivo MSC proliferation, and treating MSCs with G-CSF and SCF (0.1~100 ng/ml) resulted in a positive dose-dependent increase in the formation of CFU-F. G-CSF/SCF proliferative effect on MSCs was direct, dose dependent, long lasting. In addition, ALP activity of cells cultured with G-CSF and SCF was low at one day, and increased time-dependently. MSC differentiation potential was not affected obviously by the enhancement of self-renewal, as the proliferative effect was not associated with induced differentiation.

On the whole, these studies demonstrated that MSCs responded to G-CSF, SCF, and to G-CSF plus SCF in a manner that suppressed differentiation, and promoted proliferation and self-renewal, and supported the view that these factors could act synergistically. And the effects of G-CSF/SCF on MSCs give the cue to understand better the biology and the role of MSCs. However, the biochemical mechanism underlying this activity remains to be resolved.

5. ACKNOWLEDGEMENTS

REFERENCES

[1] P. Menasche Cell transplantation in myocardium. Ann Thorac Surg 2003, 75: S20−28.

[2] E. M. Horwitz, (2003) Bone marrow transplantation: It's not just about blood anymore! Pediatr Transplant, **7**, 56−58.

[3] N. Koike, D. Fukumura, O. Gralla, *et al*., (2004) Tissue engineering: Creation of long-lasting blood vessels, Nature, **428**, 138−139.

[4] K. D. Lee, T. K. Kuo, J. Whang-Peng, *et al*., (2004) In vitro hepatic differentiation of human mesenchymal stem cells, Hepatology, **40**, 1275−1284.

[5] D. Baksh, L. Song, and R. S. Tuan, (2004) Adult mesenchymal stem cells: characterization, differentiation, and application in cell and gene therapy, J Cell Mol Med, **8**, 301−316.

[6] A. Peister, J. A. Mellad, B. L. Larson, B. M. Hall, L. F. Gibson, and D. J. Prockop, (2004) Adult stem cells from bone marrow (MSCs) isolated from different strains of inbred mice vary in surface epitopes, rates of proliferation, and differentiation potential, Blood, **103**, 1662−1668.

[7] B. Short, N. Brouard, T. Occhiodoro-Scott, A. Ramakrishnan, and P. J. Simmons, (2003) Mesenchymal stem cells, Arch. Med. Res, **34**, 565−571.

[8] V. Gangji, J. P. Hauzeur, C. Matos, V. De Maertelaer, M. Toungouz, and M. Lambermont, (2004) Treatment of osteonecrosis of the femoral head with implantation of autologous bone-marrow cells: A pilot study, J Bone Joint Surg (Am), **86**, 1153−1160.

[9] V. Gangji, J. P. Hauzeur, A. Schoutens, M. Hinsenkamp, T. Appelboom, and D. Egrise, (2003) Abnormalities in the replicative capacity of Osteoblastic cells in the proximal femur of patients with osteonecrosis of the femoral head, J Rheumatol, **30**, 348−351.

[10] D. Orlic, J. M. Hill, and A. E. Arai, (2002) Stem cells for myocardial regeneration, Circ Res, **91**, 1092−1102.

[11] M. K. Majumdar, M. A. Thiede, S. E. Haynesworth, S. P. Bruder, and S. L. Gerson, (2000) Human marrow-derived mesenchymal stem cells (MSCs) express hematopoietic cytokines and support long-term hematopoiesis when differentiated toward stromal and osteogenic lineages, J Hematother Stem Cell Res, **9**, 841−848.

[12] R. F. Duarte and D. A. Frank, (2000) SCF and G-CSF lead to the synergistic induction of proliferation and gene expression through complementary signaling pathways, Blood, **96**, 3422−3430.

[13] R. Cancedda, G. Bianchi, A. Derubeis, and R. Quarto, (2003) Cell therapy for bone disease: A review of current status, Stem Cells, **21**, 610−619.

[14] F. R. Rose and R. O. Oreffo, (2002) Bone tissue engineering: Hope vs hype, Biochem. Biophys. Res Commun., **292**, 1−7.

[15] X. B. Yang, H. I. Roach, N. M. Clarke, *et al*., (2001) Human osteoprogenitor growth and differentiation on synthetic biodegradable structures after surface modification, Bone, **29**, 523−531.

[16] D. C. Colter, I. Sekiya, D. J. Prockop, (2001) Identification of a subpopulation of rapidly self-renewing and multipotential adult stem cells in colonies of human marrow stromal cells, Proc Natl Acad Sci U S A, **98**, 7841−7845.

[17] S. A. Wexler, C. Donaldson, P. Denning-Kendall, C. Rice, B. Bradley, and J. M. Hows, (2003) Adult bone marrow is a rich source of human mesenchymal 'stem' cells but umbilical cord and mobilized adult blood are not, British Journal of Haematology, **121**, 368−374.

[18] M. F. Pittenger, A. M. Mackay, S. C. Beck, *et al*., (1999) Multilineage potential of adult human mesenchymal stem cells, Science, **284**, 143−147.

[19] A. P. Croff and S. A. Przyborski, (2004) Generation of neuroprogenitor-like cells from adult mammalian bone marrow stromal cells in vitro, Stem Cells Dev, **13**, 409−420.

[20] Y. Jiang, B. N. Jahagirdar, R. L. Reinhardt, *et al.*, (2002) Pluripotency of mesenchymal stem cells derived from adult marrow. Nature, **418**, 41−49.

[21] M. Studeny, F. C. Marini, R. E. Champlin, *et al.*, (2002) Bone marrow-derived mesenchymal stem cells as vehicles for interferon-*β* delivery into tumours, Cancer Res, **62**, 3603−3608.

[22] O. N. Koc, S. L. Gerson, B. W. Cooper, *et al.*, (2000) Rapid hematopoietic recovery after coinfusion of autologous-blood stem cells and culture-expanded marrow mesenchymal stem cells in advanced breast cancer patients receiving high-dose chemotherapy, J Clin Oncol, **18**, 307−316.

[23] D. Orlic, J. Kajstura, S. Chimenti, *et al.*, (2001) Bone marrow cells regenerate infarcted myocardium, Nature, **410**, 701−705.

[24] M. Krampera, S. Glennie, R. Laylor, *et al.*, (2003) Bone marrow mesenchymal stem cells inhibit the response of naïve and memory antigen-specific T cells to their cognate peptide, Blood, **101**, 3722−3729.

[25] B. Avalos, (1996) Molecular analysis of the granulocyte-colony stimulating factor receptor, Blood, **88**, 761−777.

[26] M. L. McLemore, S. Grewal, F. Liu, *et al.*, (2001) STAT-3 activation is required for normal G-CSF-dependent proliferation and granulocytic differentiation, Immunity, **14**, 193−204.

[27] J. R. Fu, W. L. Liu, J. F. Zhou, *et al.*, (2006) Sonic hedgehog protein promotes bone marrow-derived endothelial progenitor cell proliferation, migration and VEGF production via PI 3- kinase/Akt signaling pathways, Acta Pharmacol Sin, **27**, 685−693.

[28] O. Kollet, A. Spiegel, A. Peled, *et al.*, (2001) Rapid and efficient homing of human CD34 (+) CD38 (-/low) CXCR4 (+) stem and progenitor cells to the bone marrow and spleen of NOD/SCID and NOD/SCID/B2m(null) mice, Blood, **97**, 3283−3291.

[29] B. Heissig, K. Hattori, and S. Dias, (2002) Recruitment of stem and progenitor cells from the bone marrow niche requires MMP-9 mediated release of kit-ligand, Cell, **109**, 625−637.

[30] D. M. Bodine, N. E. Seidel, and D. Orlic, (1996) Bone marrow collected 14 days after in vivo administration of granulocyte colony- stimulating factor and stem cell factor to mice has 10-fold more repopulating ability than untreated bone marrow, Blood, **88**, 89−97.

[31] E. H. Javazon, K. J. Beggs, and A. W. Flake, (2004) Mesenchymal stem cells: Paradoxes of passaging, Exp Hematol, **32**, 414−425.

[32] P. A. Zuk, M. Zhu, H. Mizuno, *et al.*, (2001) Multilineage cells from human adipose tissue: implications for cell-based therapies, Tissue Eng, **7**, 211−228.

[33] M. F. Pittenger and B. J. Martin, (2004) Mesenchymal stem cells and their potential as cardiac therapeutics, Circ Res, **95**, 9−20.

[34] J. R. Smith, R. Pochampally, A. Perry, *et al.*, (2004) Isolation of a highly clonogenic and multipotential subfraction of adult stem cells from bone marrow stroma, Stem Cells, **22**, 823−831.

Call for Papers ◆IEEE EMB ⊜ iCBBE

The 4th International Conference on Bioinformatics and Biomedical Engineering
(iCBBE 2010)

June 18-20, 2010   Chengdu, China

The 4th International Conference on Bioinformatics and Biomedical Engineering (iCBBE 2010) will be held from June 18th to 20th, 2010 in Chengdu, China. You are welcome to share your recent advances and achievements in all aspects of bioinformatics and biomedical engineering on the conference. **And all accepted papers in iCBBE 2010 will be published by IEEE and indexed by Ei Compendex and ISTP.**

Topics
Bioinformatics and Computational Biology
- Protein structure, function and sequence analysis
- Protein interactions, docking and function
- Computational proteomics
- DNA and RNA structure, function and sequence analysis
- Gene regulation, expression, identification and network

- Structural, functional and comparative genomics
- Computer aided drug design
- Data acquisition, analysis and visualization
- Algorithms, software, and tools in Bioinformatics
- Any novel approaches to bioinformatics problems

Biomedical Engineering
- Biomedical imaging, image processing & visualization
- Bioelectrical and neural engineering
- Biomechanics and bio-transport
- Methods and biology effects of NMR/CT/ECG technology
- Biomedical devices, sensors and artificial organs
- Biochemical, cellular, molecular and tissue engineering
- Biomedical robotics and mechanics

- Rehabilitation engineering and clinical engineering
- Health monitoring systems and wearable system
- Bio-signal processing and analysis
- Biometric and bio-measurement
- Biomaterial and biomedical optics
- Other topics related to biomedical engineering

Special Sessions
Biomedical imaging
Biostatistics and biometry
The information technology in bioinformatics
Environmental pollution & public health

Sponsors
IEEE Eng. in Medicine and Biology Society, USA
Gordon Life Science Institute, USA
University of Lowa, USA
Wuhan University, China
Sichuan University, China
Journal of Biomedical Science and Engineering, USA

Important Dates
Paper Due: Oct.30, 2009
Acceptance Notification: Dec.31, 2009
Conference: June 18-20, 2010

Contact Information
Website:http://www.icbbe.org/2010/
E-mail: submit@icbbe.org

Journal of Biomedical Science and Engineering (JBiSE)

www. scirp. org/journal/jbise

JBiSE, an international journal, publishes research and review articles in all important aspects of biology, medicine, engineering, and their intersection. Both experimental and theoretical papers are acceptable provided they report important findings, novel insights, or useful techniques in these areas. All manuscripts must be prepared in English, and are subject to a rigorous and fair peer-review process. Accepted papers will immediately appear online followed by printed in hard copy.

Subject Coverage

Bioelectrical and neural engineering

Bioinformatics

Medical applications of computer modeling

Biomedical modeling

Biomedical image processing & visualization

Real-time health monitoring systems

Biomechanics and bio-transport

Patten recognition and medical diagnosis

Biomedical effects of electromagnetic radiation

Safety of wireless communication devices

Biomedical devices, sensors, and nano technologies

NMR/CT/ECG technologies and EM field simulation

Physiological signal processing

Medical data mining

Other related topics

JBiSE
ISSN: 1937-6871
Volume 2 Number 3 June 2009

Journal of Biomedical Science and Engineering

www. scirp. org/journal/jbise

Editor-in-Chief
Kuo-Chen Chou

Editor−in−Chief

Kuo-Chen Chou
Gordon Life Science Institute, San Diego, California, USA

Notes for Intending Authors

Submitted papers should not have been previously published nor be currently under consideration for publication elsewhere. Paper submission will be handled electronically through the website. All papers are refereed through a peer review process. For more details about the submissions, please access the website.

Website and E-Mail

www. scirp. org/journal/jbise
Email: jbise@scirp.org

Editorial Board

ISSN 1937-6871 (Print), 1937-688X (Online)

TABLE OF CONTENTS

Volume 2, Number 3, June 2009

9771937687000106